STUDIES OF EPITAXIAL SILICON AND GRAPHENE GROWTH ON SILICON CARBIDE UNDER SILANE GAS

A Thesis
Presented to
The Academic Faculty

by

Tien Manh Hoang

In Partial Fulfillment
of the Requirements for the Degree
Doctor of Philosophy in the
School of Physics

Georgia Institute of Technology
May 2017

STUDIES OF EPITAXIAL SILICON AND GRAPHENE GROWTH ON SILICON CARBIDE UNDER SILANE GAS

Approved by:

Professor Phillip N. First, Advisor
School of Physics
Georgia Institute of Technology

Professor Kurt Wiesenfeld
School of Physics
Georgia Institute of Technology

Professor Zhigang Jiang
School of Physics
Georgia Institute of Technology

Professor Thomas Orlando
School of Chemistry & Biochemistry
Georgia Institute of Technology

Professor Edward H. Conrad
School of Physics
Georgia Institute of Technology

Date Approved: February 9, 2017

To my family and my lover,

Le Tu Nhat Lan Anna

ACKNOWLEDGEMENTS

First of all, I would like to dedicate my special appreciation to my thesis advisor Dr. Phillip N. First. When I first met him in summer 2010, to my surprise the professor asked me about my ability to fix a bicycle or a car. After joining his group, I understood that through this question he wanted to test my dexterity, which is necessary for a Ph.D. student working on the ultra-high vacuum systems. I truly appreciate Dr. First guidance in expanding my experimental skills and academic knowledge. His inspiration, patience, and understanding helped me create my career path. I would also like to acknowledge my gratitude to other committee members, Dr. Jiang, Dr. Orlando, Dr. Conrad, and Dr. Wiesenfeld for reading and giving useful advice on the thesis.

The thesis would not be complete without cooperation with my former and present lab partners: Dr. Britt Torrance, Dr. Yuntao Li, Dr. David Lee Miller, Dr. Kevin D. Kubista, Louis Wu, Di Chen, and Zachery Enderson. I am glad that we could discuss physics, exchange knowledge, and help each other during every experiment. I would also like to thank Dr. Sonam Sherpa, Dr. James M. Palmer, Dr. Feng Wang, Dr. Meredith Nevius, Owen Vail, and Jean-Philippe Turmaud for collaborating and sharing ideas, which contributed to this thesis. Furthermore, I would like to thank to all my friends who supported me through this journey. When I first came to the US, I was alone but thanks to your hospitality and help, you made this country become my second home.

Lastly, I would like to express my heartfelt gratitude to my family and to my love. Without your care and love, I would not be where I am today. My parents always give me the confidence when I doubt myself. They teach me how to be a

diligent, passionate as well as a caring and respectful person. They always believe in me and encourage me to achieve what I have thought to be impossible. My younger brother is my greatest competitor, but he is also my greatest role model. His work and achievements will always impress and motivate me. My special dedicate to my lover, Le Tu Nhat Lan, who is always on my side. Your love and support are vital to me not only for this thesis but also for the rest of my life.

This work was supported in part by the National Science Foundation (NSF) through grants DMR-1106131 and DMR-0820382 [MRSEC].

TABLE OF CONTENTS

DEDICATION . . . . . **iii**

ACKNOWLEDGEMENTS . . . . . **iv**

LIST OF TABLES . . . . . **ix**

LIST OF FIGURES . . . . . **x**

SUMMARY . . . . . **xviii**

I INTRODUCTION **1**

1.1 Motivation 1

1.2 Physical Properties of Graphene 4

1.3 Hexagonal Silicon Carbide 10

1.4 Epitaxial growth 11

1.5 Epitaxial Graphene (EG) Growth on Silicon Carbide 14

1.5.1 Silicon faces: zero-layer graphene 16

1.5.2 Carbon faces: multiple layer graphene 17

1.5.3 Sidewall graphene nanoribbons (GNRs) 17

1.6 Thesis Outline 20

II EXPERIMENTAL METHODS **21**

2.1 Sample Preparation 22

2.1.1 Dimple Grinding 23

2.1.2 Hydrogen Etching 26

2.2 Growth System 28

2.2.1 Design and Operation 28

2.2.2 Temperature Measurement 33

2.3 Sample Characterization Tools 37

2.3.1 Low Energy Electrol Diffraction (LEED) 37

2.3.2 Auger Electron Spectroscopy (AES) 40

2.3.3 Scanning Tunneling Microscopy (STM) 43

2.3.4 Atomic Force Microscopy (AFM) 45
2.3.5 Scanning Electron Microscope (SEM) 46

III RECONSTRUCTIONS ON SILICON CARBIDE UNDER SILICON DEPOSITION 48

3.1 Auger Attenuation Model (AAM) 51
3.1.1 Basics 51
3.1.2 Continuum Limit for a Homogeneous Material 54
3.1.3 Layer Limit for a Homogeneous Material 55
3.1.4 Thin Films and Multilayer Materials 57
3.1.5 Connection to Tabulated Parameters 58
3.1.6 Thin film layers on SiC 60
3.1.7 Convert Auger data: from RFA to CMA 65
3.2 Experiments and Results 68
3.2.1 New reconstructions on $\boldsymbol{SiC(0001)}$ under silicon deposition 69
3.2.2 Reconstructions on $\boldsymbol{SiC(000\bar{1})}$ under silicon deposition . . . 76
3.3 Chapter Conclusion 82

IV EPITAXIAL GRAPHENE GROWTH ON VICINAL SILICON CARBIDE 84

4.1 Experimental Results 85
4.1.1 Dimple sample preparation 85
4.1.2 Dimple sample morphology after graphitization 86
4.2 $\boldsymbol{SiC}$ step bunching: a quasi one dimensional step model 94
4.2.1 Theory of Step Bunching 94
4.2.2 Simulation of Step Bunching 99
4.3 Discussions 105
4.4 Chapter Conclusion 109

V CONCLUSION 110

APPENDIX A — AUGER ATTENUATION MODEL 113

APPENDIX B — CONVERT RFA AUGER DATA TO CMA-SCALING AND RESOLUTION 115

APPENDIX C — QUASI-1D STEP BUNCHING MODEL 116

REFERENCES 120

VITA 135

LIST OF TABLES

1 Electron Effective-Attenuation-Length (EAL) in Angstrom ($\mathring{A}$). Obtained from NIST software [131]. 64

2 Backscattering-Correction-Factor Database for Auger Electron Spectroscopy. Obtained from NIST software [132]. 64

3 Calculation the average bunch size N_{av} (nm) versus local angle α (degree) from AFM images at different locations inside the dimple. See text for explanation of estimation methods. 91

LIST OF FIGURES

1.1 Number of publications on graphene from 2004 to Dec. 2016. The graph indicates the exponential increase of graphene publications over a decade. Source from ISI Web of Science (search by topic: TS = Graphene). 2

1.2 Graphene is a $2D$ building block for all of other graphitic allotropes: $0D$ buckyballs (wrapped), $1D$ nanotubes (rolled), and $3D$ graphite (stacked) [26]. 5

1.3 Graphene's crystal lattice and first Brillouin zone. On the left is the honeycomb lattice of graphene, with the two sublattices denoted by colored circles. The triangle Bravais lattice has two basis vector $\boldsymbol{a}_1$ and $\boldsymbol{a}_2$. On the right is the first Brillouin zone of graphene, with two inequivalent points K and K' (Dirac points) [32]. 7

1.4 Graphene band structure. The Dirac points are the places where the upper edge of valance band and lower edge of conduction band meet. Those are six points at the six corner of the first Brillouin zone in which only two of them, K and K', are inequivalent. Near the Dirac points, the band structure is linear at the Dirac points [33]. 8

1.5 Comparison of some important electrical properties of silicon carbide and silicon material. All of three common silicon carbide polytypes possess superior properties for high-temperature, high-power, and high-frequency applications [38]. 9

1.6 Crystal structure of $4H$- and $6H$-SiC displayed parallel to the $(11\bar{2}0)$ plane: The big filled circle denotes a Si atom and the small white circle denotes a C atom. On the left is the $4H$-SiC with the unit cell height of 1.0 nm and on the right is the $6H$-SiC with the unit cell height of 1.5 nm. The top is the silicon-terminated face and the bottom is the carbon-terminated face [39]. 10

1.7 The atomic diffusion process of epitaxial thin film growth. The adatom can move on the terrace or along the step until it meets either another adatom to form a island (nucleation) or an existing island to stick to it (growth) [44]. 13

1.8 Structure models of the interface layers of epitaxial graphene on the two polar faces of SiC. Solid circles represent carbon atoms, open circles are silicon atoms and lined circles are graphene carbon atoms [64]. . . 15

1.9 (a) The lattice structure of a graphene sheet with armchair and zigzag edges. Top and bottom edges are zigzag, left and right edges are armchair. (b),(c),(d) Energy bands for a graphene nanoribbon with a typical length, L, and edges. The band structure of zigzag nanoribbon is always metallic while that of armchair nanoribbon is either metallic or insulating [78]. 18

1.10 Model of armchair sidewall graphene nanoribbons (GNRs): (a) The schematics of the sidewall which is composed of an extended facet in between several bottom and a top minifacets. (b) Atomic structure model of the sidewall GNRs which have free standing nano ribbons on the facets [82]. 19

2.1 (a) A $6H$-SiC wafer, purchased from Cree Inc, was diced into $3.5 \times 4.5\,\mathrm{cm}^2$ samples along the $< 1\bar{1}00 >$ and $< 11\bar{2}0 >$ directions. (b) A typical AFM image of these samples. The chemical mechanical polishing (CMP) surface shows plenty of straight, deep scratches. 22

2.2 (a) Gatan 656 Dimple Grinder at Institute of Paper Science and Technology. (b) The dimple grinder operation: both the spherically-shaped grinding/polishing wheel and sample table rotate simultaneously in a perpendicular direction. If the wheel is aligned with the sample axis of rotation, the spherical dimple is formed on the substrate. However, in this figure an aspherical surface dimple is created because of the off-axis alignment. 23

2.3 Sketching of the dimple. A concave-shaped dimple has been grinded in the middle of a SiC sample with the depth of about $30\,\mu$m. 24

2.4 A SiC dimple surface after rapidly polished with $0.25\,\mu$n diamond compound for 30 mins. (a) Bright-field optical microscopy image. The field of view of the optical microscopy image is approximately 0.5 mm. The circles, sharing the same center, indicate a well-defined spherical dimple. (b) AFM image which shows the straight, deep scratches on the surface after polishing. 25

2.5 (a) the custom tantalum thin-wall hydrogen etching furnace in Keck's lab. AFM images of a typical $6H$-$SiC(0001)$ after hydrogen etching show regular steps of (b) single unit-cell or (c) half unit-cell depending upon the etching recipe and initial surface conditions [86]. 26

2.6 AFM images of the $6H$-SiC dimple at different locations inside it after hydrogen etching treatment. It clearly indicates that the dimple surface is atomically flat consisting of regular, straight steps. It also shows the step density depending on the local angles which increases from the left to the right of the bottom panel. 27

2.7 Sketch of the home-made growth system. The system includes (from left to right) the growth chamber, gas-line connections, and in-situ LEED/AES characterization equipment, and transfer arm. The inset is a zoom-in of the graphite sample holder which is inserted from the front of the graphtie furnace (see the text for more details). 29

2.8 Gasline system. Three lines connect to three different gas cylinders (on the back, not shown) and each line has two Swagelok valves. Two lines in front, one is connected to a turbo pump and one is hooked up to the growth chamber via a leak valve. 31

2.9 The Mikron MI-GA140 Infrared Pyrometer (IP). (a) Overview of the IP with the adjustable lens in the front and the analog output cable in the back. (b) The zoom in of the built-in display with indication of temperature and emissivity. 33

2.10 Temperature on the surface using various emissivity setting in the infrared pyrometer: $\epsilon = 99\%$ (blue square), $\epsilon = 85\%$ (green cross), $\epsilon = 75\%$ (yellow triangle). The red circles are the temperature inside the hole itself. The experiments were performed in argon (on the left) and vacuum (on the right) environments. 35

2.11 The "effective" emissivity depends on the target temperature. The "effective" emissivity is the value inserted in the IP so that measuring the temperature on the furnace surface should give the exact temperature inside the furnace. 36

2.12 The Ewald sphere construction for the normal incidence case: The sphere has a radius $|\boldsymbol{k}_0|$, the rods are numbered by their hk value in the reciprocal space, and the green spots represent the intersection of the rods with the phosphor screen. (a) Spots are then formed on the fluorescent screen at the intersections of the rods and the screen. (b) at higher kinetic energies, the Ewald sphere radius increases and more rods cross the sphere, thus more LEED spots are visible [95]. 38

2.13 (a) An image of the LK RVL2000 LEED/Auger system. At the top are 4 grids and a phosphor-coated screen, in the center is the electron gun. (b) A schematic of the LEED/Auger. It is convenient to switch between LEED mode and Auger mode by changing the kinetic energy of the electron primary beam (E_{e^-}), the filer voltage (G_{23}), and screen voltage (V_s) (see text for more details). 39

2.14 Typical LEED patterns of the EG growth on SiC: (a) C-face at 60 eV. The well-known feature of the pattern is a graphene ring which reflects the rotational disorder. (b) Si-face at 75 eV. The special characteristic of the pattern is the six-root-three reconstructions. 40

2.15 A schematic diagram of the Auger effect. The results of the process release either a X-ray photon with its energy $h\upsilon = E_A - E_B$ (top) or an Auger electron with its kinetics $K_E \approx E_A - E_B - E_C - \phi$ (bottom) [97]. 41

2.16 Schematic diagram of the principles of STM: (a) The interactions between tip and surface. The tunneled electrons are primarily from the atomic apex of the tip to the surface due to the quantum mechanics. (b) The tunneling current generated from tip and surface is used as a feedback to control the tip movement [99]. 43

2.17 Room Temperature (RT) STM system in S03 lab. The chamber includes capabilities for scanning tunneling microscopy (STM), low-energy electron diffraction (LEED), CMA Auger electron spectroscopy (AES), ion beam sputtering, residual gas analysis, and a load-lock for tip/sample exchange. 44

2.18 (a) AFM in Keck's lab. (b) Inter-atomic force vs. distance [105]. Depending on different tip-surface working distance, the AFM can operate in the contact or non-contact modes. 46

2.19 Zeiss Ultra 60 FE-SEM at Georgia Tech: (left) a picture of the system. (right) at the bottom is the series of sample holders attached to a big metal plate, at the top is teh in-lens secondary electron (SE) detector. The working distance from the samples to the lens is recommended about 4 mm. 47

3.1 LEED patterns of the reconstructed phases on the hexagonal faces at different prepared conditions. The Si/C ratios, measured by AES signals, indicate the silicon rich interfaces at lower temperature and carbon rich interfaces at higher temperature. (top) Si face with a series three stable phases of (3×3), $(\sqrt{3} \times \sqrt{3})R30°$, and $(6\sqrt{3} \times 6\sqrt{3})R60°$. (bottom) C face with a series three stable phases of $(2 \times 2)_{Si}$, (3×3), and $(2 \times 2)_C$ [109]. 49

3.2 Sketch of the AES model. The incident electron beam strikes along the normal direction. It is attenuated because of collision with the surface atoms to create the core holes. The Auger electrons are detected at the angle $\lambda_0 = 42.2$ due to the CMA design [49]. 51

3.3 Re-plot of the electron multiplier gain versus Auger electron energy from Davis et al [134]. 60

3.4 Sketch of thin films on SiC bulk: AB is the bilayer silicon carbide (depending on C-termination or Si-termination). F is the graphene or silicon overlayers which are epitaxial grown on top of SiC substrate. . 61

3.5 AES model for CMA data to determine the thin film thickness of the epitaxial growth silicon or graphene layers based on the Si:C Auger intensity ratios. A silicon film layer is defined equally to the silicon density in a SiC bilayer ($12.25 \times 10^{14}\,\mathrm{cm}^{-2}$) while the carbon density of a graphene layer is $38.16 \times 10^{14}\,\mathrm{cm}^{-2}$. The solid line is the curve for $SiC(000\bar{1})$ face, the dash line is the curve for $SiC(0001)$ face. Inset is the semi-log plot for the case of determining graphene thickness. . . . 65

3.6 (a) Schematic of two Auger types. (a) The Retarding Field Analyzer (RFA) with three concentric grids in which the inner and outer grids are at ground potential while the middle grid has negative bias (retarding). (b) The Cylindrical Mirror Analyer (CMA) consists of two concentric cylinders in which the inner cylinder is held at ground potential while the outer cylinder is at negative potential. Adapted form [98]. 66

3.7 (a) Raw data from RFA Auger in the growth system. (b) Raw data from CMA Auger in the RT STM system. (c) The RFA data after converted (blue) and the raw CMA data (red). The two data has been subtracted from the constant background and rescaled. 67

3.8 AFM images of the Si-face: (a) Starting surface is atomically flat with regular steps of a unit cell height 1.5 nm. (b) Morphology of the surface after graphitization. The steps are still one unit cell height, and graphene is grown the step edges. 70

3.9 Auger spectra of the Si-face after ex-situ hydrogen etching and annealing at different temperatures in the silane/argon gas mixtures. The starting surface has small oxygen peak which is vanished after annealing. The Si:C ratios decrease as the annealed temperatures increase. . 71

3.10 LEED pattern of the Si face after annealing at 1000 °C for 30 mins: (a) LEED pattern. (b) $(\sqrt{3} \times 7)R30°$ reciprocal lattice. (c) Matching the LEED pattern to the reciprocal lattice. (d) A unit cell of $Si(100)$ on top of $SiC(0001)$ plane in which green, black, and red circles represent Si, C atoms in SiC and Si in Si bulk respectively. 73

3.11 (a) A unit cell of $Si(140)$ on top of $SiC(0001)$ plane. (b) $(2\sqrt{3} \times \sqrt{13})R30°$ reciprocal lattice. (c) Superposition of $(\sqrt{3} \times 7)R30°$ and $(2\sqrt{3} \times \sqrt{13})R30°$ reconstructions. (d) Matching the LEED pattern to the reciprocal lattice. 74

3.12 LEED pattern of the Si face after further annealing at 1100 °C: (a) complicated LEED pattern. (b) $(\sqrt{19} \times \sqrt{21})R36.6°$ reciprocal lattice. (c) Matching LEED pattern to the reciprocal lattice. (d) A unit cell of the reconstruction on top of $SiC(0001)$ plane. 75

3.13 AFM images of the C-face: (a) The starting surface is atomically flat with regular straight steps. A unit-cell height step, $\sim 1.5\,\mathrm{nm}$, includes two half-unit-cell height steps close to each other. (b) Morphology of the surface after graphitization. The step heights are two unit cells. . 77

3.14 LEED patterns on the C-face at various temperatures. (a) (2×2) spots at $1000\,^{\circ}\mathrm{C}$ and $1.4\times10^{-4}\,\mathrm{Torr}$ of silicon ($75\,\mathrm{eV}$). (b) (3×3) spots at $1100\,^{\circ}\mathrm{C}$ and vacuum ($72\,\mathrm{eV}$). (c) (2×2) spots plus graphene ring at $1250\,^{\circ}\mathrm{C}$ and $1.4\times10^{-6}\,\mathrm{Torr}$ of silicon ($60\,\mathrm{eV}$). (d) dimmer (2×2) spots and clear graphene ring when annealing in $1.4\times10^{-5}\,\mathrm{Torr}$ of silicon for additional 30 mins ($60\,\mathrm{eV}$). 78

3.15 Auger spectra of the C-face after ex-situ hydrogen etching and annealing at different temperatures in the silane/argon gas mixtures. The Si:C ratios decrease as the annealed temperatures increase. 79

3.16 LEED patterns of the $(\sqrt{43}\times\sqrt{43})R7.6^{\circ}$ reconstruction: (a) The pattern on the C-face at $100\,\mathrm{eV}$ was reported recently [119]. The sample was prepared by heating in disilane ($5\times10^{-5}\,\mathrm{Torr}$) at $1220\,^{\circ}\mathrm{C}$ for 10 min. (b) The pattern of the C-face surface is acquired at $60\,\mathrm{eV}$. The sample was annealed inside our graphite under $2\times10^{-4}\,\mathrm{Torr}$ silane/argon gas mixtures at $1350\,^{\circ}\mathrm{C}$ for 20 min. 80

3.17 Design of the holders: (a) Vented graphite sample holder of the growth system. (b) Dimensions of the graphite holder in inches. (c) Modified sample holder of the RT STM system. (d) Dimensions of the STM holder. 81

4.1 A $4\times4\,\mu\mathrm{m}^2$ AFM image of the dimple sample after hydrogen etching which is taken near the center of the dimple: (a) graphic image (mean plane subtracted) reveals the equidistant, straight steps. (b) the line profile of the segment on the top figure after applying facet level. It confirms the average step height of a unit-cell of $6H$-SiC, 1.5 nm. . . . 85

4.2 A $10\times7.5\,\mu\mathrm{m}^2$ SEM image of the dimple sample after hydrogen etching taken near the center of the dimple. The scan is captured at primary electron energy of 3 kV, working distance of 8 mm, and aperture size of $30\,\mu\mathrm{m}$. 86

4.3 In-situ characterization of the dimple sample after graphitization: (top) LEED pattern shows the graphene and the $(6\sqrt{3}\times6\sqrt{3})R30^{\circ}$ reconstruction at $60\,\mathrm{eV}$. (bottom) Auger spectrum has Si:C ratio of 0.36. Based on the AAM model, the graphene coverage is one graphene layer. 88

4.4 SEM images taken at various locations inside the dimple sample after graphitization, (a) and (b). The white regions are buffer layers while the dark regions are graphene layers. (c) The average graphene coverage at different locations. The larger the vicinal angle, the higher the graphene coverage. Scan parameters are 3 kV primary electron energy, 8 mm working distance, and 30 μm aperture size. 89

4.5 A $10 \times 10\,\mu\text{m}^2$ AFM image the dimple sample on silicon face after graphitization. (left) Topography of the surface after removing quadratic backgrounds. (right) The line profile of the in the top figure after applying the facet level data. The horizontal lines are the terraces, identified by their shape after background subtraction. . . . 90

4.6 Average step heights at various local angles as suggested in the Table 3. The data are fitted to the power law relation, $a(x - x_0)^b$. The curve fit function provides the value of the parameters: $a = 6.08 \pm 0.14$, $b = 0.47 \pm 0.05$, and $x_0 = 0.12 \pm 0.05$. Inset: The approximate locations of the AFM images inside the dimple. 91

4.7 STM image of a typical sidewall facet on the dimple. (a) The overall step structure of a large step bunch shown in the inset. (b) Atomic resolutions of a region near the step edge with distorted graphene lattices. The inset shows the undistorted graphene lattices on the flat terrace farther way from the step edge. (c) Line profile of the dashed green line in the inset of (a) reveals the step height of 11 nm and facet angle of 22.3°. (d) Undistorted graphene lattices of the top terrace in (a). (e) FFT of (d) showing the $(1 \times 1)_{Gr}$ periods (~ 2.34 Å). Images are acquired at sample biases of -0.6 V (a), -1.0 V (b), and -0.6 V (e) while tunneling current sets at 30 pA. Copyright ©2016 by Yuntao Li. Reprinted with permission [103]. 93

4.8 Schematic step configuration of a vicinal suface in one dimension. The position of the *ith* step is x_i. $n_{s,i}$ is the concentration of adatoms on the *ith* terrace, its width $w_i = x_{i+1} - x_i$. The kinetic coefficients for the ascending and descending step i are K_i^+ and K_i^- respectively. . . 95

4.9 Step trajectories showing the formation of step bunches. The simulation parameters are $N = 50$, $w_0 = 1100$ Å. 102

4.10 Evolution of the average bunch size as a function of growth time. The asymptotic values of these lines depend on the Ehrlich-Schwoebel (ES) barriers. However, the slope of the lines are approximately equal to $\frac{1}{2}$. Fitted lines have slope of 0.49 ± 0.01 (the top line) and 0.52 ± 0.01 (the bottom line). The simulation parameters are $N = 500$, $w_0 = 300$ Å. . 103

4.11 Average bunch size at the different local angles. The data are snapshotted after 150 min and 300 min time of growth of a 500 step system. The solid lines are the fits to power law relation $a(x-x_0)^b$ with $b = .55 \pm 0.04$ (the top line) and $b = .46 \pm 0.05$ (the bottom line). 104

4.12 Pressure-temperature phase diagram for SiC surface. The top dashed line is the silicon vapor pressure over silicon carbide surface in equilibrium [173]. 106

4.13 Kinetic Monte Carlo (KMC) model for the growth of graphene on a vicinal angle: (a) the initial triple-bilayer step structure, (b) the nucleation sites at the step edges, (c) a graphene layer propagating to the left, (d)(e) the graphene layer may "climb over" the upper terrace, (f)(g) two graphene sheets may coalesce upon further propagation, (h)(i) the second layer underneath the first one may then start [148]. 107

4.14 Kinetic Monte Carlo (KMC) model for the growth of graphene on a nano-facet. (a) initial structure of the nano-facet, (b) the nucleation sites at the bottom terrace, (c) a graphene layer propagating up the step, (d)(e) continuing over growth on the upper terrace, (f)(g) the start of the second layer underneath the first one [150]. 107

SUMMARY

The goals of this thesis are to study the growth of epitaxial graphene on both faces of SiC under silane/argon gas mixtures. The first part of the thesis examines on-axis SiC annealed close to the graphitization temperature, below 1350 °C. Experimental results reveal new reconstructions on the Si-face which have not been reported elsewhere, such as $(\sqrt{3} \times 7)R30°$, $(2\sqrt{3} \times \sqrt{13})R30°$, and $(\sqrt{19} \times \sqrt{21})R36.6°$. On the C-face, these studies confirm the well-known (3×3) and (2×2) phases as well as the existence of a $(\sqrt{43} \times \sqrt{43})R7.6°$ reconstruction, which was reported previously by others. The Auger attenuation model is also developed to estimate the graphene or silicon film thickness epitaxial grown on SiC substrates. The next part of the thesis focuses on epitaxial graphene growth on vicinal silicon carbide. Vicinal angles were introduced by grinding a dimple into an on-axis SiC wafer. Atomic-force microscopy of the dimple surface after graphitization shows step bunching, with a power law relation between the average bunch size and the vicinal angle. Scanning electron microscopy of the surface confirms that the growth of graphene starts at step edges, creating sidewall graphene nanoribbons on natural SiC facets. A theory and simulation of a quasi-one dimensional step bunching model are developed to explain the experimental results of the power law relation.

CHAPTER I

INTRODUCTION

1.1 Motivation

Graphene is the first two-dimensional single atomic layer material stably isolated. The single atomic layer is made of sp^2 bonded carbon atoms densely packed in a honeycomb crystal lattice. In fact, graphene is just a single layer of graphite which is well-known and widely available. Notably, a single graphene sheet and its band structure were studied theoretically in 1947 by Wallace [1]. A free standing single atomic layer, however, was predicted by theories to be thermodynamically unstable under ambient conditions [2]. Nevertheless, on metal and semiconducting substrates, graphene ("monolayer graphite") has been known since the 1970s [3, 4]. Such samples remained just interesting surface science experiments until 2004, when unique transport properties were measured for graphene on SiC [5] and for graphene created on SiO_2 through exfoliation of graphite [6]. The latter measurements and technique led to the 2010 Nobel prize in Physics.

Since 2004, graphene has obtained much attention in both theoretical and experimental studies because of its unique properties. The number of academic publications per year related to graphene has grown promptly as shown in Fig. 1.1. According to Web of Science, there were merely 161 publications in 2004 which had their topics related to graphene. However, the number of publications on graphene has increased exponentially every year, and the total number was around $100,000$ in December 2016. The trending of scientific work in graphene has been launched by reporting the multiple methods for producing graphene from lab research to mass production [5–9]. At the same time, a ton of publications points out unique and exciting properties of

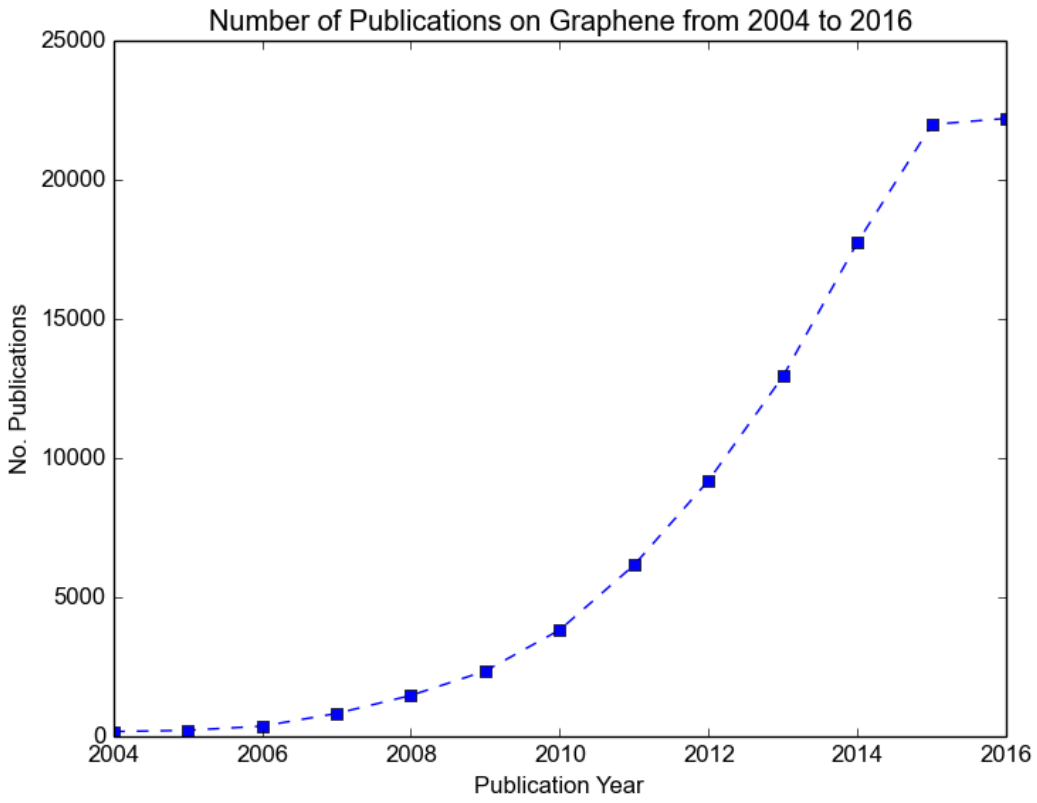

Figure 1.1: Number of publications on graphene from 2004 to Dec. 2016. The graph indicates the exponential increase of graphene publications over a decade. Source from ISI Web of Science (search by topic: TS = Graphene).

graphene [10–14]. Even though there has not had a superior method to achieve a perfect single layer of graphene yet, it still becomes a potential candidate for various future technologies [15]. Furthermore, graphene has also gained the attention of the community through funding to research centers all around the world, mainly in the United States, Europe, and Asia.

Graphene has been considered as a future material to replace silicon in electronics because of its exceptional electrical properties [16]. Intrinsic graphene, characterized as a semi-metal or zero-gap semiconductor, produces a remarkably high electron (hole) mobility at room temperature, from $1100\,\mathrm{cm^2V^{-1}s^{-1}}$ [5] up to $2 \times 10^5\,\mathrm{cm^2V^{-1}s^{-1}}$ [17, 18]. Moreover, it has low thermal (Johnson) noise. The typical value of the

noise is measured $\sim 10^{16}\,\mathrm{V}^2/\mathrm{Hz}$, one order of magnitude below the $1/f$ noise [19]. The combination of high electron mobility and low noise makes graphene an excellent channel in a field effect transistor (FET). Additionally, graphene is mono-atomic-layer-thickness which allows graphene FETs to be scaled to shorter channel lengths and higher speeds [20]. However, a major impediment to graphene electronics is the fact that graphene has no band gap, preventing complete turn-off of conduction in the FET channel.

Many methods have been proposed to prepare graphene of various dimensions, shapes, and quality deposited on different kinds of substrates for specific applications [21]. The mechanical exfoliation technique produces graphene by peeling a small graphite crystallite in a piece of folded scotch tape [22]. The graphite flake becomes thinner and thinner after each time peeling away the tape. Repeating several cycles, we may obtain thin graphene stacks consisting of several graphene sheets and few single layers of graphene. Then, the scotch tape is pressed on an oxidized Si substrate (typically 300nm SiO_2). After carefully removing the tape, the graphene sheets remain stuck to the substrate. Finally, optical microscopy is used to identify mono-layer graphene sheets with a high probability, and an AFM is used to confirm them. This method is extremely simple, but time-consuming, to produce small-size graphene samples used in lab research.

One of the promising methods to produce graphene, potentially on a large scale, is chemical vapor deposition (CVD) growth on transition metals. In this approach, carbon-containing gases, such as methane, ethane, or propane, decompose on a catalytic metal (Cu, Ni, Ir, Ru, Co, etc.) surface at high temperature and convert to graphene [23]. Despite the cost-effective and large-scale production, many issues need to be solved. The first concern is the quality of graphene itself such as defects, dislocations, grain boundaries, uniforms, and so on. Furthermore, graphene

may be contaminated with metals, which can degrade the quality of graphene. Importantly, the graphene films need to be transferred onto an appropriate substrate for characterizations and operations. The transfer processes, potentially damage and degrade graphene films, are far from perfect and require further studies to improve and optimize for practical applications.

To utilize graphene as a platform for graphene-based electronics, epitaxial graphene (EG) growth on SiC substrates emerges as one of the most suitable mass production methods. The confinement controlled sublimation (CCS) method, widely performed at Georgia Tech, can produce uniform EG layers with impressive quality [5, 24]. In this technique, a SiC wafer (6H or 4H polytype) is annealed inside a nominally closed graphite furnace at high temperature (around 1400C) under external gases (Ar, silane, etc.) overpressure. At the growth temperature, the sublimating silicon leaves the surface and the remaining C forms a graphene film on the SiC substrate. No transfer needed for device processing is a key advantage of this method. Also, as shown later in this thesis, the detailed kinetics of graphene growth on the $SiC(0001)$ surface enables the creation of quasi-one-dimensional graphene nanoribbons. These "sidewall" nanoribbons have been shown to have the property of ballistic current transport [25].

1.2 Physical Properties of Graphene

Carbon, the most important element to living things, is the sixth element of the periodic table. In the atomic ground state, there are 6 electrons which are in the configuration $1s^2 2s^2 2p^2$. As we know, the inner shell $1s^2$ is close to the nucleus, then, two electrons filling this shell are irrelevant for chemical reactions. On the other hand, the remaining 4 electrons occupy the outer shell of $2s$ and $2p$ orbitals which have total 8 possible states ($2s$, $2p_x$, $2p_y$, $2p_x$, moreover, each orbital has two eligible states due to a spin up or down). Because of the small energy gap between the $2s$ and $2p$ orbitals (around 4 eV), one of the $2s$ electrons can be promoted to the empty $2p$ orbital. As

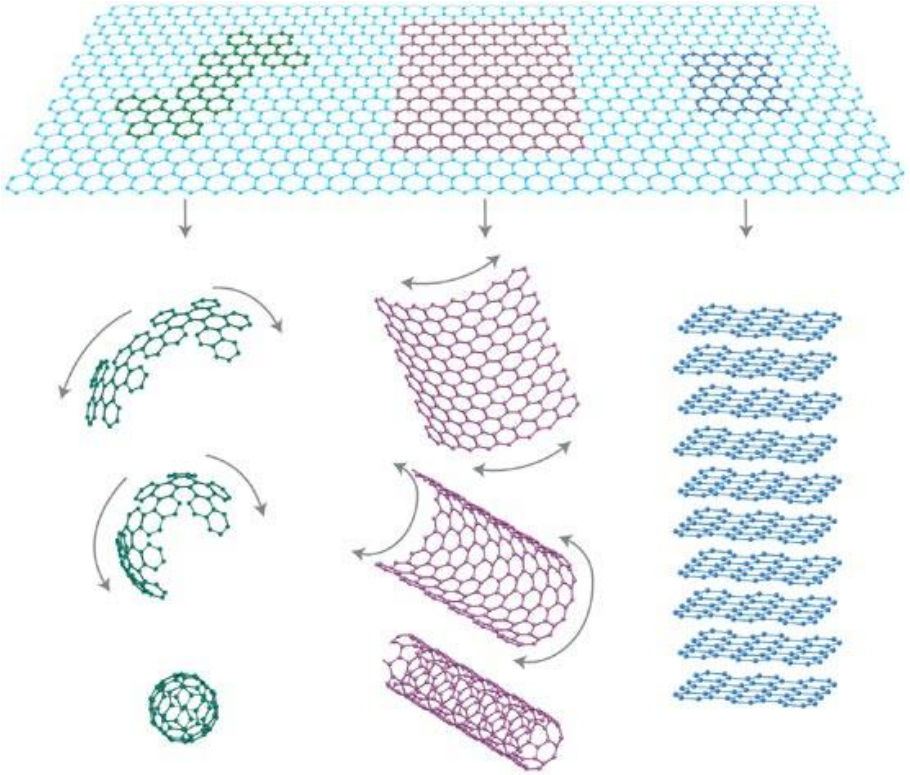

Figure 1.2: Graphene is a $2D$ building block for all of other graphitic allotropes: $0D$ buckyballs (wrapped), $1D$ nanotubes (rolled), and $3D$ graphite (stacked) [26].

the results, carbon has three hybridizations sp^1, sp^2, and sp^3 corresponding to the number of the $2p$ orbitals mixing with the $2s$ orbital.

Graphene is made of sp^2 hybridization of carbon in which one $2s$ and two $2p$ orbitals are hybridized to form three in-plane covalent σ bonds. Similar to benzene molecule configurations [27], all σ bonds in graphene are trigonal-planar symmetry with 120° angles. Moreover, the $C-C$ distance in graphene is $0.142\,\text{nm}$ for all bonds (nearly the same as for the Benzene molecule) which is roughly the average length of a single bond ($C-C$: $0.147\,\text{nm}$) and a double bond ($C=C$: $0.135\,\text{nm}$). Because of the strong covalent σ bonds, the in-plane properties of graphene/graphite make it the strongest material ever measured: a Youngs modulus of $E = 1.0\,\text{TPa}$, third-order elastic stiffness of $D = -2.0\,\text{TPa}$, and intrinsic strength of $\sigma_{int} = 130\,\text{GPa}$ [28, 29]. In contrast, the remaining unhybridized $2p_z$ orbital, perpendicular to the σ bond plane,

forms π bonds. Each carbon atom of the graphene lattices contributes one electron to this electronic band so that it is only half-filled. Because of the small overlap between these orbitals, the out-of-plane π bond is much weaker than the covalent σ bond. As the results, the weak-coupled π bond is responsible for the high electron (hole) mobility of the graphene because of the ease of movement of electrons (holes) in these π states.

Two-dimensional graphene ($2D$) is the building block for all of the graphitic allotropes: three-dimensional graphite ($3D$), one-dimensional nanotubes ($1D$), and zero-dimensional buckyballs ($0D$) (Fig. 1.2). The buckyballs (fullerenes) were predicted theoretically in 1970 by Eiji Osawa and discovered experimentally in 1985 [30]. The C_{60} molecule, the most prominent representative of $0D$ allotropes, is formed by wrapping a graphene sheet by replacing some hexagons with pentagons. Carbon nanotubes, discovered in 1991 [31], may be viewed as graphene sheets rolled up with a diameter of several nanometers. On the other hand, graphite is a stacking of graphene sheets that stick together due to the weak van de Waals interaction. Conversely, graphene sheets can be obtained by unwrapping single wall carbon nanotubes or exfoliating graphite crystals.

Graphene's honeycomb lattice is the combination of two triangular Bravais lattices. The honeycomb lattice itself is not a Bravais lattice because of two nearest neighboring (nn) sites are not equivalent; however, it may be viewed as a triangular Bravais lattice with a two-atom basis (A and B) (Fig. 1.3). As we pointed out previously, the distance a between two nn carbon atoms is 0.142 nm, hence, the triangular Bravais lattice is spanned by the basis vectors

$$\boldsymbol{a}_1 = \sqrt{3}a\boldsymbol{e}_x, \qquad \boldsymbol{a}_2 = \frac{\sqrt{3}a}{2}(\boldsymbol{e}_x + \sqrt{3}\boldsymbol{e}_y) \tag{1.1}$$

It is straight forward to gain the lattice spacing, $\tilde{a} = \sqrt{3}a = 0.246\,\text{nm}$, and the unit cell area, $A = \sqrt{3}\tilde{a}^2/2 = 0.052\,\text{nm}^2$. Therefore, the density of the carbon atoms,

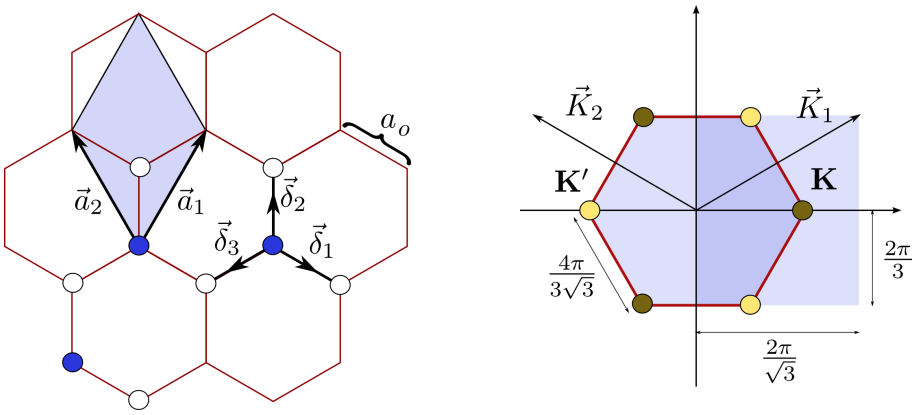

Figure 1.3: Graphene's crystal lattice and first Brillouin zone. On the left is the honeycomb lattice of graphene, with the two sublattices denoted by colored circles. The triangle Bravais lattice has two basis vector $\boldsymbol{a}_1$ and $\boldsymbol{a}_2$. On the right is the first Brillouin zone of graphene, with two inequivalent points K and K' (Dirac points) [32].

equivalent to the π electron density in charge-neutral graphene, is $n_C = 2/A = 3.8 \times 10^{15}\,\mathrm{cm}^{-2}$. The reciprocal lattice of the triangular Bravais lattice has basis vectors

$$\boldsymbol{a}_1^* = \frac{2\pi}{\sqrt{3}a}(\boldsymbol{e}_x - \frac{\boldsymbol{e}_y}{\sqrt{3}}), \qquad \boldsymbol{a}_2^* = \frac{4\pi}{3a}\boldsymbol{e}_y \tag{1.2}$$

One can easily check the relation between direct and reciprocal lattice vectors is held, $\boldsymbol{a}_i.\boldsymbol{a}_j = 2\pi\delta_{ij}$ (for $i, j = 1, 2$)). In the reciprocal space, the first Brillouin zone (BZ) represents a set of inequivalent points, which can not be connected to one another by a reciprocal lattice vector. In the graphene case, the first BZ consists of some special points corresponding to the physically distinguishable lattice excitations. The Γ point is located at the center of the first BZ and is responsible for long wavelength excitations. The two inequivalent points K and K' are located at the two neighboring corners of the first BZ ($\boldsymbol{K}, \boldsymbol{K'} = \pm\frac{4\pi}{3\sqrt{3}a}\boldsymbol{e}_x$) and have low-energy excitations. Lastly, the three inequivalent M points are in the middle of the BZ edges.

The electronic band structure of graphene was originally calculated using the tight-binding approximation (Wallace, 1947 [1]). As discussion before, the ease of movement of the π electrons is responsible for the electronic properties at low energies,

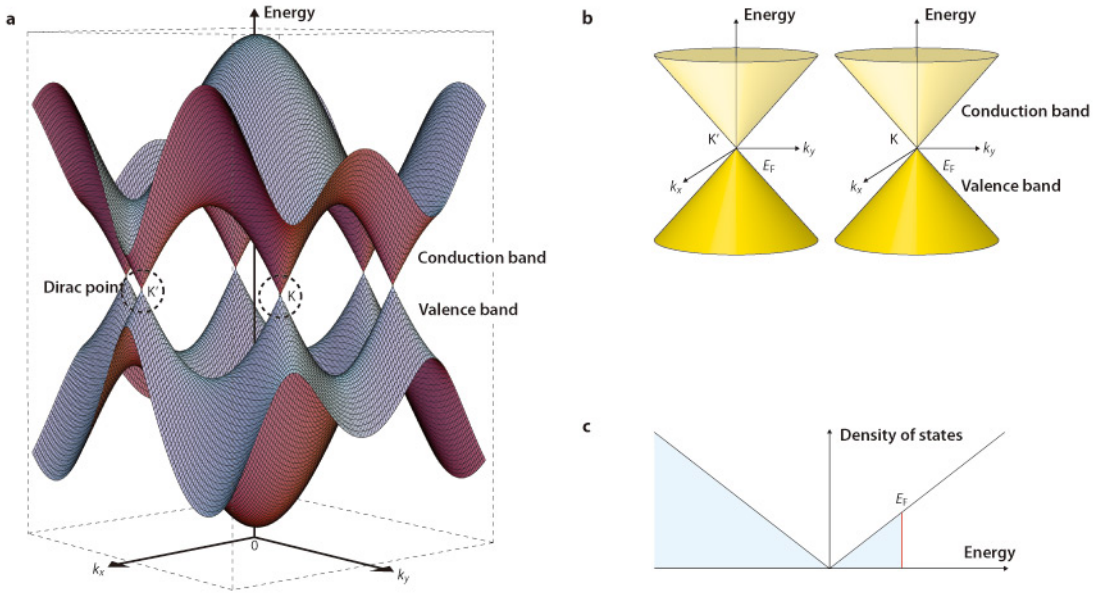

Figure 1.4: Graphene band structure. The Dirac points are the places where the upper edge of valance band and lower edge of conduction band meet. Those are six points at the six corner of the first Brillouin zone in which only two of them, K and K', are inequivalent. Near the Dirac points, the band structure is linear at the Dirac points [33].

i.e., close to the Fermi energy. by ignoring the band structure of the strong σ bonds, the energy bands of π electrons are calculated straightforwardly by using the tight-binding method. Taking into account Bloch's theorem, one can write down the energy dispersion $E(k_x, k_y)$ of π electrons in an analytic expression:

$$E(\boldsymbol{k}) = \pm t\sqrt{3 + 2\cos(\sqrt{3}k_x a) + 4\cos(\sqrt{3}k_x a/2)\cos(3k_y a/2} \tag{1.3}$$

in which $t \approx 3\,\text{eV}$ is the nn hopping integral in graphene. The dispersion relation of graphene in the first BZ is plotted in Fig. 1.4. There are two different π bands corresponding to two π orbitals in each graphene unit cell: a valence band (π) and a conductions band (π^*). Contrary to the usual parabolic shape, the dispersion relation near the K and K' points is linear:

$$E(\boldsymbol{k}) = \pm\hbar(\frac{3ta}{2\hbar})|\boldsymbol{k}| = \pm\hbar v_F|\boldsymbol{k}| \tag{1.4}$$

Quantity	3C-SiC	4H-SiC	6H-SiC	Silicon [28]
E_g (eV) ($T < 5$ K)	2.40 [19]	3.26 [27]	3.02 [27]	1.12
E_{crit} (MV cm^{-1})	2.12 [29]	2.2 [29]	2.5 [29]	0.25
$\Theta\kappa$ (W cm^{-1} K^{-1}) at 300 K†	3.2 [32]	3.7 [33]	4.9 [33]	1.5
n_i @ 300 K (cm^{-3})‡	1.5×10^{-1}	5×10^{-9}	1.6×10^{-6}	1.0×10^{10}
v_{sat} (cm s^{-1}) parallel to c-axis		2.0×10^{7} [10]	2.0×10^{7} [30]	1.0×10^{7}
μ_e (cm^2 V^{-1} s^{-1})	800 [20]	1000 [35]	400 [35]	1400
$(\mu_\perp)/(\mu_\parallel)$ at 300 K		0.7–0.83 [34]	6 [35]	
μ_h (cm^2 V^{-1} s^{-1})	40 [37]	115 [38]	101 [38]	471
ε_s	9.72 [40]		9.66 [40]	11.7

†Doped at $\sim 10^{17}$ cm^{-3}.
‡Effective mass values found in Refs [34, 35], and E_g with respect to T in Ref. [36].

Figure 1.5: Comparison of some important electrical properties of silicon carbide and silicon material. All of three common silicon carbide polytypes possess superior properties for high-temperature, high-power, and high-frequency applications [38].

where the Fermi velocity $v_F \approx 10^6$ m/s is a constant which depends on the lattice constant a and the nn hopping energy t only. Those two points, where the two band π and π^* touch each other, are called Dirac points because of the linear relationships near them. It is worth to mention that a Dirac point is double degenerated because of the symmetry $E(\boldsymbol{k}) = E(-\boldsymbol{k})$, which is a consequence of time-reversal symmetry.

A drawback of graphene for application in digital electronics is the absence of a band gap. Moreover, the linear dispersion relation near the Dirac points makes an electron as a massless fermion that is hard to confine with electrostatic potentials. Many methods have been considered in the literature to overcome these issues: stacks of graphene layers (bilayer graphene) [34], chemical doping [35], strain induced band gaps [36], and lateral-confinement induced band gaps [37]. The last approach drives scientists to find the best way to produce graphene nanoribbons (GNRs). GNRs have been grown epitaxially on SiC facets using Confinement Controlled Sublimation (CCS) method at Georgia Tech [25].

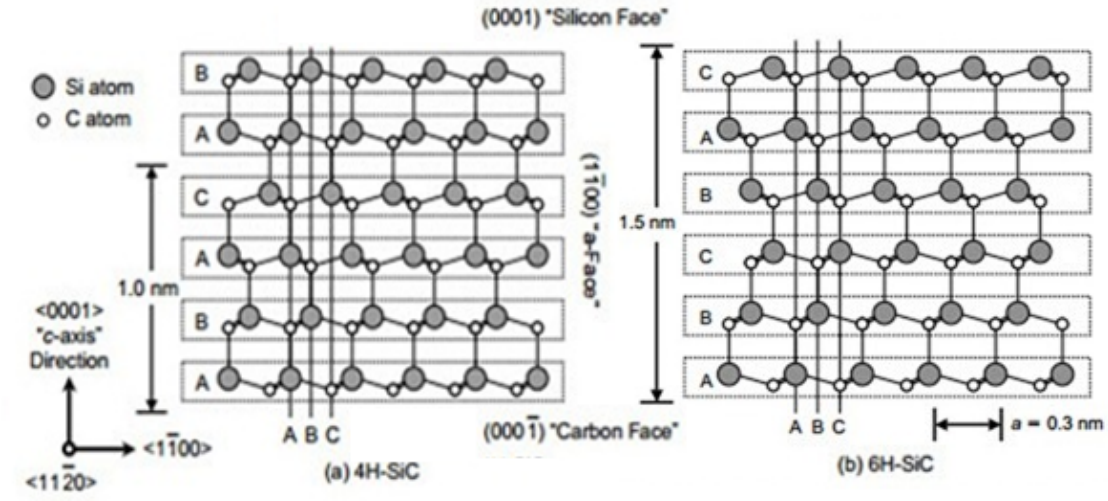

Figure 1.6: Crystal structure of $4H$- and $6H$-SiC displayed parallel to the $(11\bar{2}0)$ plane: The big filled circle denotes a Si atom and the small white circle denotes a C atom. On the left is the $4H$-SiC with the unit cell height of 1.0 nm and on the right is the $6H$-SiC with the unit cell height of 1.5 nm. The top is the silicon-terminated face and the bottom is the carbon-terminated face [39].

1.3 Hexagonal Silicon Carbide

SiC itself is a material of interest because of its wide band gap (2.0 eV−7.0 eV, depending on the polytype [38]). It is a semiconductor with potential for high-temperature, high-power, and high-frequency applications. Fig. 1.5 reveals some basic electrical properties of common silicon carbide polytypes in comparison with silicon [38]. According to this table, SiC has higher thermal conductivity Θ_κ, greater electric field breakdown strength, and wider band gap than Si. Thus, SiC is an excellent substrate for high-temperature operation of integrated circuit technologies. Even though there are over 250 polytypes of SiC known, this thesis exclusively uses hexagonal $4H$ and $6H$ polytypes as substrates for epitaxial growth of the thin films.

Figure 1.6 shows the crystal structure of $4H$-SiC and $6H$-SiC, in which each carbon atom bonds with 4 different silicon atoms and vice versa. One layer of carbon atoms and that of silicon atoms close to each other are called a bilayer. In each bilayer, the carbon-silicon bond length is 1.89 Å, and the closest distance between two carbon

atoms is $a_{SiC} = 3.08\,\text{Å}$ [40]. Thus, the density of carbon atoms for each bilayer is $\rho_{SiC} = 2/(\sqrt{3}a_{SiC}^2) = 1.22 \times 10^{15}\,\text{cm}^{-2}$, which is approximately equal to one-third of carbon density in single-layer graphene. In other words, three (more accurately 3.14) SiC bilayers generate enough carbon atoms to form a graphene layer. The distance between two bilayers is 2.52 Å. As a result, $4H$- and $6H$-SiC have a unit cell height of 10.08 Å and 15.12 Å respectively. The stacking sequences of $4H$- and $6H$- SiC are ABAC... and ABCBAC... respectively in the Ramsdell type notation [41]. The plane of a bilayer sheet is defined as the basal plane (or hexagonal plane), and the stacking direction is perpendicular to it. If the hexagonal SiC crystal is cut by the basal plane, there are two possible surface terminations: the silicon-terminated face is denoted as $SiC(0001)$, and the carbon-terminated face is denoted as $SiC(000\bar{1})$.

1.4 Epitaxial growth

The ability to grow ultra-thin films is crucial nowadays for electronic devices and applications. Epitaxial growth, the deposition of a crystalline layer on the surface of a crystalline substrate, is widely used in both research and industry. The substrate wafer acts as a seed crystal, thus influencing the crystallographic orientation of the epitaxial film. If the film and the substrate are the same material, it is called homoepitaxial, in other cases, it is called heteroepitaxial. In the latter case, the mismatch between the film and the substrate crystal lattices introduces lattice strains which will alter the properties of the thin films. The lattice misfit m, defined as $m = (a_{film} - a_{sub})/a_{sub}$, is an important parameter for determining the equilibrium structure and morphology of a heteroepitaxial thin film. The smaller the misfit value is, the lower the strain energy is, and the fewer the defects are in the epitaxial film.

There are three common techniques used in epitaxial processes: chemical vapor deposition (CVD), molecular beam epitaxy (MBE), and liquid phase epitaxy (LPE). In CVD, source materials are supported by containing-element gasses, and metal

substrates are heated to high temperature. In MBE, one or more evaporated beams of atoms impinge on the substrate to form a film under ultra-high vacuum conditions. On the other hand, LPE is a method to grow a crystalline film from a supersaturated melt onto a substrate. The precursor molecules, which are dissolved in the melt of the substrate, precipitate to form thin films when reducing the substrate temperature.

Regarding to the thermodynamics, there are three growth modes of epitaxy depending on the macroscopic surface tensions: γ_{sub} (substrate/vacuum interface), γ_{fil} (film/vacuum interface), and γ_{int} (film/substrate interface) [42]:

1. The Frank-van der Merwe (FM) growth mode [43]: $\gamma_{sub} > \gamma_{fil} + \gamma_{int}$. Forming a film reduces the total surface energy, thus leading to layer-by-layer growth (a new layer starts to grow only when the preceding one is finished).

2. Volmer-Weber (VW) growth mode: $\gamma_{sub} < \gamma_{fil} + \gamma_{int}$. In contrast to FM mode, growing a film increases the interface surface energy and its surface energy, thus making a priority to form $3D$ islands.

3. The Stranski-Krastanov (SK) growth mode. It is the mixture of the two previous modes. It initially has : $\gamma_{sub} > \gamma_{fil} + \gamma_{int}$, however, eventually it becomes: $\gamma_{sub} < \gamma_{fil} + \gamma_{int}$ due to the strain effects. As the results, the first few layers grow (as in FM mode), and latter islands are created as a result of the mismatch in lattice constants (as in VW mode).

Epitaxial thin film growth can be understood through the atomic diffusion process. An adatom diffuses on the surface by jumping from one lattice site to the adjacent lattice sites. The jump rate of a diffusion process is given by the Boltzmann statistics $\nu = \nu_0 \exp(-E_n/k_B T)$, where $\nu_0 \approx 10^{12} - 10^{13}$ Hz is the attempt frequency (typically in the range of the Debye frequencies), E_n is the activation energy. Fig. 1.7 shows the typical diffusion process of an adatom arriving on the crystal surface. The adatom moves on the terrace or along the step until it meets either another adatom to form

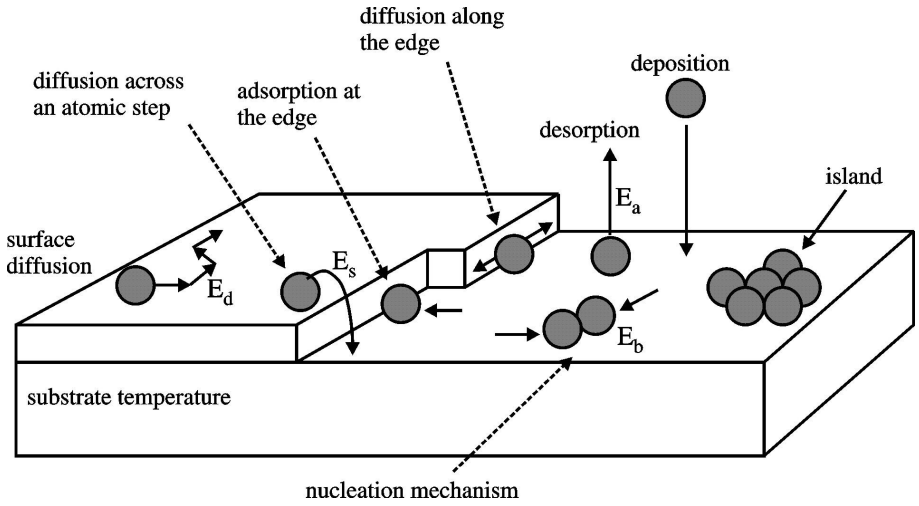

Figure 1.7: The atomic diffusion process of epitaxial thin film growth. The adatom can move on the terrace or along the step until it meets either another adatom to form a island (nucleation) or an existing island to stick to it (growth) [44].

an island (nucleation) or an existing island to stick to it (growth). As a result, the larger the diffusion coefficient D, the lower the island density.

Despite many different approaches to studying the surface properties and evolution, there are two extremes: (i) atomistic descriptions (at the microscopic level), and (ii) continuum descriptions (at the macroscopic level). At the atomic scale, the motions of individual atoms on the surface are governed by their hopping energies with different lattice sites. The Kinetic Monte Carlo (KMC) model is the appropriate approach to this level. On the other hand, the continuum step model has proven to be powerful at macroscopic level where the steps and terraces are treated continuously. This approach considers an individual step as the fundamental element of the growth process and focuses on its motion as the only way of the surface evolution. In this thesis, the quasi-1D step model, known as Burton-Cabrera-Frank (BCF) theory, has been studied extensively in the chapter 4 to explain the silicon carbide step bunching and graphene growth at variable vicinal angles on a dimple sample.

1.5 Epitaxial Graphene (EG) Growth on Silicon Carbide

Because SiC is suitable for high-temperature, high-power applications, epitaxial graphene growth on SiC substrates is an attractive method for electronic devices [45–48]. In principle, when annealing a SiC crystal at high temperature ($\sim 1400°C$), silicon atoms evaporate from the surface, and the remaining carbon atoms form graphene sheets on the top of the SiC substrate. Unlike all traditional thin-film growth methods, where the material deposition rate and the surface diffusion rate are controlled separately, epitaxial graphene growth in vacuum is determined by a single parameter: the substrate temperature. Thus, the key challenge for obtaining high-quality monolayer graphene is to decouple the carbon surface diffusion rate and the carbon deposition rate (i.e. the silicon sublimation rate). In the case of the growth of EG on SiC in ultra-high vacuum (UHV), the two rates are dependent on each other, and the growth process is far from equilibrium. Upon SiC annealing, silicon atoms leave the surface at a high sublimation rate which leads to inhomogeneous graphene layers [49]. It has known that the higher annealing temperature is, the more uniform graphene layers are formed, because of the higher kinetic energy and mobility of carbon atoms. However, at very high temperature, it is difficult to control the exact numbers of graphene layers [50]. Thus, controlling the silicon sublimation rate is necessary to increase growth temperature, while slowing down the growth process is the key to gain homogeneous graphene layers.

The confinement Controlled Sublimation (CCS) method, used by Georgia Tech research groups since 2002 [51], suppresses silicon sublimation rate by controlling the silicon vapor pressure over silicon carbide. The silicon carbide samples are inserted into a graphite furnace which is enclosed except for a small hole that allows vapor transport. The furnace is nominally in vacuum, with the possibility to introduce an inert gas (argon), or a silicon-containing gas (silane). These ambient conditions limit the escape of silicon from the surface, thus maintaining a high silicon vapor

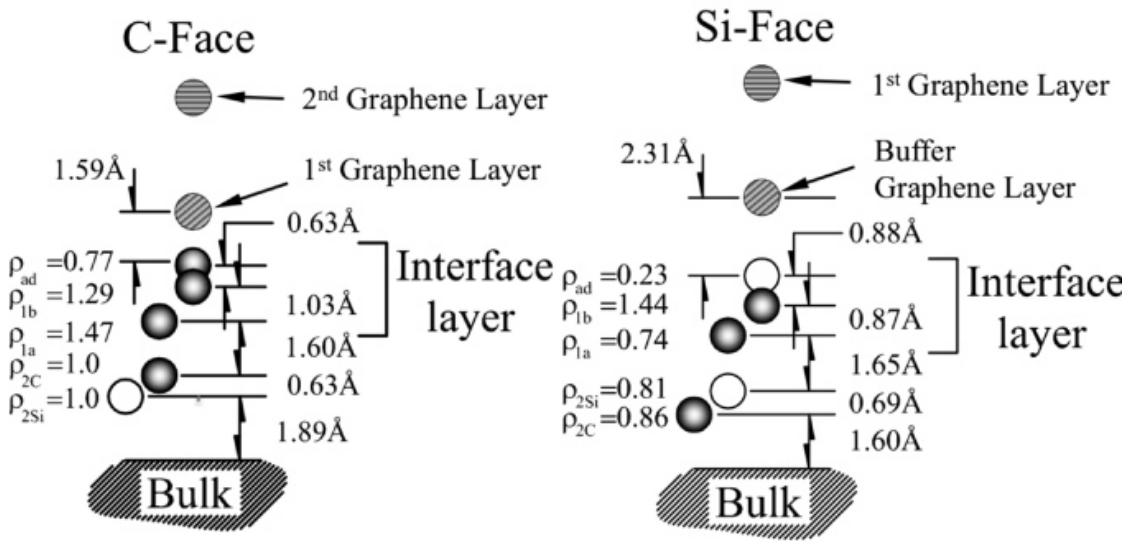

Figure 1.8: Structure models of the interface layers of epitaxial graphene on the two polar faces of SiC. Solid circles represent carbon atoms, open circles are silicon atoms and lined circles are graphene carbon atoms [64].

pressure. As a result, the EG growth proceeds close to thermodynamic equilibrium. The quality of the resulting homogeneous graphene layers has been tested via many surface science tools such as STM, AFM, LEED, etc [24, 52–58].

The growth mechanism of EG on the C-face is significantly different from the one on the Si-face [59–61]. One of the reason is that the surface energy on the C-face ($300\,\mathrm{erg/cm^2}$) is much less in comparison with the surface energy on the Si-face ($2220\,\mathrm{erg/cm^2}$) [62]. Thus, EG growth on the C-face is faster and less controllable than on the Si-face. Multiple graphene layers (up to 100 layers) are observable in C-face grown, and monolayer graphene, while monolayer growth on the C-face is difficult to achieve. Conversely, monolayer graphene is easily grown on the Si-face of SiC [63]. Moreover, graphene synthesized on the C-face is weakly attached to the SiC substrate. In contrast, the first carbon layer grown on the Si-face is covalently bound to the underlying SiC bilayer; this layer is called zero-layer, buffer layer, or interface layer graphene (Fig. 1.8).

1.5.1 Silicon faces: zero-layer graphene

EG growth on the Si-face is the method of choice to produce single layer graphene because of the easy control of graphene thickness. Due to the slower growth rate on the Si-face plus introducing silicon overpressure, the CCS method easily controls the desired number of graphene layers, and even a single layer can be achieved. When annealing to high temperature, Si sublimation leave the C atoms to form a C-rich $(6\sqrt{3} \times 6\sqrt{3})R30^\circ$ structure ($6\sqrt{3}$ layer for short) which has the same honeycomb structure of graphene. The $6\sqrt{3}$ zero-layer (or buffer layer), served as an interlayer between graphene and the SiC substrate. The reconstructed layer is strongly connected to the substrate due to about 30% the carbon atoms covalently bonding to silicon atoms of the SiC bilayer [11]. Because of this strong coupling with the substrate, a buffer layer does not possess the exceptional properties of the freestanding graphene. However, the buffer layer has an important role in ensuring that well-ordered graphene grows subsequently on this face. By further Si sublimation, a second $6\sqrt{3}$ layer is formed under the first one, thus decoupling the initially-grown layer from the substrate and forming "layer 1", i.e., monolayer graphene. This is called a bottom-up growth process [65]. Moreover, it is possible to separate the buffer layer from the bulk and obtain a quasi-free-standing graphene layer by introducing intercalant atoms of hydrogen, silicon, etc [11, 66].

Figure 1.8 shows structural models of the interface layers between graphene and silicon carbide on both polar faces. On the Si face, the distance from the buffer layer to the Si-terminated SiC surface is about 2.3 Å. The distance between the buffer layer and the first graphene layer is about 3.5 Å, which is close to the graphite inter-planar spacing of 3.35 Å [50, 67]. In addition, graphene layers on the Si face are stacked with a 30° rotation [68]. Few-layer graphene (FLG) has electronic properties dependent on the stacking sequence. Bilayer graphene has Bernal AB stacking, and trilayer graphene has two stable stacking sequences of ABA and ABC [50].

1.5.2 Carbon faces: multiple layer graphene

The growth rate of graphene on the C-face is relatively fast, a 4-5 layer graphene film forms in $\sim 6\,\text{min}$ at $1420°C$ [69, 70]. Under UHV conditions, the number of graphene layers grows rapidly above a threshold temperature [69]. Thus, a thin graphene film is difficult to obtain because of the limitation in rapid temperature control and measurement. However, the graphene is weakly bonded to the SiC substrate. The first graphene layer is separated at the distance of about 3.2 Å from SiC bilayer (based on the TEM results reported from J. Borysiuk et al. [71]), which is much bigger than $C-C$ covalent bonds.

The energy band structure of each layer is linear, which is similar to the one of the freestanding monolayer graphene [72]. ARPES measurements have confirmed that the multiple graphene layers grown on the C-face behave essentially as independent monolayers of graphene. The relatively weak interaction between multiple graphene layers is the result of the rotational stacking. The first graphene layer rotates at $30° \pm 7°$ to the SiC substrate; the next graphene layer has a random twisted angle from the first one [73]. The graphene ring in the LEED patterns and the moiré superlattices in STM images also confirm the rotational stacking.

1.5.3 Sidewall graphene nanoribbons (GNRs)

Graphene nanoribbons are proposed as a mean to open an energy band gap and to create a transport channel for electronic applications [74, 75]. It is well known that the lateral quantum confinement of charge carriers (electrons and holes) leads to discrete energy states. Specifically, the energy band gap of a GNR is inversely proportional to its width and length [25]:

$$E_{n,m} = \pm\hbar v_F \sqrt{(\frac{n\pi}{W})^2 + (\frac{m\pi}{L})^2} \tag{1.5}$$

where $v_F \approx 10^6\,\text{m/s}$ is the Fermi velocity, $\hbar$ is the Planck's constant divided by 2π, and W, L are the width and length of the ribbons respectively. Thus, the narrower

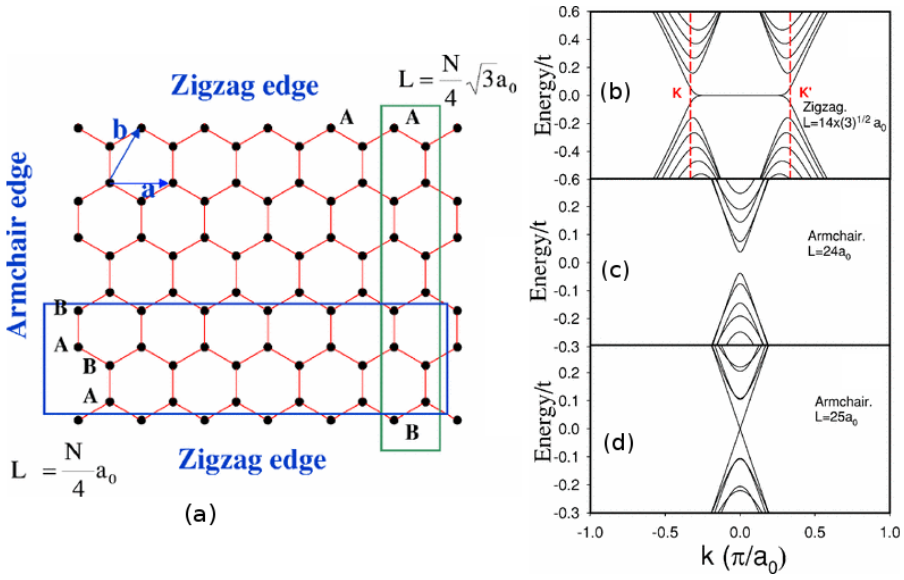

Figure 1.9: (a) The lattice structure of a graphene sheet with armchair and zigzag edges. Top and bottom edges are zigzag, left and right edges are armchair. (b),(c),(d) Energy bands for a graphene nanoribbon with a typical length, L, and edges. The band structure of zigzag nanoribbon is always metallic while that of armchair nanoribbon is either metallic or insulating [78].

is the GNR, the bigger is the bandgap, and the higher is the on/off ratio that could be achieved by a GNR FET. Research confirms that a sub-10 nm GNR FET reaches an on/off ratio of 10^7 [76]. On the other hand, the band gap, as well as the carrier mobility and other electronic properties of the GNR, is also dependent on the edge configuration of a ribbon. Depending on the orientation of cutting from a $2D$ graphene sheet, the edge of a $1D$ GNR can be armchair (AGNR) or zigzag (ZGNR) (Fig. 1.9). In general, the band structures of AGRNs are either metallic or insulating depending on the ribbon widths, while these of ZGNRs are always metallic [77–79].

Although many methods have been proposed to fabricate GNRs, epitaxial sidewall GNR growth on SiC nanofacets, conceived at Georgia Tech, is one of the most promising approaches to obtain high-quality GNRs for electronic devices [80]. The 40-nanometer-wide sidewall GNRs possess exceptional ballistic transport properties with electron mean free path greater than 10 μm at room temperature [25, 81].

The selective growth of graphene relies on the preferential sublimation of Si atoms

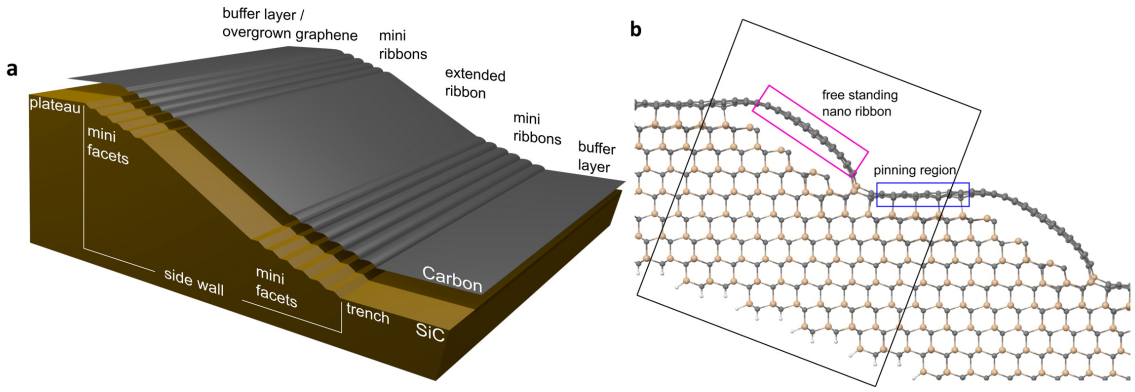

Figure 1.10: Model of armchair sidewall graphene nanoribbons (GNRs): (a) The schematics of the sidewall which is composed of an extended facet in between several bottom and a top minifacets. (b) Atomic structure model of the sidewall GNRs which have free standing nano ribbons on the facets [82].

from the nanofacet, and then the remaining C atoms are self-assembled to form graphene layers on top of it. Figure 1.10 shows the schematics of the model proposed for the general structure of armchair graphene nanoribbons grown on the Si-face of a SiC wafer [82]. The sidewall is composed of an extended facet in between several bottom and top minifacets. The extended facet corresponds to a 30° off normal with respect to the $SiC(0001)$ plane (corresponding to $[1\bar{1}07]$ plane), the minifacets have a normal tilted $\sim 20°$ from the $SiC(0001)$ plane (corresponding to $[1\bar{1}0n]_{n=9,10}$ planes). As shown in the figure, graphene is bonded to the substrate in between the flat terraces and the SiC facets. However, it is floating without any strain (free standing) in between these pinning areas. Further investigation confirms that the growth of graphene initially starts at the bottom edge and hence continues overgrowth through the top edge of the facet [83]. In this thesis, I perform the experiments of the epitaxial growth of sidewall GNRs on natural facets which are self-created during the growth process. The details of experimental results and theoretical explanations are found in Chapter 4.

1.6 Thesis Outline

In Chapter 2, I present the sample preparation processes, the home-made growth system, and surface characterization tools used in the thesis. The samples are either $4H$- or $6H$- silicon carbide wafers which are on-axis or off-axis with variable vicinal angles. The growth techniques and equipment, including the growth chamber, gas-line system, and temperature device, are also presented. In the end, I mention some sample characterization techniques which are used in the thesis such as the in-situ LEED, AES and the ex-situ STM, AFM, SEM.

Chapter 3 is devoted to silicon deposition on on-axis silicon carbide substrates at lower graphitization temperature. I found new reconstructions on the Si-face which have not been reported elsewhere. On the C-face, the reconstructions were in agreement with previous results. In addition, an Auger attenuation model was developed to determine the thickness of both silicon and graphene thin films based on the Auger peak intensity ratio, Si:C. I also propose a routine to convert the Auger data acquired by a retarding field analyzer (RFA) for direct comparison to data acquired using a standard cylindrical mirror analyzer (CMA).

Finally, Chapter 4 studies epitaxial graphene growth on vicinal silicon carbide. I present the morphology of the dimple on a $6H$-SiC wafer after annealing in the argon/silane gas. The experimental outcomes showed a power law relation between the average bunch size and the local surface angle. I developed a quasi-one-dimensional step-bunching model based on the BCF theory and ran simulations to explain this result.

CHAPTER II

EXPERIMENTAL METHODS

This chapter describes the sample preparation processes, the home-made growth system, and the surface characterization tools as a background for the thesis. The samples were hexagonal silicon carbide wafers with initial on-axis facets. Then, a concave-shaped dimple was ground on top of a SiC sample to create a variety of vicinal angles. These samples were treated by using hydrogen etching at high temperature, $\sim 1450 - 1500^{\circ}$ C, to reduce scratches and form regular steps. After verified the atomically flat surface via AFM, they were inserted into a graphite sample holder and transferred into the ultra-high vacuum (UHV) system. There was a transfer arm to grasp the holder then mounting it into the graphite furnace placed inside the growth chamber. The furnace was annealed by a radio frequency (RF) heater, and the whole chamber was backfilled with ambient gasses by leaking the valve connected to the gas-line system. During the growth process, the temperature was monitored by a thermocouple or an infrared pyrometer. Finally, the samples were characterized by in-situ a LEED/Auger system, and ex-situ AFM, SEM, STM, etc.

At the beginning of the chapter, I illustrate the sample preparation processes in section 2.1. The dimple grinding method wasused for making a $30\,\mu$m hole at the middle of an on-axis SiC sample. The hydrogen etching technique, the method of choice for preparing atomically flat surfaces, is described briefly. In the section 2.2, I introduce the home-made growth system in our lab. The system includes the growth chamber, gas-line connections, and in-situ LEED/AES characterization equipment. I also report my experiments to calibrate the growth temperature for achieving reliable measurement. Lastly, section 2.3 introduces shortly some of the surface science tools

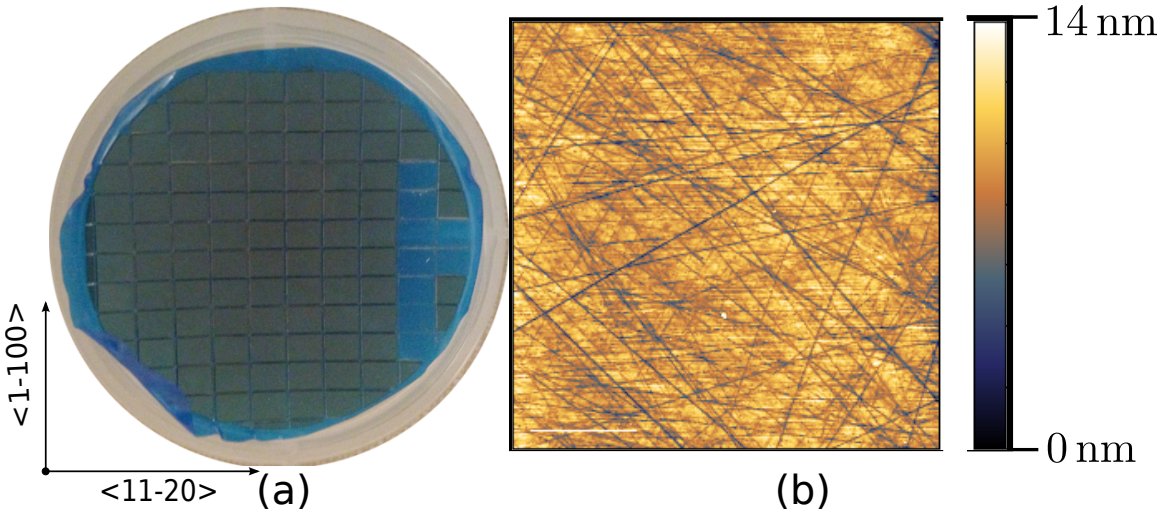

Figure 2.1: (a) A $6H$-SiC wafer, purchased from Cree Inc, was diced into $3.5 \times 4.5\,\mathrm{cm}^2$ samples along the $< 1\bar{1}00 >$ and $< 11\bar{2}0 >$ directions. (b) A typical AFM image of these samples. The chemical mechanical polishing (CMP) surface shows plenty of straight, deep scratches.

used for sample characterization in this thesis. The in-situ LEED/AES system is placed on top of the main chamber of the growth system. The ex-situ tools are available on campus such as the room temperature (RT) STM (in the room S03), the AFM (in Keck's lab), the SEM (in Georgia Tech's cleanroom).

2.1 Sample Preparation

All of the samples studied in this thesis are semi-insulator $4H$-SiC or conductive $6H$-SiC wafers which were purchased from Cree Inc. The samples are commonly on-axis facets with two faces: silicon-terminated face $SiC(0001)$, and carbon-terminated face $SiC(000\bar{1})$. Due to fabrication limitations, each surface possesses a small miscut angle ($\sim 0.25°$) with respect to the perfect $SiC(000 \pm 1)$ surfaces. The original wafers (about 50 mm or 75 mm) were diced into 3.5×4.5 nm samples using the wafer cutting tools in the cleanroom at Georgia Tech. The two edges of the samples were along $< 1\bar{1}00 >$ and $< 11\bar{2}0 >$ directions (Fig. 2.1a).

The SiC wafers are usually mechanical polishing on one side and chemical mechanical polishing (CMP) on the other side. Figure 2.1b reveals a typical CMP surface

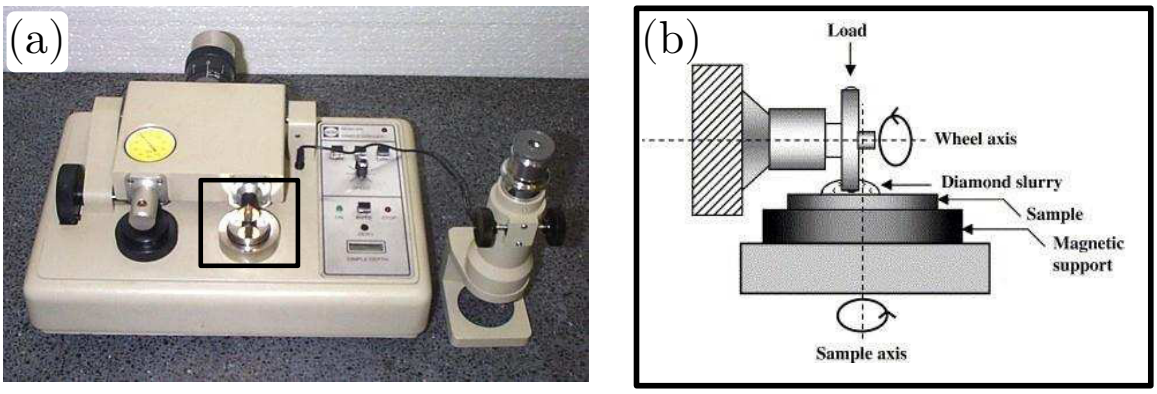

Figure 2.2: (a) Gatan 656 Dimple Grinder at Institute of Paper Science and Technology. (b) The dimple grinder operation: both the spherically-shaped grinding/polishing wheel and sample table rotate simultaneously in a perpendicular direction. If the wheel is aligned with the sample axis of rotation, the spherical dimple is formed on the substrate. However, in this figure an aspherical surface dimple is created because of the off-axis alignment.

using the AFM. As measured from this picture, the surface has the root mean square (RMS) roughness about 0.92 nm. There are plenty of randomly oriented, straight scratches as deep as 10 nm. Thus, the starting surface is not clean enough for the epitaxial growth of an ultra-thin film. The hydrogen etching method, which is well-known for preparing atomically flat SiC surface [84], is also employed in our lab for achieving high-quality silicon/graphene films.

2.1.1 Dimple Grinding

To study the mechanisms and properties of the epitaxial graphene growth on various vicinal angles, we prepare a curved surface from a flat, on-axis SiC sample in our lab. As it is known, silicon carbide is very hard material (silicon carbide hardness is $9-9.5$, on the Mohs scale, slightly less than 10 for diamond) which make it extremely difficult to change its shape. Fortunately, a dimple grinder is a suitable tool to erode the SiC crystal slowly using stainless steel wheels. By utilizing this technique, a concave-shaped dimple was prepared in the middle of a SiC sample which fits perfectly to our experimental purposes.

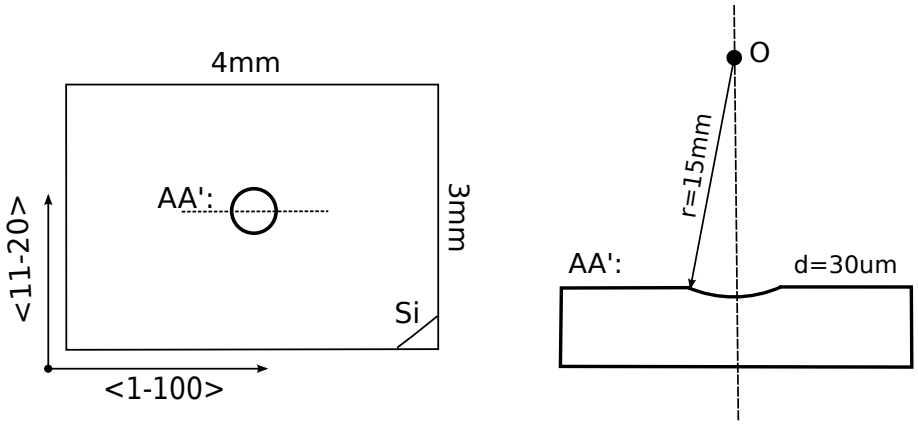

Figure 2.3: Sketching of the dimple. A concave-shaped dimple has been grinded in the middle of a SiC sample with the depth of about 30 μm.

The dimple grinding process was performed at Institute of Paper Science and Technology. The main equipment includes a Gatan 656 dimple grinder, 15 mm stainless steel Gatan grinding wheels, $1-3\,\mu$m grain-size diamond compound, and $0.05\,\mu$m grain-size aluminum suspension. At first, the sample was mounted to a stainless stain plate (a sample holder) via a strong wax which was melted at high temperature ($\sim 120\,^{\circ}$C). Tweezers were used to gently inserted the sample holder into the center of the table wheel which had magnetic support to hold it on top firmly. The SiC sample was coated with the paste (diamond compound or alumina suspension) diluted with water. The principle of the dimple grinder operation is showed in the Fig. 2.2b. While being operated, both the table wheel and the grinding wheel were rotating simultaneously and perpendicularly to create a concave, spherical dimple. However, if the wheel were not aligned with the sample axis of rotation, an aspherical surface dimple would be formed on the substrate as shown in this figure. Thus, to prevent multiple dimples or aspherical shapes from creating, it is important to maintain the alignment of the grinding wheel and the rotation axis of the sample throughout the entire grinding/polishing operations. The whole process took roughly three hours in which two hours for grinding using $1-3\,\mu$m grain-size diamond compound and another hour for polishing using $0.05\,\mu$m grain-size alumina suspension. In the end,

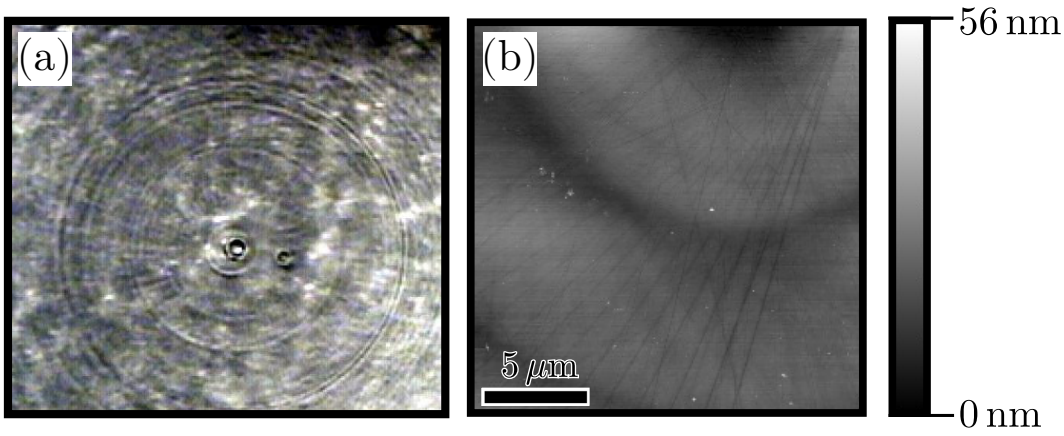

Figure 2.4: A SiC dimple surface after rapidly polished with 0.25 μn diamond compound for 30 mins. (a) Bright-field optical microscopy image. The field of view of the optical microscopy image is approximately 0.5 mm. The circles, sharing the same center, indicate a well-defined spherical dimple. (b) AFM image which shows the straight, deep scratches on the surface after polishing.

we used an optical microscope to check the desirable smooth and depth of the dimple.

After grinding, a concave-shaped dimple was constructed in the middle of a SiC sample with a variety of vicinal angles. The dimple was a part of the 15 mm diameter sphere. The depth of dimple ($\sim 30\,\mu$m) was achieved by monitoring a depth gauge of the grinder. The depth gauge was able to measure the vertical distance with an accuracy of $\pm 1\,\mu$m. Because each SiC bilayer height is approximate 2.5 Å, the dimple included about 150.000 bilayers. As sketched in the Fig. 2.3, the out-of-plane polar angle θ varies from $0^\circ < \theta < 5^\circ$. It means the miscut angles have changed continuously from 0° to 5° with respect to the basal plane $SiC(0001)$.

Figure 2.4 reveals the morphology of a dimple surface after being rapidly polished with 0.25 μn diamond compound for 30 mins. The bright-field optical microscopy image shows a series of circles (rings) which share the same center. It confirms that the dimple has a perfect spherical shape. The AFM image displays plenty of the random straight scratches on dimple surface. The RMS surface roughness is over $400\,\mu\text{m}^2$ which is comparable to the initial surface roughness (~ 0.92 nm) of the mechanically polished SiC as received from the manufacturer (see Fig. 2.1).

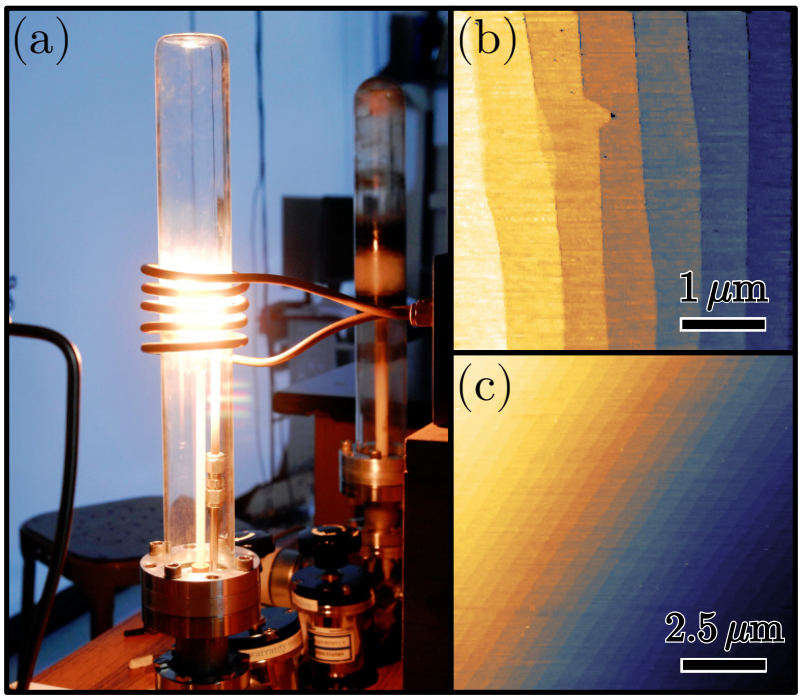

Figure 2.5: (a) the custom tantalum thin-wall hydrogen etching furnace in Keck's lab. AFM images of a typical 6H-SiC(0001) after hydrogen etching show regular steps of (b) single unit-cell or (c) half unit-cell depending upon the etching recipe and initial surface conditions [86].

2.1.2 Hydrogen Etching

As it was pointed out in the previous sections, silicon carbide surfaces, after being polished via chemical mechanical methods, are still rough with many straight scratches and marks (see Fig. 2.1 and 2.4). Therefore, hydrogen etching treatment is the method of choice to obtain the atomically flat surfaces [84]. After hydrogen etching, both the Si-face and the C-face of 4H- and 6H-SiC are smooth with flat terraces and regular steps of a half or full unit-cell height. Surface morphology of the particular SiC wafers strongly depends on the etching conditions, gas components, SiC polytypes (4H or 6H type), face polarities (C- or Si- face), on-axis or off-axis angles of SiC surfaces. For example, experimental results observe full unit-cell high steps on the 6H-SiC(0001) surface and half unit-cell high steps on the 6H-SiC(000$\bar{1}$) surface [85].

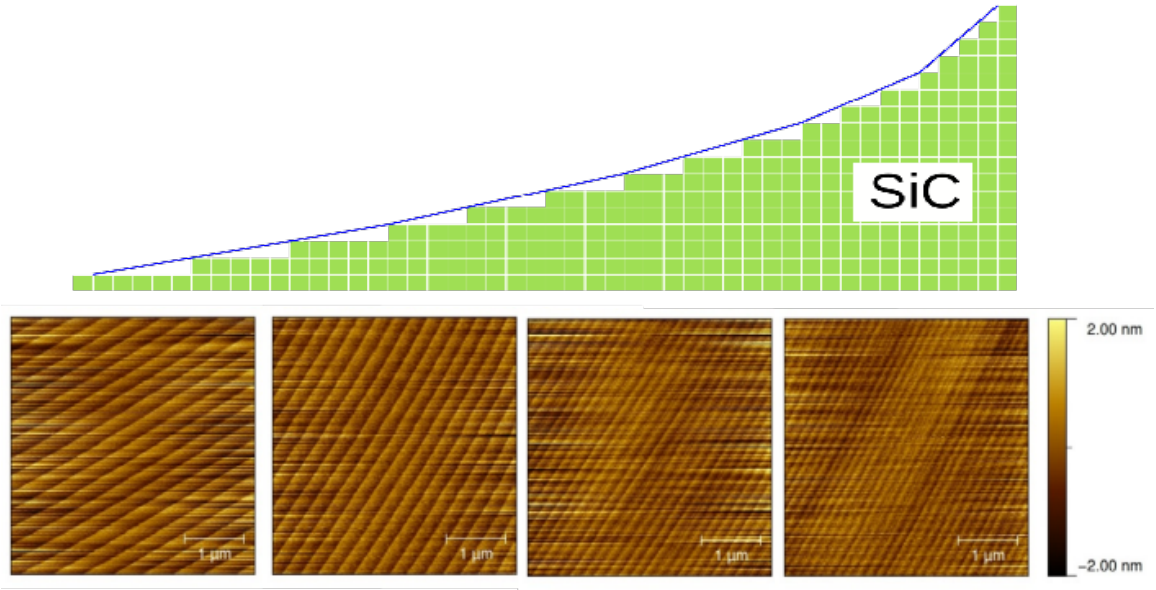

Figure 2.6: AFM images of the $6H$-SiC dimple at different locations inside it after hydrogen etching treatment. It clearly indicates that the dimple surface is atomically flat consisting of regular, straight steps. It also shows the step density depending on the local angles which increases from the left to the right of the bottom panel.

Our samples were etched by the home-made hydrogen etching system in Keck's lab. Figure 2.5 pictured the etching furnace which was normally operated in a temperature range of $1400-1650^\circ$ C with a H_2/Ar mixed gas flowing under one atmospheric temperature. The temperature was gradually increasing at the rate of $50-100^\circ$ C per minute to the final etching temperature, stayed for awhile $15-60$ minutes. Then it was ramped down to 800° C at the rate of 100° C per minute, and finally cooled down to the room temperature. During the etching process, the mixed gas, 5% hydrogen and 95% argon supplied by South Airgas company, flowed at the rate of 200 sccm to remove silicon droplets and residual chemical byproducts. The whole system was connected to a computer for convenient controlling through a Labview interface. More details about this system were presented in the thesis of Dr. Xuebin Li [76].

Figure 2.6 shows the series of AFM images at different positions inside the $6H$-SiC dimple after hydrogen etching. The etching procedures were to anneal the sample at 1500° C for one hour to completely remove all of the scratches that appeared in the

grinding process. The hydrogen treatment was successful in producing an atomically flat surface with equidistant, straight steps. The steps are full unit-cell height or half unit-cell height depending on the local positions (the more details of the analysis are found in the section 4.1). From the left to the right of the bottom panel, the AFM images were taken from the center to the edge of the dimple. There is an agreement between the step densities and the local angles: the greater the local angle is, the higher the step density becomes. The morphology of the dimple after hydrogen etching was consistent with the previous studies [87–89].

2.2 Growth System

2.2.1 Design and Operation

The home-made growth system was originally designed by Dr. David Lee Miller, and more details were presented in his thesis [90]. Fig 2.7 shows the schematic diagram of the system which performs both rapid ultra-high vacuum (UHV) characterization and growth. The whole system is maintained at UHV environment($\sim 10^{-10}$ Torr) thanks to an ion pump (IP) and a titanium sublimation pump (TSP) which are located at the bottom of the main chamber. The RVL2000 LEED/AES device from LK Technologies, installed at the top of the main chamber, is able to characterize samples right after growth without any possibility of contaminations. On the right of the main chamber is a double load-lock which is designed for quickly transferring samples from atmospheric pressure to the UHV system (about an hour). The sample holder is grasped by a claw which can be moved across the whole system. On the left of the main system is the growth chamber where the samples are grown in different conditions. The growth chamber is isolated from the main chamber by a gate valve and connected to a gas-line system which is supplied hydrogen, argon, and silane. Inside the growth chamber, the graphite furnace is annealed by a radio frequency (FR) induction furnace.

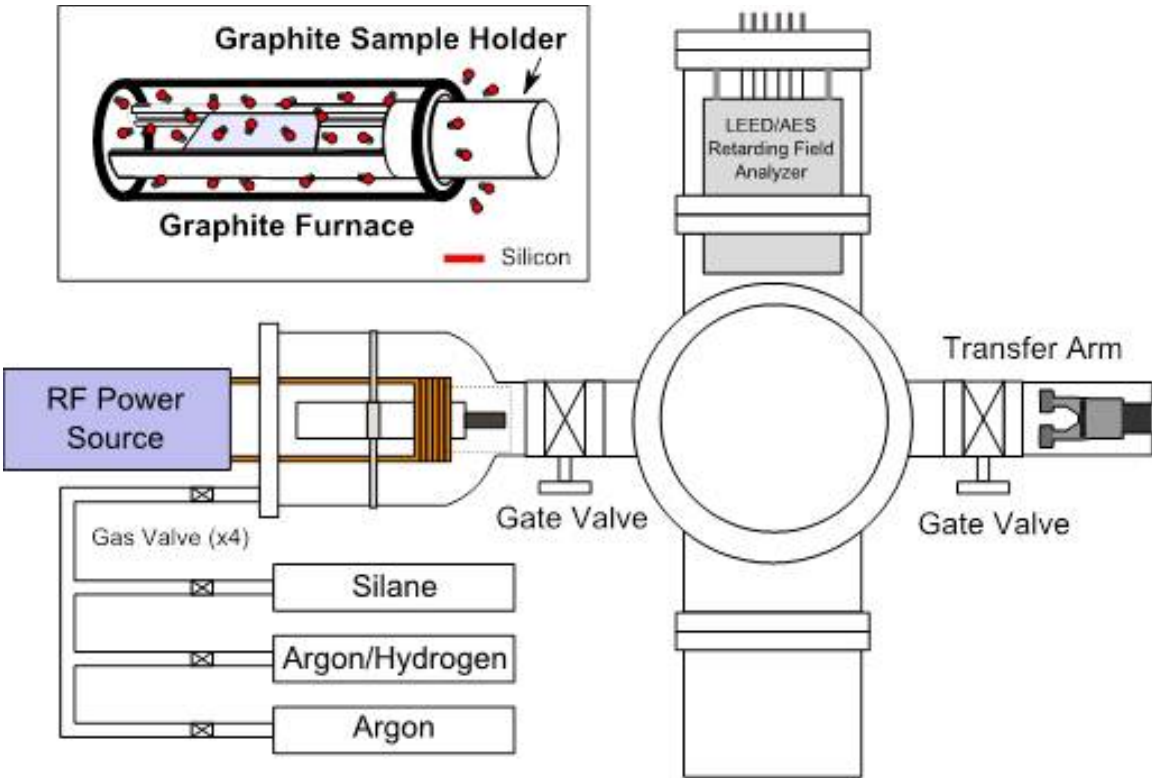

Figure 2.7: Sketch of the home-made growth system. The system includes (from left to right) the growth chamber, gas-line connections, and in-situ LEED/AES characterization equipment, and transfer arm. The inset is a zoom-in of the graphite sample holder which is inserted from the front of the graphtie furnace (see the text for more details).

Both the growth furnace and sample holder are made of graphite which has proven to be the most compatible material for growing silicon carbide. Firstly, graphite has an extremely high melting point so that it can survive in high-temperature conditions for hours (up to 1600° C). Secondly, it has a low heat capacity which is enabled to rapid thermal processing. The graphite furnace is easy to be annealed to target temperature 1500° C in a minute. Moreover, graphite is relatively inert at high temperature (except in the present of oxygen or hydrogen) which can avoid sample contamination and interaction. However, carbon has high spectral emissivity which results in rapidly lost power through radiation. As a solution to this issue, an alumina (Al_2O_3) tube is used to cover the graphite furnace for radiation shielding.

A graphite sample holder are customized to hold up to three 3.5×4.5 nm SiC samples (inset of Fig 2.7). The holder has two arms with slots inside to slide the samples into it. At the end of each arm, there is a stopper to prevent the samples from falling out. The size of these slots is close to the thickness of the SiC wafers to keep them stable. A plug, where the two arms are attached, well fits the graphite furnace. Thus, while the holder is inserted into the furnace, the samples are virtually enclosed by carbon walls. To change the leak rate of the enclosed furnace, we drill a small hole through the plug. By using the "hole" holder, it is possible to perform silicon deposition or graphene graphitization in different conditions. Moreover, the design of the sample holder allows us to study growth processes on both faces of the samples simultaneously.

The growth furnace is equipped with the gas-line system which can supply various gasses through an ultra-high precision valve (leak valve). This leak valve is cable of controlling the leak rates as low as 1×10^{-10} Torr.L/s by slowly rotating a nob. The gas-line system is formed using 1/4 in stainless steel tubes joined with Swagelok valves (as seen the Fig 2.8). There are three lines which are directly connected to three different gas cylinders: ultra-high purity argon, 5.0 % hydrogen/argon, and 0.7 % silane/argon. Each line has two Swagelok valves to reduce gas pressure and accurately estimate the leak rates. The gas-line system is connected to a turbo pump via a high vacuum VCR valve. The gas-line system is leak-checked using helium gas and quadrupole mass spectrometer. As the results, the pressure as low as $10^{-}7$ Torr could be achieved inside the gas-line system before filling with gasses. By closing or opening the leak valve, growth experiments can be performed in static (no gas flowing) or dynamic (gas flowing) conditions.

In this section, I will present the typical routine of growth experiments. A 3.5×4.5 mm sample was selected from a SiC wafer or prepared by dimple grinding. It was cleaned ultrasonically with acetone and ethanol for 10 mins respectively. Then, it was

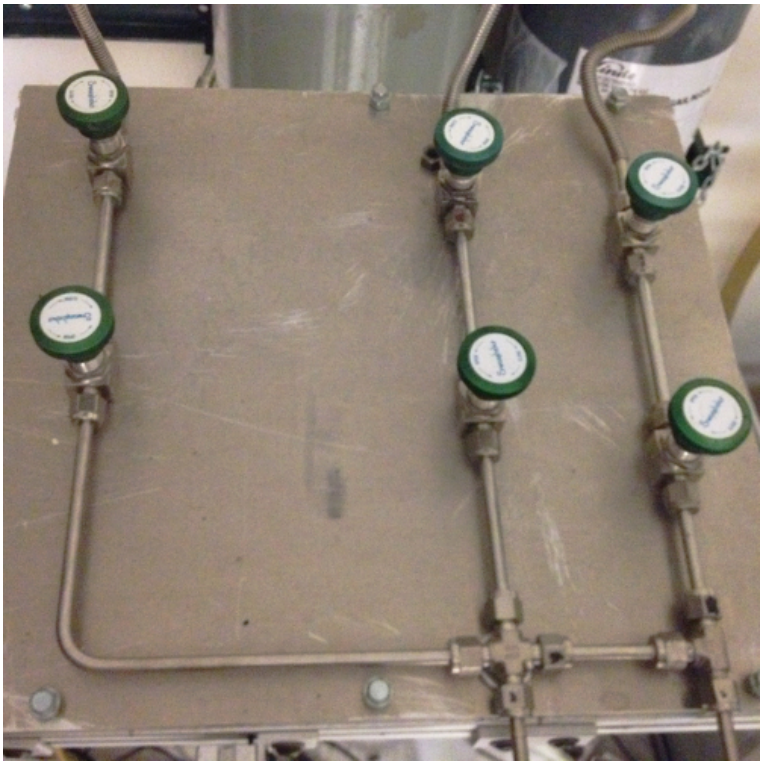

Figure 2.8: Gasline system. Three lines connect to three different gas cylinders (on the back, not shown) and each line has two Swagelok valves. Two lines in front, one is connected to a turbo pump and one is hooked up to the growth chamber via a leak valve.

blown out with nitrogen to be dry and remove dust on the surface. For achieving atomically flat surface, it was put into the tantalum thin-wall furnace to perform hydrogen etching. The results of this process were verified by using AFM which was operated in the air for quick scans. After that, the sample was carefully inserted into the graphite sample holder, which was with or without a hole on the plug depending on the purposes of the experiments. The holder was then placed on top of the elevator which was located inside the double load-lock. The double load-lock design allowed to transfer the sample from the air to the vacuum system in a short time (an hour) [90].

In the meantime, the gas-line system and the graphite furnace must be cleaned before each growth experiment in order to minimize contaminants. All of the Swagelok valves were opened to clean the whole gas-line system. Then, the cylinder valve was

slowly opened to purge the entire gas-line for about 5 mins to get rid of the air inside the tube as much as possible. After that, the gas-line was pumped down for one hour by using a turbo pump. In addition, it was necessary to anneal the graphite furnace up to 1500° C for half of an hour to remove possible elements left from previous experiments.

After an hour of pumping, the sample holder was transferred into the UHV chamber and inserted into the furnace to be ready for the growth process. The gate valve was closed to separate the growth chamber from the UHV main chamber. Then, the leak valve was opened slowly to leak the gas from the gas-line into the growth chamber. The gas pressure in the chamber was measured using a typical Bayard-Alpert ion gauge at pressures less than 1×10^{-4} Torr and a Convectron gauge at higher pressures [91]. For safety, the gas pressure inside the chamber was kept below 600 Torr because it would remain less than atmospheric pressure during the growth. Then an infrared pyrometer was installed to monitor the furnace temperature (see section 2.2.2 for more details). The growth process was controlled by using an in-house software called pyTherm which was written in Python (see Dr. Miller's thesis for more information [90]). The procedure for a typical growth experiment was to maintain the furnace temperature at 850° C for 20 mins, 1200° C for 20 mins, and final growth temperature for a given amount of time, then natural cooling down to room temperature. The first step, maintaining the furnace temperature at 850° C, was to outgas the samples and remove unwanted particles on the surface. The next step, maintaining the furnace temperature at 1200° C for 20 mins, would allow the initial SiC step-flow to stabilize across the surface [92]. In the final step, the growth temperature was constantly kept for a period before cooling down. Once the temperature of the furnace decreased below 600° C, the valve connected to the turbopump was opened. Then the furnace chamber was pumped down to 1×10^{-7} Torr before opening the gate valve to the main chamber.

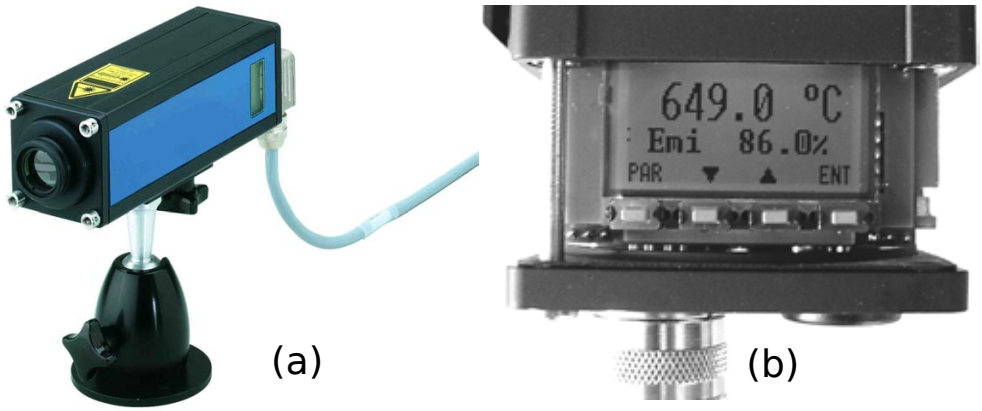

Figure 2.9: The Mikron MI-GA140 Infrared Pyrometer (IP). (a) Overview of the IP with the adjustable lens in the front and the analog output cable in the back. (b) The zoom in of the built-in display with indication of temperature and emissivity.

2.2.2 Temperature Measurement

It is a huge challenge to measure and monitor the temperature inside the graphite furnace. One of the methods I attempted was to use a type C (W-5% Re/W -26% Re) thermocouple (TC). A cut was made on the alumina (Al_2O_3) covered tube, and then a hole was drilled through the graphite rod close to the furnace. A thermocouple junction has adhered at the middle of this rod. Unfortunately, this method was not well performed because of two following issues. The first problem was the effect of the huge electrical noise. The placement of the TC junction was placed inside of the furnace coils. While turned on, the induction RF furnace generated strong magnetic fields, thus introducing the huge electrical signs to the TC. Although two TC wires were kept parallel and close to each other to minimize the induced current, the noise was still significant. A low-pass filter was used in an attempt to reduce the noise; however, the results were not reliable because the TC signals were on the order of 20 mV while the pickup signals from the coils were on the order of 10 V. Another problem was that the TC junction was extremely easy to break after several growth cycles. In addition, it was time-consuming to replace the broken one because of opening the whole UHV system.

In practice, a Mikon MI-GA140 infrared pyrometer (IP) was used to measure furnace temperatures (Fig 2.9). The IP has a measurable temperature range of $300 - 3300^{\circ}$ C, which is appropriate for our growth conditions. With the IP, the temperature was read and transferred to the computer fast and easily using the analog output cable. Another advantage of using the IP was the ability to measure the furnace temperature from a distance through the UHV window. The temperature was relatively insensitive to the radio frequencies generated by RF heater. Nonetheless, it was difficult to choose appropriate emissivities for each measurement. As the emissivity of a surface representing its effectiveness in emitting energy as thermal radiation, the emissivity value depends on the material, surface grade, temperature range, etc. The typical values of graphite emissivity is about $80 - 85\%$ between temperature of $1000 - 1500^{\circ}$ C [93]. However, what is the exact value? To solve this problem, the following experiment was performed to measure the emissivity of the graphite furnace surface.

The purpose of this experiment was to calibrate the "effective" emissivity depending on the furnace temperature. When chosen the "effective" emissivity, the temperature measured on the furnace surface ("surface temperature") should give the exact temperature inside the furnace ("inside temperature" or real furnace temperature). It is worth to notice that the "effective" emissivity is not the actual emissivity of graphite surface. However, it took into account both the graphite emissivity and the temperature difference between the surface and inside of the furnace. To measure the "inside temperature", I used the vented sample holder which had a small hole through the plug (its diameter around 0.06 inch). The distance from the hole to the IP was about 15 inch, which was corresponding to the spot size diameter of 0.4 inch (Page 5 of the manual document). The diameter of the spot size was smaller than that of the hole, thus enable to measure the "inside temperature" by directly pointed through this hole. The furnace was enclosed so that the emissivity was set at 99%

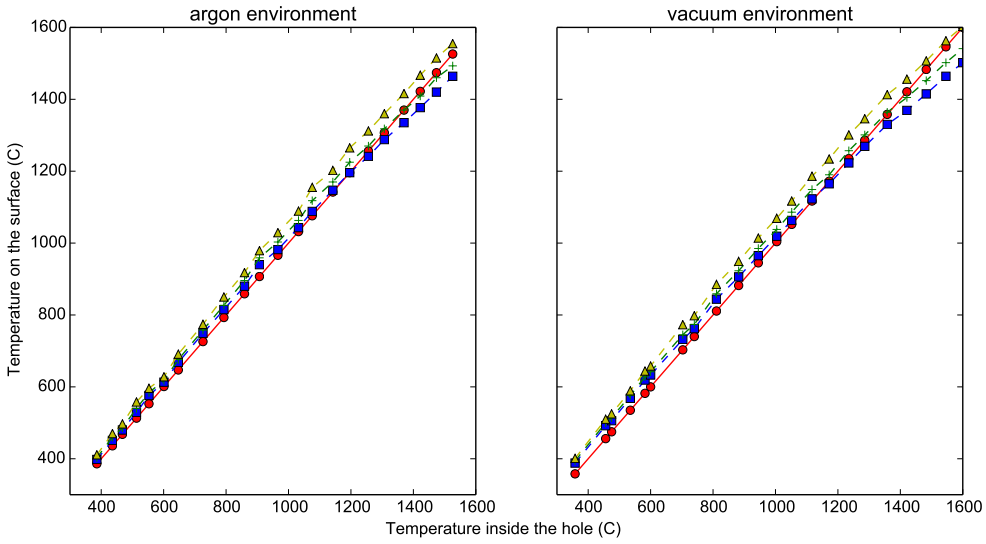

Figure 2.10: Temperature on the surface using various emissivity setting in the infrared pyrometer: $\epsilon = 99\%$ (blue square), $\epsilon = 85\%$ (green cross), $\epsilon = 75\%$ (yellow triangle). The red circles are the temperature inside the hole itself. The experiments were performed in argon (on the left) and vacuum (on the right) environments.

as a result from the black-body approximation. When pointed the IP through this hole, its position was adjusted and focused on maximizing the reading. Thus, the value read on the IP screen was truly the real "inside temperature". Then, the IP was pointed on the graphite furnace to measure the "surface temperature". Two different experiments were performed separately while heating the furnace from room temperate to 1600° C: (1) recording the "surface temperature" of the various emissivity of $99\%, 85\%, 75\%$, and (2) recording the adjustable emissivity of the IP when the "surface temperature" was equal to the "inside temperature".

In the first experiment, the graphite furnace was heated step-by-step from 400° C to 1600° C. At each step, the furnace temperature remained constant by using the PID loop. Then, the IP was used to measure the "inside temperature" by pointing it through the hole (using the technique discussed above). The "surface temperature" was recorded with different emissivity of $99\%, 85\%, 75\%$. The experiments had done in both argon environment (~ 600 Torr) and UHV environment ($\sim 10^{-8}$ Torr). The

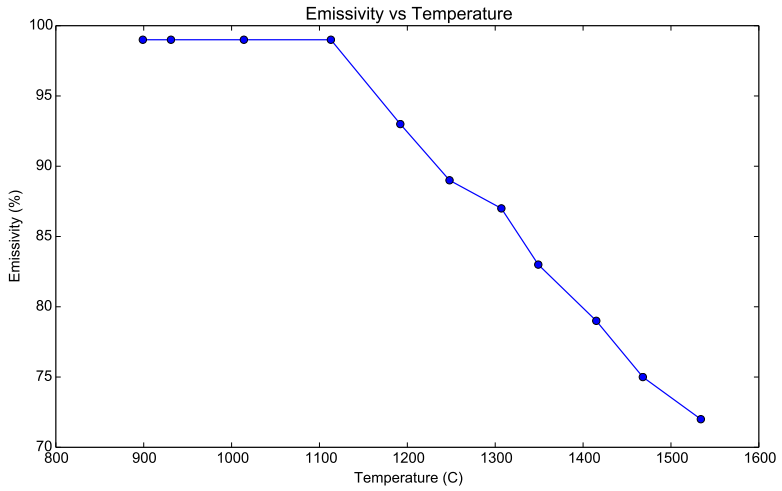

Figure 2.11: The "effective" emissivity depends on the target temperature. The "effective" emissivity is the value inserted in the IP so that measuring the temperature on the furnace surface should give the exact temperature inside the furnace.

results are plotted in the Fig. 2.10. As shown in that figure, there are similar features from both argon and vacuum environments. The smaller the emissivity was set, the higher the temperature was read by the IP. At low-temperature range (below 1600° C, "surface temperature" is slightly higher than the "inside temperature" regardless of emissivities. At the graphitization temperature range, $1300 - 1400°$ C, the emissivity is about $80\% - 85\%$. The error of the temperature measurement is estimated less than $\pm 10°$ C.

Figure 2.11 shows the results of the second experiment. This study was similar to the first one and was performed in the vacuum environment only. For each step in this experiment, after recording the "inside temperature", the IP emissivity was adjusted slowly (in steps of 0.1 %). The emissivity, when the "surface temperature" was equal to the "inside temperature", was written down. As it can be seen from the figure, the higher the temperature is, the lower the emissivity becomes. It means at higher temperature regime, the "surface temperature" was significantly lower than the "inside temperature". There were two plausible reasons to explain this phenomenon. Firstly, the end of the furnace, where the sample holder was inserted, was not covered

by alumina Al_2O_3 shielding. As the results, graphite furnace lost its power through radiation because of the high spectral emissivity of carbon. Secondly, the end of the furnace received less energy because of the weaker magnetic fields generated by the coils.

In conclusion, the Fig. 2.11 is the guideline for setting up the IP emissivity depending on different temperature. The results are relatively insensitive to the environment. The error of the temperature measurement is less than $\pm 10^\circ$ C with an appropriately chosen emissivity.

2.3 Sample Characterization Tools

2.3.1 Low Energy Electrol Diffraction (LEED)

The first electron diffraction was confirmed experimentally in 1927 by Davisson and Germer [94]. Since the early 1960s, LEED has become one of the most successful surface science tools to determine the surface crystal structure within a few atomic layer. This technique is extremely surface-sensitive because of using a well-defined low energy electron beam ($20\,\text{eV} - 200\,\text{eV}$) emitted to the surface. The de Broglie wavelength of a massive particle is $\lambda = \frac{h}{mv}$, so a typical $100\,\text{eV}$ electron has the wavelength of $\lambda_e = 1.22\,\text{Å}$. According to the attenuation model $I = I_0 e^{-d/\lambda_e}$, the electron beam only penetrates at most several nanometer in depth d. Thus, only electrons scattered from near surface can leave the surface, and collecting them on a phosphorous screen gives us the information of a few top layers on the surface.

The observed LEED pattern is the reciprocal lattice of the pseudo-$2D$ surface structure. When an incident beam arrives in a crystal surface, the scattering vector is defined as $\Delta\boldsymbol{k} = \boldsymbol{k}_0 - \boldsymbol{k}$, where $\boldsymbol{k}_0, \boldsymbol{k}_k$ represent, respectively, the wave vectors of the incident and reflected electrons. The Bragg condition for the diffraction pattern appeared is that the scattering vector must terminate on a reciprocal lattice, $\Delta\boldsymbol{k} = \boldsymbol{G} = h\boldsymbol{a}^* + k\boldsymbol{b}^*$. Fig. 2.12 shows the Ewald's sphere construction for the case of

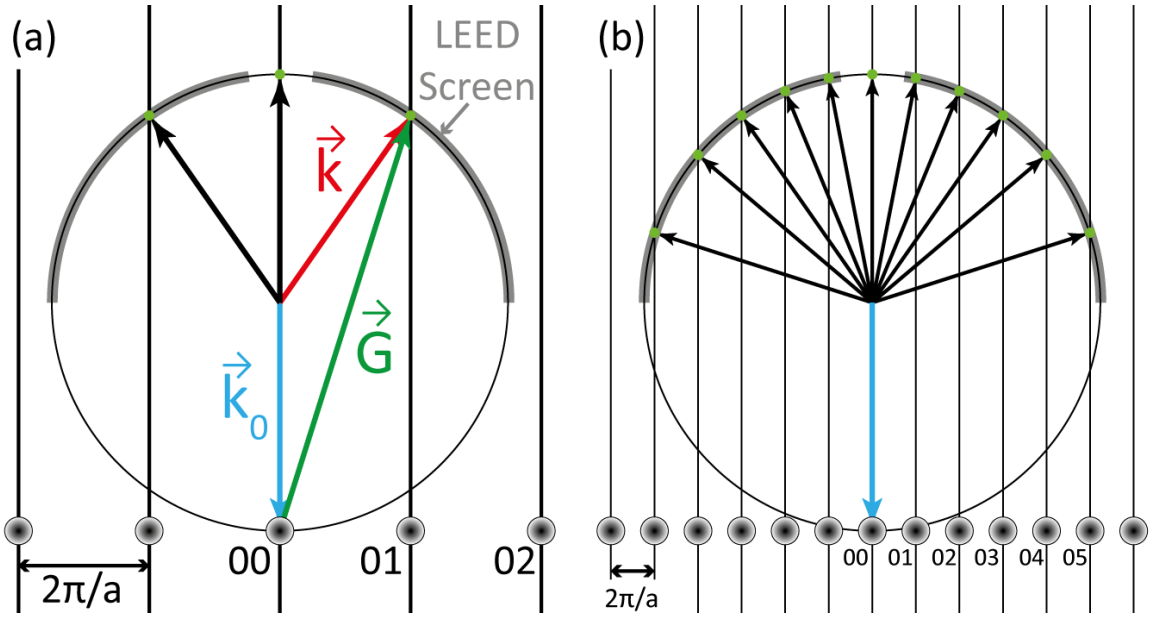

Figure 2.12: The Ewald sphere construction for the normal incidence case: The sphere has a radius $|\boldsymbol{k}_0|$, the rods are numbered by their hk value in the reciprocal space, and the green spots represent the intersection of the rods with the phosphor screen. (a) Spots are then formed on the fluorescent screen at the intersections of the rods and the screen. (b) at higher kinetic energies, the Ewald sphere radius increases and more rods cross the sphere, thus more LEED spots are visible [95].

normal incidence of the primary electron beam which is suitable for our system. The intersections between the sphere and the reciprocal lattice are the LEED pattern observed on the fluorescent screen. The size of the Ewald's sphere and the number of diffraction spots are controlled by the incident electron energy. The higher the energy of the primary electron beam is, the more spots are visible on the screen. In practice, multiple scattering usually happens which result in the superposition of several reciprocal lattices into a LEED pattern.

Our LEED, which is incorporated in the growth system, is RVL2000 model purchased from LK technology (Fig. 2.13). The system includes 4 grids and a phosphor-coated screen. In the LEED mode, the two outer grids are held at the ground potential, and the voltage between two inner grids G_{23} filters the unwanted inelastically scattered electrons. At the middle, there is an electron gun which is made of a LaB_6

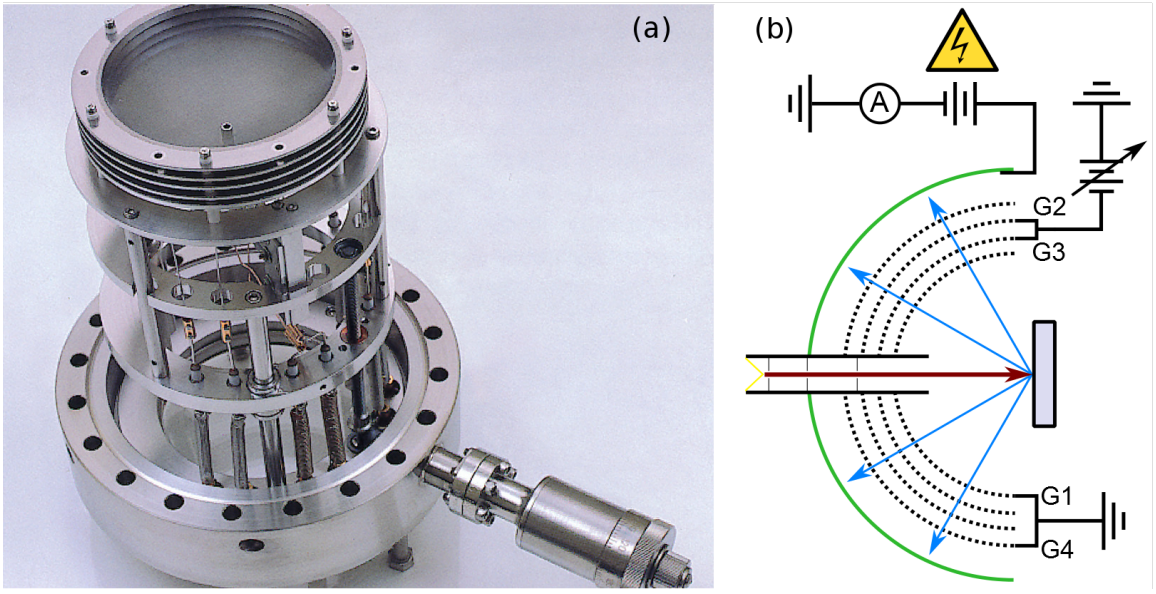

Figure 2.13: (a) An image of the LK RVL2000 LEED/Auger system. At the top are 4 grids and a phosphor-coated screen, in the center is the electron gun. (b) A schematic of the LEED/Auger. It is convenient to switch between LEED mode and Auger mode by changing the kinetic energy of the electron primary beam (E_{e^-}), the filer voltage (G_{23}), and screen voltage (V_s) (see text for more details).

(lanthanum hexaboride) filament. The filament operates at relatively low temperatures (filament currents of $\sim 1.6\,\mathrm{A}$) in order to get the required emission current ($\sim 1\,\mathrm{mA}$). It is important to adjust the filament slowly and never exceed $1.8\,\mathrm{A}$ to protect the filament to last longer. Moreover, for safety, the system must be operated in UHV environment, below $10^{-8}\,\mathrm{Torr}$. The typical parameters for the LEED mode are: $E_{e^-} = 20 - 200\,\mathrm{eV}$, $V_s = 3.5 - 5.0\,\mathrm{kV}$, $G_{23} = -V_{e^-} + \Delta V$. The diffraction patterns are taken by a Canon camera in a low light mode using the open-source camera acquisition software package gPhoto2.

The Fig. 2.14 shows typical LEED patterns of epitaxial graphene growth on the C- and Si-faces of a SiC wafer. The distinguishable characteristics of the two patterns are a graphene ring on the C-face and a $6\sqrt{3}\times 6\sqrt{3}R30^\circ$ reconstruction on the Si-face.

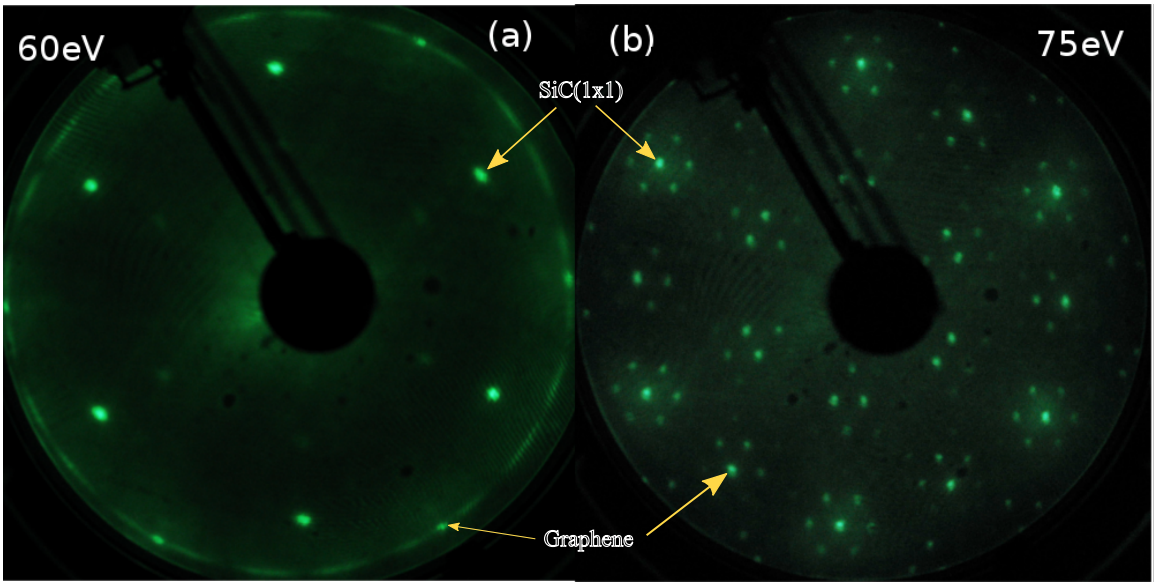

Figure 2.14: Typical LEED patterns of the EG growth on SiC: (a) C-face at 60 eV. The well-known feature of the pattern is a graphene ring which reflects the rotational disorder. (b) Si-face at 75 eV. The special characteristic of the pattern is the six-root-three reconstructions.

2.3.2 Auger Electron Spectroscopy (AES)

AES technique was developed in the 1960s based on the Auger effect which was discovered independently by both Lise Meitner and Pierre Victor Auger in 1920s [96]. AES provide us valuable information on the chemical compositions of the surface. Moreover, by calculating the relative strength of different signals, we may quantitatively estimate the thin film thickness. For example, for a SiC substrate the $Si : C$ ratio will provide the information of the C- or Si- rich surface and the thickness of silicon or graphene thin films. Similar to LEED, AES is a surface-sensitive technique within a shallow depth of electron penetration (several nanometers). In contrast to LEED where elastic scattering electrons have been collected, the inelastic scattering electrons with lower energies are gathered in AES mode.

The Auger process happens in two sequentially stages (Fig. 2.15). The first stage is to create core holes when an external electron with sufficient energy (a few keV) collides a surface atom. After the collision, the low-energy core-shell electron ($1s$)

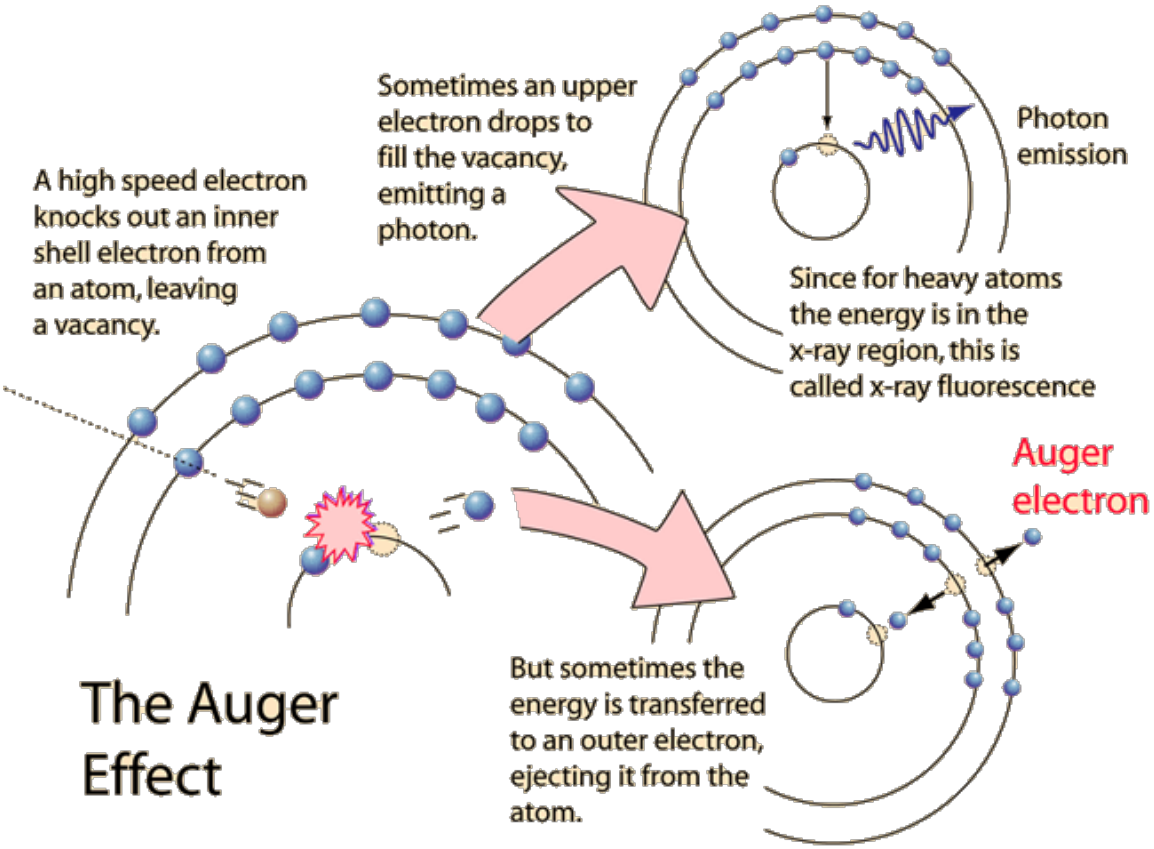

Figure 2.15: A schematic diagram of the Auger effect. The results of the process release either a X-ray photon with its energy $h\upsilon = E_A - E_B$ (top) or an Auger electron with its kinetics $K_E \approx E_A - E_B - E_C - \phi$ (bottom) [97].

is removed, which create a vacancy. In the next stage, the core hole (the vacancy) eventually decay because of the relaxation from a high-energy level to a low-energy level. The energy is released via either photoemission (X-ray) or electron erection (called Auger electron). The former case likely happens for heavy elements which have a deep core hole with high binding energies (BE). The latter case is called Auger process which has a higher probability for light elements (almost exclusively for $Z < 15$). In the Auger process, the internal rearrangement of electrons is radiationless, and the final atomic state has two holes (doubly-ionized). Thus, the Auger transition notation is KLL, $KL_1L_{2,3}$, etc, or XYZ in general where the first letter is the initial core hole location, the second letter is the initial location of the relaxing electron, and

the third letter is the location of the second hole (the initial location of the Auger electron).

Our in-situ AES is one of two modes in the LK RVL2000 system which uses a retarding field analyzer (RFA). In RFA mode, the inner and outer electrodes (grids) are held at ground potential, while applying a retarding, negative voltage V to the two middle grids, G_{23}, to make it as a high pass filter. Thus only electrons with energies above the pass energy V can reach the phosphor collector, and produce a measurable current I. The Auger electronics use a lock-in amplifier to measure the differential signal: $N(E) = -\frac{dI}{dE}$, which is called Auger intensity. Analyzing the Auger intensity $N(E)$ provides us the characteristic of the surface atom because each element has its unique orbital electron energy levels. The typical parameters for the Auger mode are: $E_{e^-} = 2.5\,\mathrm{keV}$, $V_s = 0.5\,\mathrm{kV}$, $G_{23} = -0.5\,\mathrm{kV}$ (see Fig. 2.13).

Despite its convenience (incorporated with LEED) and high analyzer transmission, the RFA suffers from a poor energy resolution and a poor signal-to-noise ratio relative to the CMA [98]. The poor signal-to-noise results from a large, integrated background signal of secondary and backscattered primary beam electrons. The energy resolution of the RFA design is ΔE which is mostly bigger than that of CMA system, $\Delta E/E$. In this thesis, I will compare the experimental results of the RFA and CMA (available in our Room Temperature STM system) and provide a routine to convert between them at convenient in Sec. 3.1.7.

In the section 3.1, the AES model is built to determine the thin film thickness based on Auger electron intensities of silicon and carbon. Unfortunately, due to the large beam size ($\sim 0.5\,\mathrm{mm}$) it is impossible to characterize local GNRs, but it serves as an estimation of the average graphene thickness.

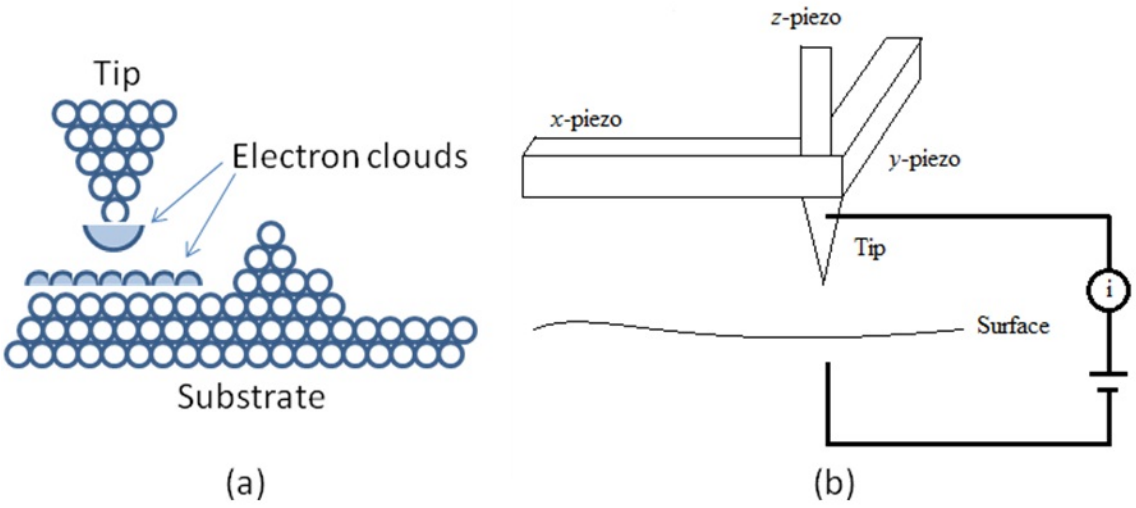

Figure 2.16: Schematic diagram of the principles of STM: (a) The interactions between tip and surface. The tunneled electrons are primarily from the atomic apex of the tip to the surface due to the quantum mechanics. (b) The tunneling current generated from tip and surface is used as a feedback to control the tip movement [99].

2.3.3 Scanning Tunneling Microscopy (STM)

STM, invented in 1981 by Gerd Binnig & Heinrich Rohrer at IBM Research-Zurich, is the perfect tool to explore surface materials at the atomic scale [100]. By placing a metallic atomically sharp probe close ($\sim 10\,\text{Å}$) to the conductive samples, a current I is tunneled through the small vacuum gap. In quantum mechanics, the tunneling current is exponentially proportional to the vacuum gap z thus make it relatively sensitive to the surface morphology. Moreover, switching the sign of the bias voltage would alter the electronic surface states: an empty state or a filled state corresponding to the positive or negative voltages respectively. In practice, there are two modes of STM operation, constant height or constant current. In the former mode, the relative height of the tip to the sample remains constant during scanning, then the variations of the tunneling current provide the surface structure of the sample. The mode allows faster scan because the feedback loop is opened (or set with a very slow response time). The latter mode is commonly used in the STM system in which the feedback loop remain the pre-set tunneling current unchanged during scanning. In this case, the

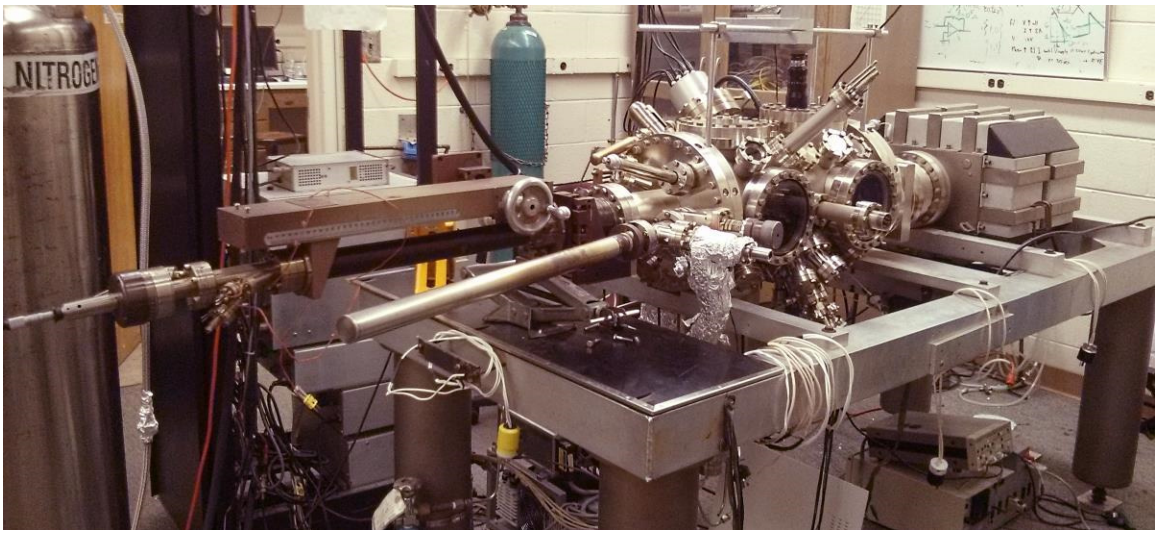

Figure 2.17: Room Temperature (RT) STM system in S03 lab. The chamber includes capabilities for scanning tunneling microscopy (STM), low-energy electron diffraction (LEED), CMA Auger electron spectroscopy (AES), ion beam sputtering, residual gas analysis, and a load-lock for tip/sample exchange.

tip-height variations will tell us the surface configuration, even in atomic resolution (Fig. 2.16).

The theory of STM has been studied rigorously [101, 102]. The tip-sample tunneling current using the first-order perturbation theory has the form

$$I = \pm\frac{2\pi e}{\hbar}\int_{E_F}^{E_F+V_b}\rho_t(\epsilon)T(\epsilon)\rho_s(\epsilon)d\epsilon \tag{2.1}$$

in which E_F is the Fermi energy, V_b is the applied voltage bias, ρ_t, ρ_s are the density of states in the tip and sample respectively, and $T(\epsilon)$ is the tunneling matrix describing all possible scattering probabilities between electron wave functions in the tip and the sample. In the STM, the tip is extremely sharp, so its density of state ρ_t is relatively flat. Moreover, the tunneling matrix is approximately unchanged in the constant current mode because of high sample work function. Thus, the tunneling current is just proportional to the integral of the local density of states (LDOS) of the sample under the tip.

Fig. 2.17 is an image of our home-made Room Temperature STM (RT STM) system. The more details of the ultra-high vacuum (UHV) environment, piezoelectric

design, transferring process, and tip + sample preparation are presented in the thesis of our former Ph.D. students [49, 86, 103].

2.3.4 Atomic Force Microscopy (AFM)

AFM, invented shortly after the STM in 1986 [104], is widely used as a standard surface tool. The advantages of this tool are quick, reliable, and versatile thank to its ability to operate in atmospheric conditions and non-conductive samples. As the name suggested, it measures a short-range atomic force between the tip apex and the sample surface when approaching a sharp tip sufficiently close to the surface. The tip-surface interaction includes van de Walls, electrostatic, ionic, frictional, or chemical, etc. The force is converted to an electronic signal with the aid of the optical detection of the movement of the cantilever holding the tip.

The AFM can operate in different modes depending on various tip-surface working distance (Fig. 2.18): contact mode, non-contact mode, and tapping mode. In the contact mode, the tip physically touches the surface and merely dragged across the surface whiled scanned. As the results, the tip and surface are both damaged while scanned, thus making this mode uncommonly used. In contract, a non-contact mode is more widely employed. In this mode, the tip is forced to oscillate perpendicular to the surface, in which its frequency and amplitude have the roles of tunneling current and tip-sample distance relatively in the STM measurement. Because of meniscus forces, the tip will regularly stick to a sample that generates glitches on AFM images. To overcome this difficulty, in the tapping mode the tip strikes and withdraws from the surface of the sample on each oscillation cycle by applying a large vibration amplitude.

The AFM we usually used is located in Keck's lab Fig. 2.18. The non-contact mode is mostly performed in this equipment to keep a tip long-lasting. In this mode, the average distance between the tip and the surface is $2 - 4\,\mathrm{A}$ which is within the

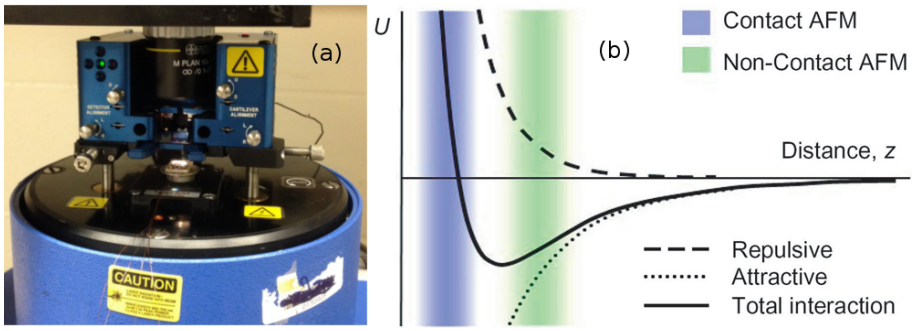

Figure 2.18: (a) AFM in Keck's lab. (b) Inter-atomic force vs. distance [105]. Depending on different tip-surface working distance, the AFM can operate in the contact or non-contact modes.

region of attractive forces. The main parameters using in this equipment are the frequency of oscillation (typically $f_0 = 300\,\text{kHz}$), the typical distance of approach ($-13\,\text{nm}$), and the amplitude of oscillation (20 nm). The ultimate resolution of the AFM topography is generally limited by the diameter at the end of the tip. For a standard topographic, tip diameters are around 10 nm [106]

2.3.5 Scanning Electron Microscope (SEM)

SEM, developed as early as the 1930's, uses a focused beam of high-energy electrons (100 eV to 20 keV) scanning through the surface of solid specimens to produce its images. The accelerated electrons in a SEM gun interact with atoms in the sample to generate a variety of signals that contain information about its surface topography and composition. These main signals include secondary electrons (SEs), backscattered electrons (BSEs), photons (X-ray). The secondary electrons have a rather low energy because of having experienced energy losses due to scattering event inside the sample. They can only escape the sample if the electron beam is focused sufficiently close to the surface, thus allowing high spatial resolution of the order of 1 nm. The secondary electron then is most valuable for obtaining the sample's morphology and topography. In contrast, the backscattered electrons, reflected elastically from the

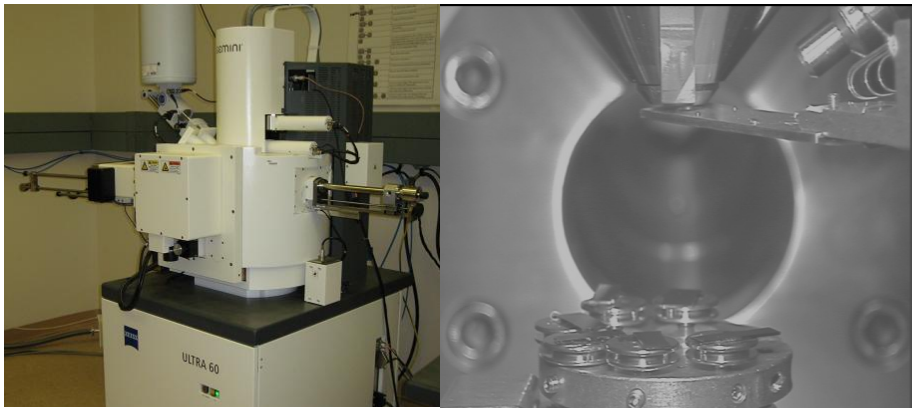

Figure 2.19: Zeiss Ultra 60 FE-SEM at Georgia Tech: (left) a picture of the system. (right) at the bottom is the series of sample holders attached to a big metal plate, at the top is teh in-lens secondary electron (SE) detector. The working distance from the samples to the lens is recommended about 4 mm.

sample, have a rather high energy. They can scatter from a distance within the sample surface (hundreds of nm). The strength of the backscattering signals provides chemical information about the sample because the heavier an atomic nucleus is, the more efficient the back-scattering is. Moreover, electron back-scatter diffraction (EBSD) has been performed to determine crystal structures and orientations of the sample.

Microscope (FE-SEM) in Georgia Tech campus (Fig. 2.19). The ULTRA 60, operating in Ultra-high vacuum environment $\sim 10^{-9}$ Torr, can obtain clear topographic images with the high efficiency in-lens SE detector. The SE mode is suitable for our applications because graphene is just one atomic thickness layer so that it requires to scan a small topmost fraction of the sample. By carefully compared the contrast of different areas of the images, the thickness of graphene layers can be determined [107, 108]. The typical electron beam energy is 5 keV, and the minimum working distance (from the sample to the SE detector) is 4 mm (Fig. 2.19).

CHAPTER III

RECONSTRUCTIONS ON SILICON CARBIDE UNDER SILICON DEPOSITION

Silicon carbide has shown an abundance of surface reconstructions. Different series of the reconstructed phases have been studied extensively on the two hexagonal orientations, i.e., $SiC(0001)$ and $SiC(000\bar{1})$ [109, 110]. The reconstructions depend on the annealing temperature and ambient (UHV, inert gases or Si overpressure, etc). On the Si face, three well-ordered (also stable and well-known) reconstructions are observed with periodicities of (3×3), $(\sqrt{3} \times \sqrt{3})R30°$, and $(6\sqrt{3} \times 6\sqrt{3})R60°$ (see Fig. 3.1)[111–113]. Other studies report more reconstruction phases as (5×5) [114], (6×6) [115], $(2\sqrt{3} \times 2\sqrt{13})R30°$ [116], (2×3), (9×9), and $(2\sqrt{3} \times 6\sqrt{3})R30°$ [117]. On the C face, there are different phases found such as $(2 \times 2)_{Si}$, (3×3), and $(2 \times 2)_C$ (Fig. 3.1) [118]. In which, $(2 \times 2)_{Si}$, and $(2 \times 2)_C$ are different surface structures according to Si rich or C rich composition.

In this Chapter, I will show some new reconstructions on the Si-face and confirmation of the recently reported $(\sqrt{43} \times \sqrt{43})R7.6°$ reconstruction on the C-face [119]. The results were motivated by studying silicon carbide reconstructions before forming epitaxial graphene layers on top of it. This experiment began with an on-axis $6H$-SiC sample which was prepared by ex-situ hydrogen etching to obtain atomically flat surfaces (see Sec. 2.1.2). The sample showed the initial (1×1) phase after transferring to the UHV chamber. Then, it was annealed in the silane overpressure with increasing temperature steps. After each growth, the sample was characterized by in-situ LEED and AES. The details of the experiments and results are presented in the Section 3.2.

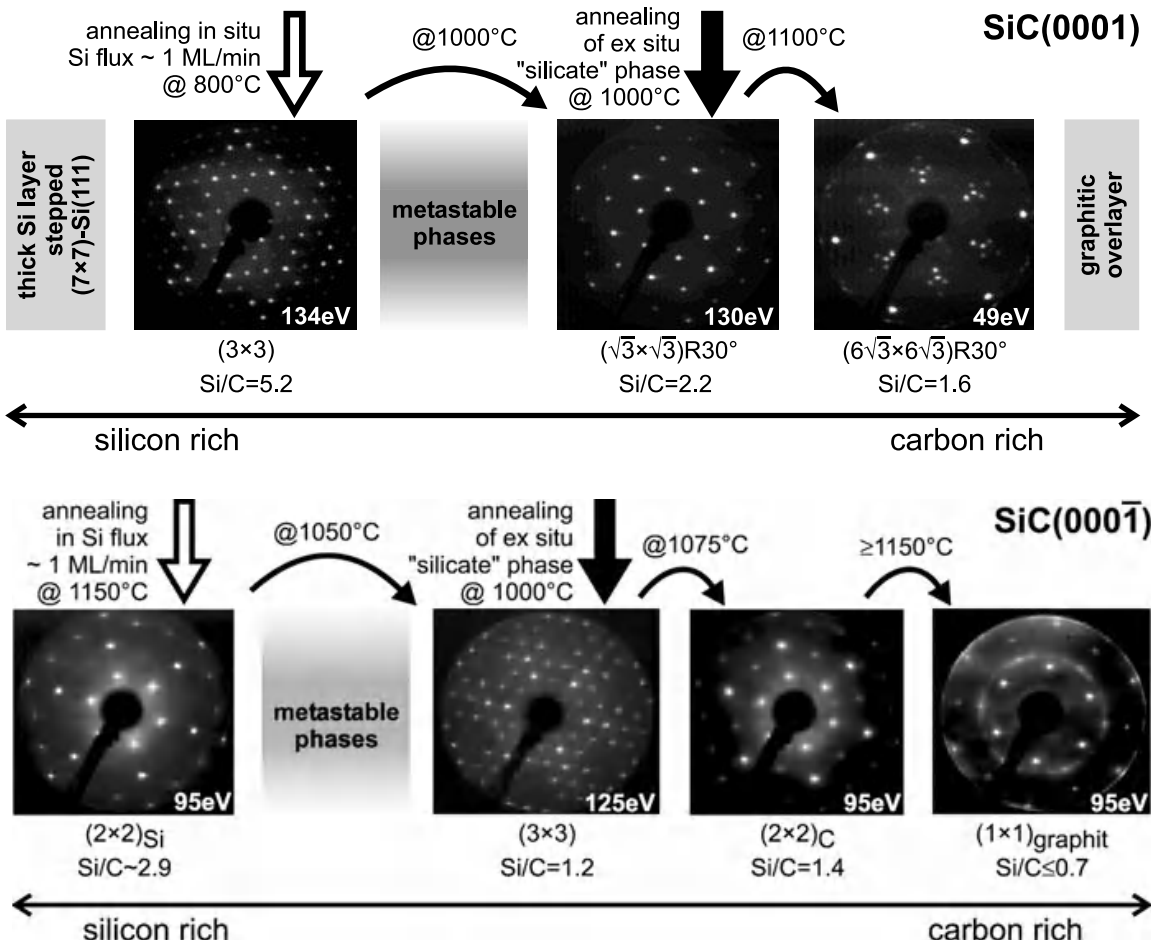

Figure 3.1: LEED patterns of the reconstructed phases on the hexagonal faces at different prepared conditions. The Si/C ratios, measured by AES signals, indicate the silicon rich interfaces at lower temperature and carbon rich interfaces at higher temperature. (top) Si face with a series three stable phases of (3×3), $(\sqrt{3}\times\sqrt{3})R30°$, and $(6\sqrt{3}\times6\sqrt{3})R60°$. (bottom) C face with a series three stable phases of $(2\times2)_{Si}$, (3×3), and $(2\times2)_C$ [109].

Before proceeding to the experimental results, I present an Auger attenuation model to determine the thickness of a thin film. Determination of the number layers of thin films is a challenging task. Many methods have been proposed to count the number, especially the number of graphene layers [120–125]. AES is a surface-sensitive tool which also provides information on the surface chemical compositions to determine the thin film thickness (see Sec 2.3.2) [126–128]. Thus, the Auger peak intensities are valuable to estimate each element density and characterize the surface

structure. This argument is mathematically put into the Auger attenuation model (AAM) in the next section. In general, the model could be applied to any materials with appropriate configurations and parameters. Here, I will utilize it for determining the thickness of silicon and graphene layers on top of SiC based on the $Si : C$ AES intensity ratios.

The Auger attenuation model was studied by former Ph.D. students in our lab: Tianbo Li [49] and David Britt Torrance [86]. Dr. Li originally built the AAM to estimate the number of graphene layers on $Si(0001)$ face based on the CMA Auger equipment. In his model, it is indistinguishable between thin films formed on C- or Si-faces of a SiC substrate. Moreover, the relative Auger intensities of silicon or carbon are simply proportional to its relative element sensitivity factors, the component mole fractions, and the Auger electron backscattering matrix factor [129, 130]. On the other hand, Dr. Torrance revised the AAM model for RFA Auger system. He took excellent efforts to calculate the silicon and carbon sensitivity factors using an analytical formula with recently experimental parameters of silicon and carbon. The differences of C-terminated and Si-terminated faces were considered in his model; however, it was just a factor ($\frac{1}{2}$) added inside the attenuation formula.

In this thesis, I built the AAM from the basics of Auger process that applies for determining the thin film thickness of any elements on top of any substrates. The formula of Auger intensity was derived in general form before applying for different limitations. For the continuum limit of a homogeneous material (section 3.1.2), the Auger current was similar to the Dr. Torrance results. I also considered the atomic layer limitation which was more appropriate for determining the fractional layers. The AAM model was applied for the CMA data to take the advantages of the literature parameters. Then, it was necessary to convert the RFA data to the CMA data before utilizing the model. In the end, the AAM was specifically applied to the cases of silicon and graphene over-layers above SiC bulk with selected parameters from literature.

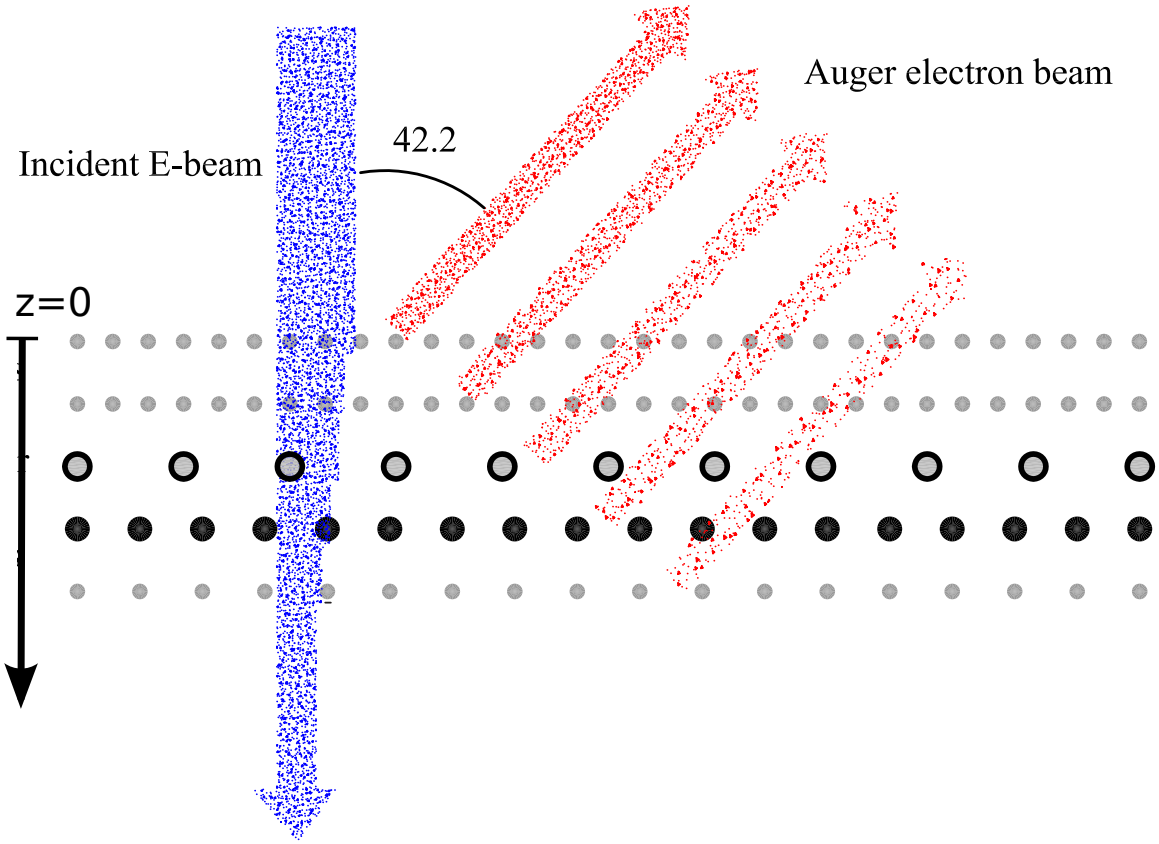

Figure 3.2: Sketch of the AES model. The incident electron beam strikes along the normal direction. It is attenuated because of collision with the surface atoms to create the core holes. The Auger electrons are detected at the angle $\lambda_0 = 42.2$ due to the CMA design [49].

3.1 Auger Attenuation Model (AAM)

3.1.1 Basics

The sample can be described by the elemental densities $\rho_\alpha(z)$, where z is the depth into the sample ($z = 0$ at the sample vacuum interface) and α labels the element. A material β can be characterized by its density function for each element α. The energy of the primary electron beam, incident along the sample normal, is E_p (Fig. 3.2). Ignoring subtleties, the incident flux (number/area/sec) of "primary" electrons (those capable of creating a core hole excitation, nominal energy E_p) incident on any layer dz at depth z as:

$$J_p(z) = J_p(0)e^{-z/\lambda_p}[1 + r_\beta(z, E_p, E_X)] \tag{3.1}$$

where λ_p is the "effective attenuation length" (EAL) [131] for electrons of energy E_p and $r_\beta(z, E_p, E_X)$ is the backscatter coefficient for material β, which accounts for core holes at energy E_X created by backscattered electrons. To simplify, the overlayer is assumed to be thin enough such that the backscattering is dominated by the substrate for all z. Then r_β is a constant value for all z, but still depends on E_p, E_X [132]. The exponential dependence is valid as long as λ_p is much larger than interatomic spacings (which it is, for the few keV energies of interest).

Define $dJ_{\alpha,XYZ}(z)$ to be the Auger intensity of element $\alpha(XYZ)$ emitted from dz at depth z (X core hole, YZ electron states):

$$\begin{aligned}
dJ_{\alpha,XYZ}(z) &= (\text{primary electron flux}) \\
&\quad \times (\text{prob. to create } X \text{ hole in } \alpha \text{ atom}) \\
&\quad \times (\text{prob. of } XYZ \text{ Auger event, given } X) \\
&= (\text{primary electron flux}) \\
&\quad \times \left(\frac{\text{cross-section for creating } X \text{ in } \alpha \text{ atom}}{\text{area per } \alpha \text{ atom in } dz} \right) \\
&\quad \times (\text{prob. of } XYZ \text{ Auger event, given } X) \\
&= J_p(z) \times \frac{\sigma_{\alpha,X}(E_p)}{A/(\rho_\alpha(z) A dz)} \times \gamma_{\alpha,XYZ} \\
&= J_p(z) \times \sigma_{\alpha,X}(E_p) \rho_\alpha(z) \times \gamma_{\alpha,XYZ}\, dz, \qquad (3.2)
\end{aligned}$$

where A is an arbitrary area, $\sigma_{\alpha,X}(E_p)$ is the cross-section for creating core hole X in element α with incident electron energy E_p [133], $\rho_\alpha(z)$ is the 3D density of element α at depth z (Eq. (3.6)), and $\gamma_{\alpha,XYZ}$ is the probability of XYZ Auger events given a collision of the primary electron with the X core hole.

The collected electron flux due to Auger transitions XYZ is affected by 1) the collection solid angle, 2) the detector sensitivity, and 3) inelastic scattering in layers between dz and the detector (integrated over collector solid angle). Even if assuming

that the collection solid angle remains constant, but the detector sensitivity is generally a function of the energy E_{XYZ} and must be determined for the specific detector. Combine the solid angle factor and detector sensitivity into a single function $T(E_{XYZ})$ [134]. For a layer of thickness dz at depth z, the probability of scattering an electron of energy E_{XYZ} from all element α atoms in the layer is

$$\begin{aligned}(\text{prob. of inelastic scattering}) &= \rho_\alpha(z)\sigma_\alpha(E_{XYZ})\,dz \\ &= \frac{dz}{\lambda_\alpha(z, E_{XYZ})},\end{aligned} \tag{3.3}$$

$$(\text{prob. of transmission}) = 1 - dz\sum_{\alpha''}\rho_{\alpha''}(z_j)\sigma_{\alpha''}(E_{XYZ}) \tag{3.4}$$

Finally, summing over layers and considering transmission through all overlying layers, the collected electron current from Auger transition XYZ of an element α can be written as:

$$I_{\alpha,XYZ} = T(E_{XYZ})\sum_{k=0}^{\infty} dJ_{\alpha,XYZ}(z_k)\prod_{j=0}^{k}\left(1 - dz\sum_{\alpha''}\rho_{\alpha''}(z_j)\sigma_{\alpha''}(E_{XYZ})\right) \tag{3.5}$$

Note that the effect of incident (θ_i) and collection (θ) polar angles can be accounted for by 1) replacing ρ_α in Eq. (3.2) (and subsequently) by $\rho_\alpha/\cos\theta_i$, 2) replacing $\rho_{\alpha'}$ by $\rho_{\alpha'}/\cos\theta$ in Eq. (3.5), and 3) inserting the θ-dependence of T (integrating over azimuthal angle as appropriate).

The Eq. (3.5) can not be computed without the appropriate expressions for the density function of each element α, $\rho_\alpha(z)$, in the material β. In the scope of this model, we are only interested in a homogenous material which consists of uniform composition and uniform properties throughout (e.g., it is made up of only one compound or element). In fact, the element density function is three-dimensional complexity. There are two limitations worth considering:

1. **Continuum Perspective**: It is corresponding to continuous density function. In this limitation, each α atoms are spreading out uniformly in all spaces, e.g

$\rho_\alpha(z) = \rho_\alpha$. The assumption is appropriate when dz is much bigger than the atomic unit cell. It means the considerable numbers of material layers, for example, the case of calculating the Auger intensities from a SiC substrate.

2. **Layer Perspective**: It is assumed that the size of an atom is infinitesimal. For regularly-spaced layers of atoms α, the density can be written as

$$\rho_\alpha(z) = n_\alpha \delta(z - z_\alpha - \ell \cdot a_\alpha), \tag{3.6}$$

where n_α is the two-dimensional atomic layer density, z_α is the position at which the atomic planes of the material begin, a_α is the interplanar spacing, and ℓ is an integer ($\ell = 0$ for the α plane located at z_α). In this case, because dz is much bigger than the atomic unit cell, most slices are devoid of atoms.

In the next section, by using appropriate expressions for the density function $\rho_\alpha(z)$, Eq. (3.5) can be computed for each limitation in homogeneous materials.

3.1.2 Continuum Limit for a Homogeneous Material

Consider a homogeneous material β spanning in semi-finite space $0 \leq z < \infty$. Define the "effective attenuation length" for electron of energy E_{XYZ} inside material β as

$$\frac{1}{\lambda_\beta(E_{XYZ})} = \sum_{\alpha''} \rho_{\alpha''\beta} \sigma_{\alpha''}(E_{XYZ}) \tag{3.7}$$

where $\rho_{\alpha\beta}$ is the constant density of element α in material β. If taking $dz = z_k/k$ and changing sums to integrals, Eq. (3.5) becomes:

$$\begin{aligned} I_{\alpha\beta,XYZ} &= T(E_{XYZ}) \int_0^\infty dJ_{\alpha,XYZ}(z) \lim_{k\to\infty} \left(1 - \frac{z/\lambda_\beta}{k}\right)^k \\ &= T(E_{XYZ}) \int_0^\infty dJ_{\alpha,XYZ}(z)\, e^{-z/\lambda_\beta} \\ &= T(E_{XYZ}) \int_0^\infty J_p(0)\,[1 + r_\beta(E_p, E_X)]\,\sigma_{\alpha,X}(E_p)\,\gamma_{\alpha,XYZ}\,\rho_{\alpha\beta}\, e^{-z/\tilde{\lambda}_\beta}\, dz \end{aligned} \tag{3.8}$$

where $\tilde{\lambda}_\beta$ is defined as $\frac{1}{\tilde{\lambda}_\beta} = \frac{1}{\lambda_\beta} + \frac{1}{\lambda_p}$. The final form follows from Eqs. (3.1) and (3.2). The integral can be done, yielding the Auger current from a homogeneous (and semi-infinite) material β:

$$I_{\alpha\beta,XYZ} = T(E_{XYZ}) J_p(0) \left[1 + r_\beta(E_p, E_X)\right] \sigma_{\alpha,X}(E_p)\, \gamma_{\alpha,XYZ}\, \rho_{\alpha\beta}\, \tilde{\lambda}_\beta \tag{3.9}$$

Typically, the material-dependent terms (excluding the density) are lumped together as a "sensitivity factor," $S_{\alpha\beta,XYZ}$, which is tabulated (note that $S_{\alpha\beta,XYZ}$ depends on the primary beam energy) [135]. So the Auger current from an infinite homogeneous material can be written as [136, 137]:

$$I_{\alpha\beta,XYZ} = T(E_{XYZ}) J_p(0)\, \rho_{\alpha\beta}\, S_{\alpha\beta,XYZ} \tag{3.10}$$

3.1.3 Layer Limit for a Homogeneous Material

Use Eq. (3.6) for the atomic density and introduce appropriate integrals in place of sums (the summations could be left as is; just use a Kronecker delta instead of Dirac delta in the density). Write the sum over k in Eq. (3.5) as an integral over $z_k = z$. The sum over α'' is over different elements in the plane located at z_j; we need to integrate the Dirac delta over the infinitesimal layer thickness z/k to change the 3D density to 2D:

$$\begin{aligned} I_{\alpha\beta,XYZ} &= T(E_{XYZ}) \int_0^\infty dJ_{\alpha,XYZ}(z) \prod_{j=0}^{k} \\ &\qquad \left(1 - \sum_{\alpha''} \int_{z_j}^{z_j + z/k} [n_{\alpha''\beta} \delta(z_j - z_{\alpha''} - \ell'' \cdot a_{\alpha''})] \sigma_{\alpha''}(E_{XYZ})\, dz_j \right) \\ &= T(E_{XYZ}) \int_0^\infty dJ_{\alpha,XYZ}(z) \prod_{\alpha'} \prod_{\ell'=0}^{\lceil (z - z_{\alpha'})/a_{\alpha'} \rceil - 1} \left(1 - n_{\alpha'\beta} \sigma_{\alpha'}(E_{XYZ})\right), \end{aligned} \tag{3.11}$$

where the $\lceil\ \rceil$ brackets denote the ceiling function, and the factor is taken to be unity if the upper index is less than the lower index (note the limits would be modified for layers placed at $z < 0$). The final form of Eq. (3.11) holds i) for a single element in layers j, ii) for $n_{\alpha'\beta}\sigma_{\alpha'} \ll 1$, or iii) if the total scattering in the layer is accounted for

by defining an effective element, as $n_{\alpha'\beta}\sigma_{\alpha'} = \sum_{\alpha''} n_{\alpha''\beta}\sigma_{\alpha''}$. These assumptions are valid for the interested homogeneous materials such as silicon carbide, silicon, and graphite, graphene, etc.

Reduce the remaining integral Eq. (3.11) using Eqs. (3.2) and (3.6):

$$I_{\alpha\beta,XYZ} = T(E_{XYZ}) \sum_{\ell=0}^{N_\alpha - 1} J_p(z_\alpha + \ell a_\alpha)\sigma_{\alpha,X}(E_p) n_{\alpha\beta}\gamma_{\alpha,XYZ} \times \left(\prod_{\alpha'} \prod_{\ell'=0}^{N_{\ell\alpha'}-1} \left(1 - n_{\alpha'\beta}\sigma_{\alpha'}(E_{XYZ})\right)\right) \tag{3.12}$$

where $N_{\ell\alpha'}$ denotes the number of α' layers between the emitting layer and the detector,

$$N_{\ell\alpha'} = \lceil (z_\alpha + \ell a_\alpha - z_{\alpha'})/a_{\alpha'} \rceil, \tag{3.13}$$

while N_α is the number of emitting α layers ($N_\alpha \to \infty$ for a semi-infinite sample).

The discussion of angle dependence following Eq. (3.5) applies also to Eq. (3.12), with $n_{\alpha\beta} \to n_{\alpha\beta}/\cos\theta_i$, $\lambda_p \to \lambda_p/\cos\theta_i$, and $n_{\alpha'\beta} \to n_{\alpha'\beta}/\cos\theta$.

Similar to the continuum case [Eq. (3.8)], and particularly for the treatment of multilayers (Sec. 3.1.4), it can be convenient to combine the attenuation factors of the primary beam and the emitted Auger electrons as an "effective attenuation factor" $\tilde{\lambda}_\beta$. However, the decay length λ_p may not be available in terms of elemental cross-sections [as in the Eq. (3.7)]. It may be measured or calculated for a particular non-elemental material (we use $\lambda_{p\beta}$ to show material specificity). This makes it problematic to put the primary beam attenuation in the form of a product of element-specific transmission factors. One way to formally group the factors (which will be convenient for multilayer systems) is to define a fictitious element that has scattering cross-sections $\sigma_{\alpha'}(E_{XYZ}) = 0$ and $\sigma_{\alpha'}(E_p) = 1/(\rho_{\alpha'\beta}\lambda_{p\beta})$. For completeness, we should also specify that the Auger emission probability $\gamma_{\alpha\beta,XYZ}$ is zero for this fictitious element.

3.1.4 Thin Films and Multilayer Materials

In this case, the sample consists of a semi-infinite substrate material β_s and thin film material layers indexed by β. "Thin" implies that most of the backscattered electrons are from the substrate so that the electron backscatter coefficient in Eq. (3.1) is r_{β_s} for all layers (however, the EAL is material dependent: $\lambda_{p\beta}$). This assumption will fail if the attenuation length of primary electrons is comparable to the total thickness of the overlayers.

The extension of Eq. (3.12) to a multilayer thin film requires the appropriate specification of the atomic layer densities. It is convenient to represent this in terms of material layers β, where "material" can also apply to a reconstructed interfacial layer. As for the EAL, some of the previously unsubscripted parameters in J_p may also have a small dependence on β, but this will be accounted for ultimately in the material-dependent sensitivity factors.

Split the sample into material layers, with $z_{\beta=0} = 0$ lying at the vacuum interface and β increasing into the sample. As a convention, we assume that material β ends where $\beta + 1$ begins. It could cause a discrepancy in the layer count if the separation between the last atomic layer of material β is separated from the first atomic layer of material $\beta + 1$ by more than the atomic interlayer spacing $a_{\alpha\beta}$. There are two potential solutions to this glitch: 1) set $z_{\alpha(\beta+1)}$ to a position above the first atomic layer in $\beta+1$, such that the interlayer spacing is less than $a_{\alpha\beta}$, or 2) insert an interface "material" for $\beta+1$, having no atoms, but satisfying the interlayer spacing restriction. The subsequent material layer then becomes $\beta + 2$.

In applying these ideas to generalize Eq. (3.12), we also have to recognize that the attenuation of the primary beam depends on all of the intervening material layers, which requires grouping the exponential attenuation factor in Eq. (3.1) with the attenuation factors for the outgoing Auger electron. Based on the discussion following

Eq. (3.12), we introduce a fictitious element that has zero cross-section for Auger electrons, and whose interlayer spacing corresponds with each material's lattice spacing. The starting positions $z_{\alpha\beta}$ should be coincident with the material layers; small deviations of a fraction of a unit cell should not matter much since the attenuation length of the primary beam is significantly larger than the interlayer spacing. To simplify the notation, we remove the energy argument in $\sigma_{\alpha\beta}$ factors, with the understanding that all cross-sections are for the *XYZ* Auger electrons, with the exception of our fictitious element, for which the energy is that of the primary beam. Summing over material layers, Eq. (3.12) becomes:

$$I_{\alpha,XYZ} = T(E_{XYZ}) \sum_{\beta} \sum_{\ell=0}^{N_{\alpha\beta}-1} J_p(0)[1 + r_{\beta_s}(E_p, E_X)]\sigma_{\alpha\beta,X}(E_p) n_{\alpha\beta}\gamma_{\alpha\beta,XYZ} \times \left(\prod_{\beta'} \prod_{\alpha'} \prod_{\ell'=0}^{N_{\ell\alpha'\beta'}-1} \left(1 - n_{\alpha'\beta'}\sigma_{\alpha'\beta'}\right) \right) \tag{3.14}$$

in which:

$$N_{\ell\alpha'\beta'} = \begin{cases} \lceil (z_{\alpha'(\beta'+1)} - z_{\alpha'\beta'})/a_{\alpha'\beta'} \rceil & \beta' < \beta, \\ \lceil (z_{\alpha\beta} + \ell a_{\alpha\beta} - z_{\alpha'\beta'})/a_{\alpha'\beta'} \rceil & \beta' \geq \beta \end{cases}$$

where the $\beta' < \beta$ means that the attenuating material β' lies closer to the vacuum interface than does the Auger-emitting material β. Recall also that we take the product to be unity if the upper index is less than the lower index. Equation (3.14) is the basic model that we use to predict relative Auger intensities from multilayer materials.

3.1.5 Connection to Tabulated Parameters

Because most tabulations of electron attenuation are in terms of exponential decays, we will rewrite Eq. (3.14) in that form. Conceptually, this requires smearing each atomic layer into an infinite series of infinitesimal-thickness layers, each with vanishing density, and following a prescription analogous to that in Sec. 3.1.2. The result is that each factor $(1 - n\sigma)$ can be replaced by $e^{-a/\lambda}$, where $a/\lambda = n\sigma$ (this is clearly

true for $n\sigma \ll 1$, but in general, the smearing concept is required). The product in Eq. (3.14) is then,

$$\prod_{\beta'}\prod_{\alpha'}\prod_{\ell'=0}^{N_{\ell\alpha'\beta'}-1}\left(1-n_{\alpha'\beta'}\sigma_{\alpha'\beta'}\right) = \prod_{\beta'}\prod_{\alpha'}\prod_{\ell'=0}^{N_{\ell\alpha'\beta'}-1}\left(e^{-a_{\alpha'\beta'}/\lambda_{\alpha'\beta'}}\right)$$
$$= e^{-\sum_{\beta'}\sum_{\alpha'} N_{\ell\alpha'\beta'} a_{\alpha'\beta'}/\lambda_{\alpha'\beta'}}$$
$$= e^{-\sum_{\beta'}\sum_{\alpha'} N_{\ell\alpha'\beta'}/\lambda^*_{\alpha'\beta'}} \tag{3.15}$$

with $\lambda^*_{\alpha'\beta'} = \frac{\lambda_{\alpha'\beta'}}{a_{\alpha'\beta'}}$. Note that the sums include only non-negative values of $N_{\ell\alpha'\beta'}$.

The product $\sigma_{\alpha\beta,X}\gamma_{\alpha\beta,XYZ}$ can be obtained from measured sensitivity factors, given measured or calculated backscattering coefficients r and EALs for different materials [131, 132, 138, 139]. From Eq. (3.10):

$$\sigma_{\alpha\beta,X}\gamma_{\alpha\beta,XYZ} = \frac{S_{\alpha\beta,XYZ}}{\left[1+r_\beta(E_p,E_X)\right]\tilde{\lambda}_\beta} \tag{3.16}$$

with $\tilde{\lambda}_\beta$ corresponding to the collection angle used for the determination of $S_{\alpha\beta,XYZ}$.

Applying these changes to Eq. (3.14) and rearranging a bit yields,

$$I_{\alpha,XYZ} = J_p(0)T(E_{XYZ})\left[1+r_{\beta_s}(E_p,E_X)\right]\sum_{\beta}\sum_{\ell=0}^{N_{\alpha\beta}-1} n_{\alpha\beta}$$
$$\times\left(\frac{S_{\alpha\beta,XYZ}}{\left[1+r_\beta(E_p,E_X)\right]\tilde{\lambda}_\beta}\right) e^{-\sum_{\beta'}\sum_{\alpha'} N_{\ell\alpha'\beta'}/\lambda^*_{\alpha'\beta'}} \tag{3.17}$$

Note that $J_p(0)$ is in common to the Auger currents from all elements in the sample so that it is irrelevant for relative intensity measurements. On the other hand, the factors $T(E_{XYZ})$ and $[1+r_{\beta_s}(E_p,E_X)]$ may be different for distinct Auger peaks. As it is defined previously, $T(E_{XYZ})$ is the combination of the solid angle factor and detector sensitivity. Because the collection solid angle remains constant throughout the experiments, $T(E_{XYZ})$ is proportional to the multiplier gain of the detector. Figure 3.3 is a plot of the electron multiplier gain variation with energy of Auger electrons from "Handbook of Auger electron spectroscopy", Davis et al. [134]. The relative Auger sensitivities of the elements with respect to the primary electron

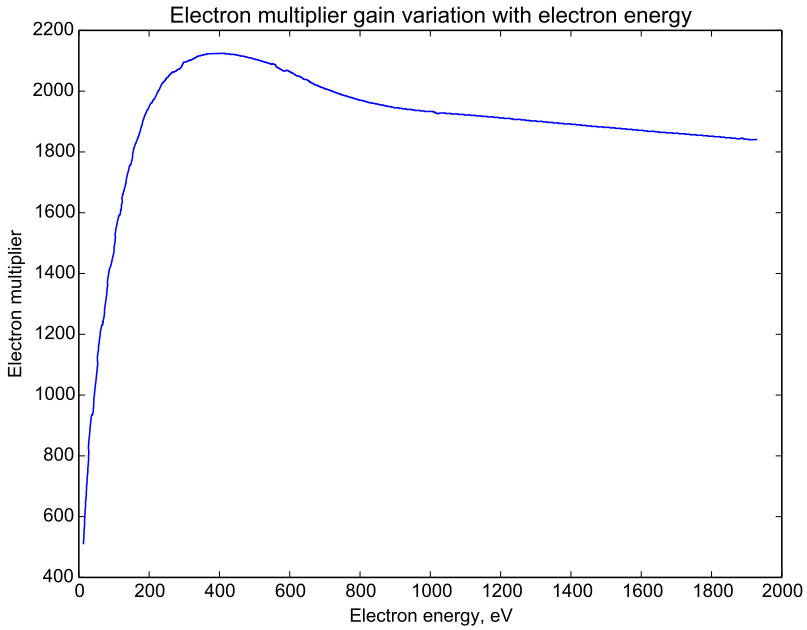

Figure 3.3: Re-plot of the electron multiplier gain versus Auger electron energy from Davis et al [134].

energy of 3 keV, 5 keV, 10 keV are also found in Davis' handbook [134]. The other parameters are taken from National Institute of Standards and Technology (NIST) database: backscattering factors $r_{\beta_s}(E_p, E_X)$ [132] and electron effective attenuation lengths (EAL) λ_{beta} [131]. Equation (3.17) is the most convenient form for practical use, with $N_{\ell\alpha'\beta'}$ from Eq. (3.14).

3.1.6 Thin film layers on SiC

It is the time to apply the Eq. (3.17) for our interesting problem: determining the number of silicon or graphene thin film layers on top SiC substrates. If the films and the substrate are comprised of completely different elements, it is relatively straightforward to estimate the film thickness based on the Auger signals of the film elements. However, the carbon or silicon element presents on both the films and substrates, thus making the problem is further complicated. The ratios of Auger intensities are considered to eliminate the system errors. In our Auger system, the energy of the primary

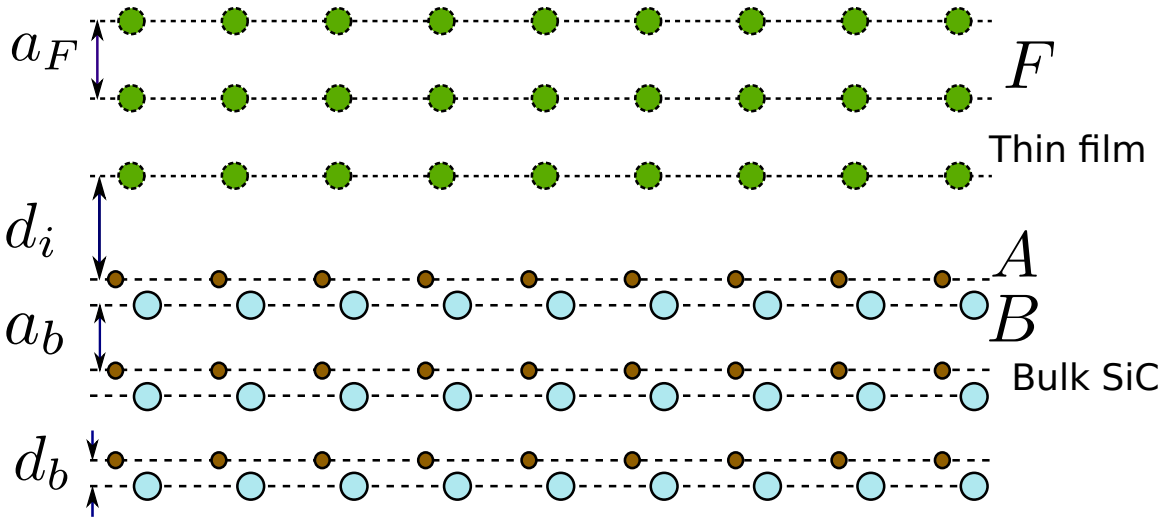

Figure 3.4: Sketch of thin films on SiC bulk: AB is the bilayer silicon carbide (depending on C-termination or Si-termination). F is the graphene or silicon overlayers which are epitaxial grown on top of SiC substrate.

electron beam is 2.5 keV which provides the silicon peak, LMM, at 90 eV and carbon peak, KLL, at 272 eV. Thus, the $Si:C$ ratios of these peaks is the only input of the AAM to calculate the thin film layers in our situation.

The SiC substrates in the model are either C-terminated face or Si-terminated face. As discussed in section 1.3, each bilayer, parallel to the basal plane, consists of one C layer and one Si layer. Without loss of generality, silicon carbide bulk is denoted as AB ($A(B)$ is either C or Si (Si or C) corresponding to a C-face or a Si-face respectively) and thin film is denoted as F (F is either G or Si corresponding to graphene or silicon epitaxial layers). Figure 3.4 shows the sketch of the model with the various parameters of inter-plane spacings and in-plane atomic densities. For bulk silicon carbide, the spacing of Si and C plane in each bilayer is $d_b = 0.63$ Å, and the distance between two closest bilayers is $a_b = 2.51$ Å. The densities of C or Si atoms in each plane are the same, $n_C = n_{Si} = n_b = 12.25 \times 10^{14}$ atoms/cm^2. For thin film of graphene, it is appropriate to use the graphite layer spacing, $a_g = 3.35$ Å, and density, $n_g = 38.16 \times 10^{14}$ atoms/cm^2. For thin film of silicon, if the epitaxial plane is parallel to the $Si(001)$ face, the layer spacing and density are $a_{si} = 1.36$ Å,

$n_{si} = 6.78 \times 10^{14}\,\text{atoms/cm}^2$. Interface layers between graphene or silicon and SiC substrate have not completely understood yet [68, 69, 114, 119, 140]. When the configuration of the interfaces is well defined, the Auger current is calculated exactly using Eg. (3.17) for the multilayer materials. To simplify, the ill-defined interface layers are ignored. It is worth to note that in the case of the graphene thin film, the first layer is counted as graphene layer on the C-face while considered as a buffer layer on the Si-face. The distance between the film layer and the bulk material is d_i.

Suppose there are n layers of thin film F (either graphene or silicon) on top of bulk material AB as shown in Fig. 3.4. Considering a specific Auger peak at energy level E_F, the Auger current contributed by the thin film is calculated easily from Eq. (3.12) with a single element:

$$I_{n,F} = T(E_F)J_p(0)[1 + r_{SiC}(E_p, E_F)]\sigma_F(E_p)\gamma_F n_F \times \sum_{l=0}^{n-1}(1 - n_F\sigma_F(E_F))^l e^{-\frac{la_F}{\lambda_p^F}} \quad (3.18)$$

As previous discussions, the backscatter coefficient is dominated by the silicon carbide substrate and remains constant throughout the calculation as long as the film is thin enough. The terms inside the sigma symbol are the attenuation of the Auger electron (factor $(1 - n_F\sigma_F)^l$) and primary electron beam (factor $e^{-\frac{la_F}{\lambda_p^F}}$). The former term is in the form of a power factor instead of an exponential factor because of the layer limit (as shown in section 3.1.3). If it is approximately in exponential factor and combined with the latter term to an "effective attenuation factor, the result is similar to the continuum limit in section 3.1.2.

Next, the Auger current of the "top" element, A (at energy level E_A), from the semi-finite substrate byond n layers of thin film F:

$$\begin{aligned} I_{A,E_A} = {} & T(E_A)J_p(0)[1 + r_{AB}(E_p, E_A)]\sigma_A(E_p)\gamma_A n_A(1 - n_F\sigma_F)^n e^{-\frac{na_F}{\lambda_p^{AB}}} \\ & \times \sum_{l=0}^{\infty}(1 - n_A\sigma_A)^l(1 - n_B\sigma_B)^l e^{-\frac{la_b}{\lambda_p^{AB}}} \end{aligned} \quad (3.19)$$

Similarly, the Auger current of the "bottom" element, B (at energy level E_B):

$$I_{B,E_B} = T(E_B)J_p(0)[1 + r_{AB}(E_p, E_B)]\sigma_B(E_p)\gamma_B n_B(1 - n_F\sigma_F)^n e^{-\frac{na_F}{\lambda_p^{AB}}} \times \sum_{l=0}^{\infty}(1 - n_A\sigma_A)^{l+1}(1 - n_B\sigma_B)^l e^{-\frac{la_b + d_b}{\lambda_p^{AB}}} \tag{3.20}$$

However, it is easy to realize that the "bottom" element B is suffered two additional attenuation factors: $(1 - n_A\sigma_A)$ for the Auger electron and $e^{-\frac{a_b}{\lambda_p^{AB}}}$ for the primary electron beam. The reason is that each layer of the element B is under the relative layer of the element A within the distance a_b. As discussed in the tabulated parameters section 3.1.5, the attenuation factor $(1 - n\sigma)$ can be replaced by $e^{-a/\lambda}$ where a is the interlayer spacing and λ is the attenuation length. Thus, the Auger currents can be calculated using the tabulated parameters.

At the end, the ratio of silicon and carbon intensities is either $\frac{I_{n,F}+I_{A,E_A}}{I_{B,E_B}}$ or $\frac{I_{n,F}+I_{B,E_B}}{I_{A,E_A}}$ depending on the thin film of silicon or graphene and the substrate termination of C or Si face. The benefits of taking ratios are to reduce system errors and cancel out the system dependent factors. The energies of the LMM (Si peak) and KLL (C peak) Auger electrons are 90 eV and 272 eV respectively. Based on the Fig. 3.3, the ratios of electron multiplier gain is $\frac{T(E_{LMM})}{T(E_{KLL}} = 1444/2068 \approx 0.7$. The products $\sigma_X(E_p)\gamma_X$ $(X = F, A, B)$ can be calculated from sensitivity factors, backscattering coefficients and EALs. The relative Auger sensitivities of Si and C elements with respect to 3 keV primary electron energy are 0.35 and 0.2 respectively. Due to the complexity of the EAL measurement, various sources in literature provided the values a bit different. The discussion of these sources could be found in Dr. Torrance's thesis for more details [86]. In this thesis, I used the average practical EALs which are calculated from the National Institute of Standard and Technology (NIST): Electron Effective-Attenuation-Length Database - Version 1.3 [131]. The backscattering factors were also obtained from NIST: Backscattering-Correction-Factor Database for

Table 1: Electron Effective-Attenuation-Length (EAL) in Angstrom ($\mathring{A}$). Obtained from NIST software [131].

Materials/Electron Energies	90 eV	272 eV	2.5 keV
Graphite	3.883	8.730	45.28
Silicon	3.433	7.532	40.08
Silicon carbide	3.165	6.776	36.51

Table 2: Backscattering-Correction-Factor Database for Auger Electron Spectroscopy. Obtained from NIST software [132].

Elements	BS factors $(1 + r)$
Si in SiC at 90 eV	1.100 ± 0.018
Si in Si bulk at 90 eV	1.078 ± 0.016
C in SiC at 272 eV	1.315 ± 0.020
C in Graphite at 272 eV	1.139 ± 0.017

Auger Electron Spectroscopy - Version 1.1 [132]. The specific EALs and backscattering factors, obtained from NIST software, are listed on the tables 1 and 2.

Figure 3.5 shows the numerical results of the AES model for estimating the thin film thickness of silicon or graphene on SiC substrates. In the numerical calculation, the collection polar angle $\theta = 42.2\,^\circ$ is taken into account for the CMA system [141]. The python code for the model can be found in the Appendix A. For the thin film of silicon, the multilayer (ML) number is defined in term of the silicon amount on a bilayer SiC. The inset of the figure obviously reveals that the $Si : C$ ratio is exponentially proportional to the thin film thickness. The bare silicon carbide (without any overlayers) has greater $Si : C$ ratio on the Si-face than that on the C-face and the ratios are bigger than unity on both faces. The ratios in the case of bare silicon carbide are also considered as a practical approach to verify the correctness of the model. Unfortunately, preparing the absolute clean SiC surfaces without any oxidation is challenging. However, it is possible to compare the model to the known reconstructions as shown in Fig. 3.1. For example, the $(\sqrt{3} \times \sqrt{3})R30^\circ$ phase, which

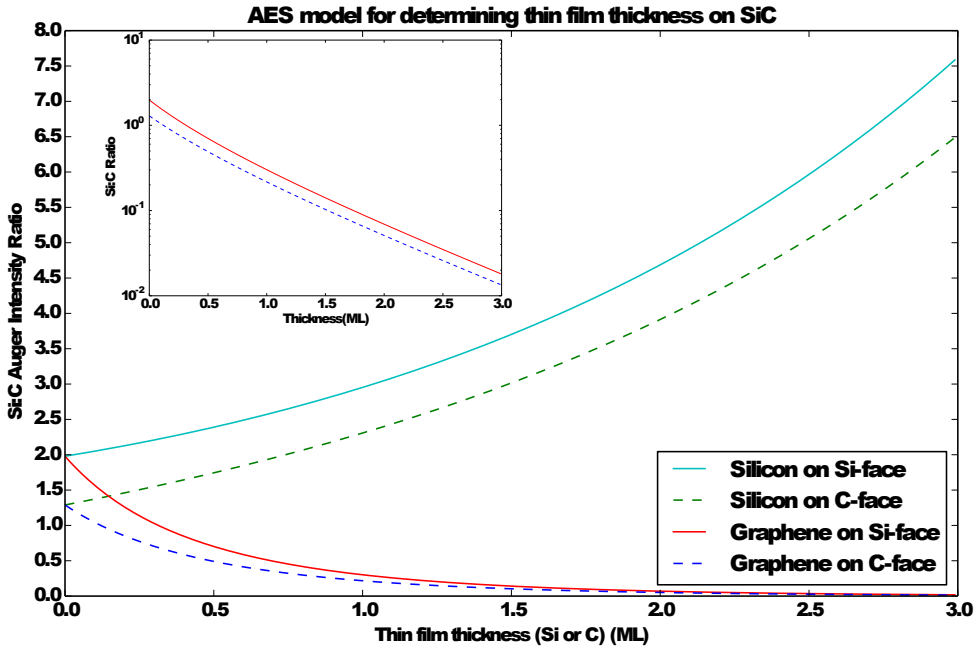

Figure 3.5: AES model for CMA data to determine the thin film thickness of the epitaxial growth silicon or graphene layers based on the Si:C Auger intensity ratios. A silicon film layer is defined equally to the silicon density in a SiC bilayer ($12.25 \times 10^{14}\,\mathrm{cm}^{-2}$) while the carbon density of a graphene layer is $38.16 \times 10^{14}\,\mathrm{cm}^{-2}$. The solid line is the curve for $SiC(000\bar{1})$ face, the dash line is the curve for $SiC(0001)$ face. Inset is the semi-log plot for the case of determining graphene thickness.

composed of Si-adatoms with one ad-structure per unit cell as concluded from STM data, has the Si:C ratio of 2.2 [111]. The result agrees with the calculation from the AAM model, where the ratio is corresponding to the one-third of Si film thickness. Moreover, the average graphene thickness on the Si-face determined by the model is in agreement with that estimated from the SEM images as shown in the next chapter.

3.1.7 Convert Auger data: from RFA to CMA

For completeness of using the Auger Attenuation Model, this section is devoted to introducing the method of converting the RFA data to CMA data while retaining the scaling and resolution. The Auger system, used in conjunction with LEED in the growth system, is the Retarding Field Analyzer (RFA) as discussed in section

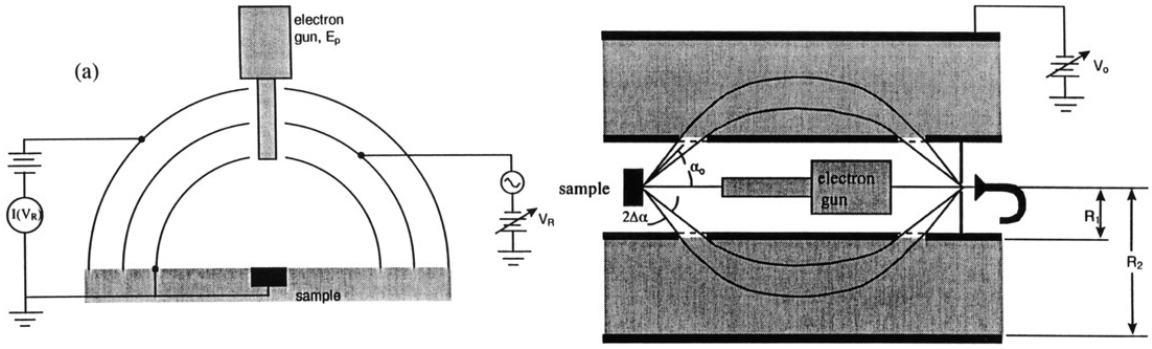

Figure 3.6: (a) Schematic of two Auger types. (a) The Retarding Field Analyzer (RFA) with three concentric grids in which the inner and outer grids are at ground potential while the middle grid has negative bias (retarding). (b) The Cylindrical Mirror Analyer (CMA) consists of two concentric cylinders in which the inner cylinder is held at ground potential while the outer cylinder is at negative potential. Adapted form [98].

2.3.2. Another Auger equipment, the Cylindrical Mirror Analyzer (CMA), is located in our RT STM system. Figure 3.6 compares these two types schematically. In the geometric point of view, the RFA collects electrons in a wide range of solid angles while CMA's collecting angle is selective. Specify for our system, the LK LEED/Auger has a viewing angle of $103\,^\circ$ and the acceptance angle of our CMA, $\alpha_0 \pm \Delta\alpha$, is $42.2\,^\circ \pm 6\,^\circ$. Moreover, in the RFA, the signal at the collector is an integral of $N(E)$ from Auger pass energy up to the incident electron beam energy. The actual Auger signal of RFA is $dN(E)/dE$ which is the second derivative of the collector signal. On the other hand, the CMA Auger signal is $d(N(E) \cdot E)/dE$ which is the first derivative of the CMA collector signal. As the results, the energy resolution, the minimum energy difference between two electrons which can be distinguished, of the CMA is $\Delta E/E = const$ compared with that of RFA where ΔE is constant for all E. Because of a better signal-to-noise than the RFA system, CMA Auger is the most popular choice in the surface science community [142]. It is also the main reason that AAM is built for CMA data.

The python codes to convert RFA data to CMA data is presented in the Appendix B. At first, it is necessary to read the raw data from different formats because the

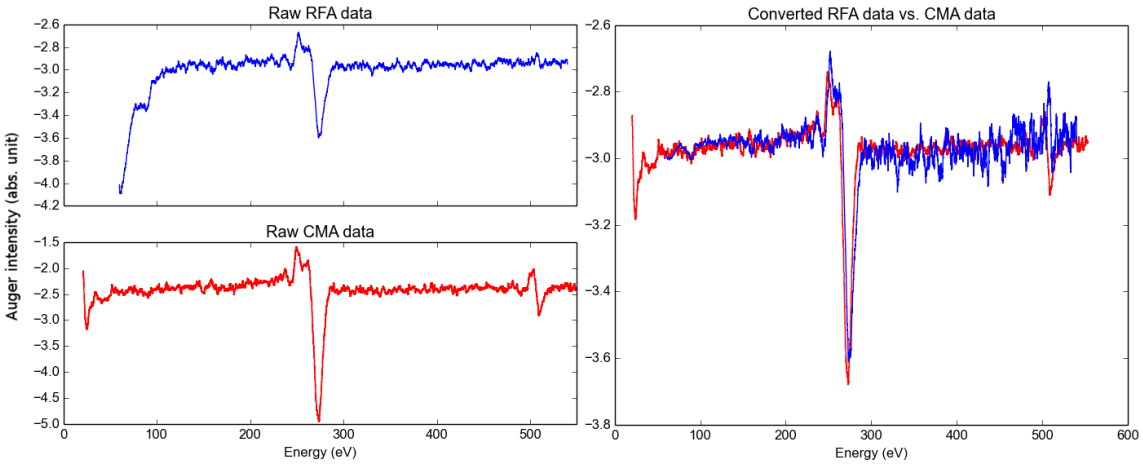

Figure 3.7: (a) Raw data from RFA Auger in the growth system. (b) Raw data from CMA Auger in the RT STM system. (c) The RFA data after converted (blue) and the raw CMA data (red). The two data has been subtracted from the constant background and rescaled.

CMA software stores data in netCDF files while the RFA software keeps data in cPickle files. The raw RFA data are Auger signal, $dN(E)/dE$, versus Auger electron energy, E. Thus, the total number of Auger electrons, $N(E)$, is simply obtained by integrating the RFA signal over the energy range. After that, the CMA signal is calculated as the first derivative of $N(E) \cdot E$ with respect to E. Furthermore, a multiplier gain is added to the RFA signal because the CMA collector is sensitive to the energy (the multiplier gain curve is taken from the Auger handbook as shown in the Fig. 3.3).

I also set up an experiment to verify the accuracy of the method. A graphitized silicon carbide sample was scanned by both the RFA and CMA Auger in our lab. The Auger measurements were performed on the same face, the C-face, of the same sample. The results are shown in the Fig. 3.7. The top left of the figure is the raw data taken from the RFA Auger in the growth system while the bottom left of the figure is the raw data obtained from the CMA Auger in the RT STM. In both cases, there is a huge C peak at 272 eV and a smaller Si peak at 90 eV as predicted. The O (oxygen) peak, $\sim$ 513 eV, is clearly visible in the CMA case but quite small in

the RFA. I applied the method above to convert the RFA data to the CMA data, then comparing with the real CMA data as shown on the right of the Fig. 3.7. A constant background was subtracted from both data sets, and they were rescaled to fit the C peaks. At first, the shape of the C peaks is incredibly similar in both cases. Moreover, the Si peaks are very close to each other even though they are quite small. At the interested energy range, below 300 eV, the converted RFA and CMA data fit very well. Unfortunately, the RFA data become noisier at increasing energies, thus making the oxygen peak unclear under large background noises at high energies. One of the reason is the resolution window which RFA data becomes worse at the high energy range. Moreover, an energy step of RFA equipment is five times as large as that of CMA equipment (82 meV versus 16 meV respectively as calculated from the raw data).

3.2 Experiments and Results

An on-axis 6H-SiC wasstudied in the experiments. The sample ID using in our logbook was 6H-HB019. The sample was picked up from the Cree's wafer and followed the general experimental routine as discussed before in the Section 2.2.1. The hydrogen etching method was effective in achieving the atomically flat surfaces on both the Si- and C-faces as indicated later in the AFM scans. The sample then transferred into the UHV growth system where a series of growths and characterizations was performed. It is worth to repeat that both the C face and Si face were studied simultaneously throughout all experiments because of the sample designs. The sample was annealed by the graphite furnace while flowing the gas mixtures of 0.7 % silane/argon. The pressure inside the growth chamber was monitored by the Convectron gauge with the gas correction factor of $R = 1.29$ for argon [91]. For the temperature growth profile, it started at room temperature (RT) then kept constant at the prepared temperature (500 °C for (300 s). Then the temperature ramped

quickly ($\sim$ 20 s) to the target temperature. The growth time varied from several minutes to an hour. A python program, named pyTherm.py, applied a PID loop to control the power of the RF heater [90]. The parameters of the PID loop were chosen to minimize the overshoot of the target temperatures (less than 10 °C).

The starting surfaces showed the $(\sqrt{3} \times \sqrt{3})R30°$ reconstruction on both faces after ex-situ hydrogen etching as the results of the silicate layers due to the interaction with the present oxygen on air [143, 144]. It was confirmed by the oxygen peak from the Auger signals. The first step, the sample was annealed to 850 °C for 10 mins under the flowing of the mixture silane/argon gas. The pressure of the chamber was $P = 2.0 \times 10^{-2}$ Torr which was corresponding to the silicon pressure of $P_{Si} = 1.4 \times 10^{-4}$ Torr. After the growth, LEED revealed the (1×1) pattern on the Si-face and still remained the $(\sqrt{3} \times \sqrt{3})R30°$ phase on C face. I repeated the experiments at increasing temperatures with the same gas-flowing condition for 30 mins each. On the Si face, I found some new reconstructions which have not reported before, as shown in the next Section 3.2.1, then ending up with the $(6\sqrt{3} \times 6\sqrt{3})R30°$ phase of graphene. On the other hand, the LEED patterns on the C-face showed some well-known phases ((2×2) and 3×3)) before graphitization. At a different experiment, the $(\sqrt{43} \times \sqrt{43})R7.6°$ reconstruction was obtained as reported by others [119]. The result for the C-face is presented later in section 3.2.2 of this chapter.

3.2.1 New reconstructions on $SiC(0001)$ under silicon deposition

To start, Fig. 3.8 shows the ex-situ AFM image of the Si-face of the sample $6H$-$HB019$. The top is the starting surface which was prepared by hydrogen etching at 1400 °C. The surface was atomically flat with regular steps as expected. The line profile, used facet level, reveals the step height of 1.5 nm that equals to the height of six bilayers (or one unit-cell height). After the final step of growth in silane/argon at 1300 °C for 30 mins, the sample was transferred out to characterize via the AFM

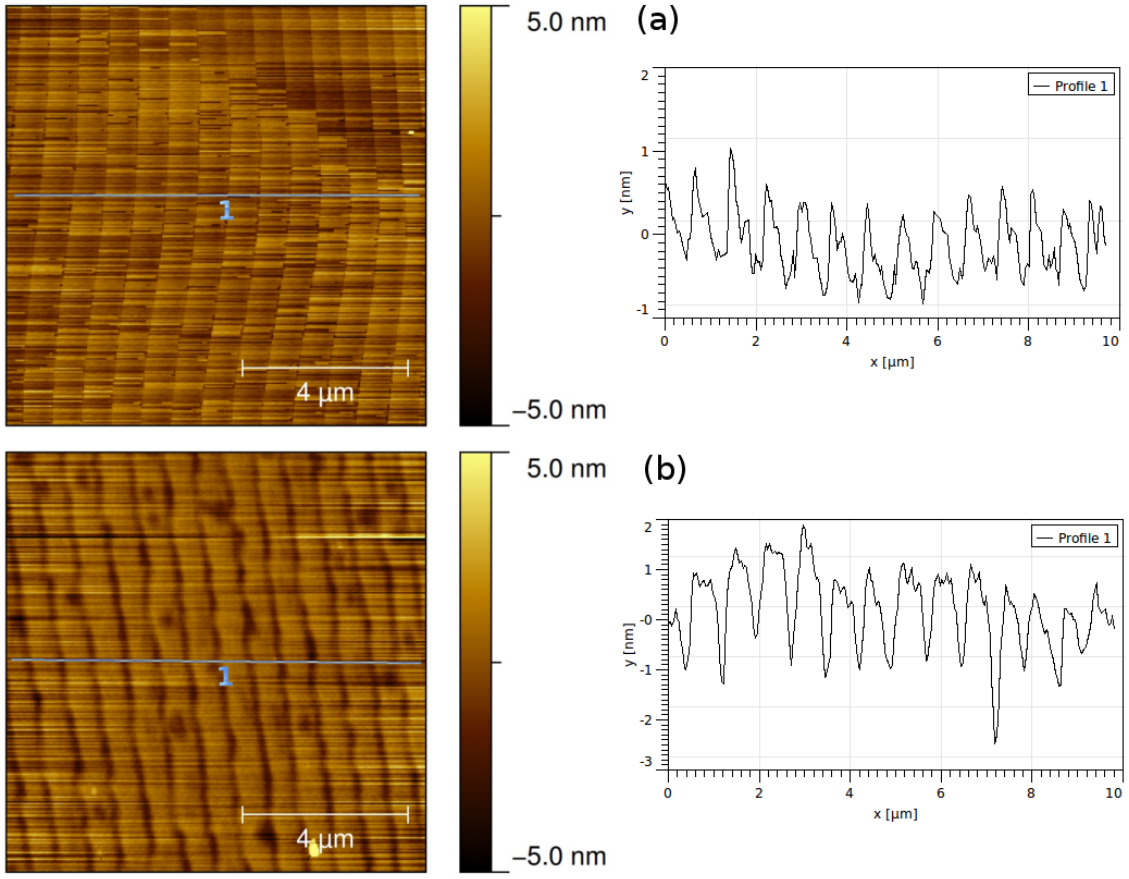

Figure 3.8: AFM images of the Si-face: (a) Starting surface is atomically flat with regular steps of a unit cell height 1.5 nm. (b) Morphology of the surface after graphitization. The steps are still one unit cell height, and graphene is grown the step edges.

again. The morphology of the sample remained similar to the starting surface with equidistant spacing steps as shown in the bottom of the figure. However, the step edges were not as straight as before. The line profile still indicates unit-cell step heights, but it was etched deeper right at the step edges. The LEED patterns of the surface, presented later, showed the mixture of $(6\sqrt{3}\times 6\sqrt{3})R30^\circ$ and graphene spots. From the Si:C ratios of the Auger spectra, the AAM also indicated the morphology of the surface includes a full buffer layer plus additional graphene on top. These results implied that the graphitization processes were started at the edges of the steps. The EFM also confirmed the conclusion, thus making the possibility of growing graphene

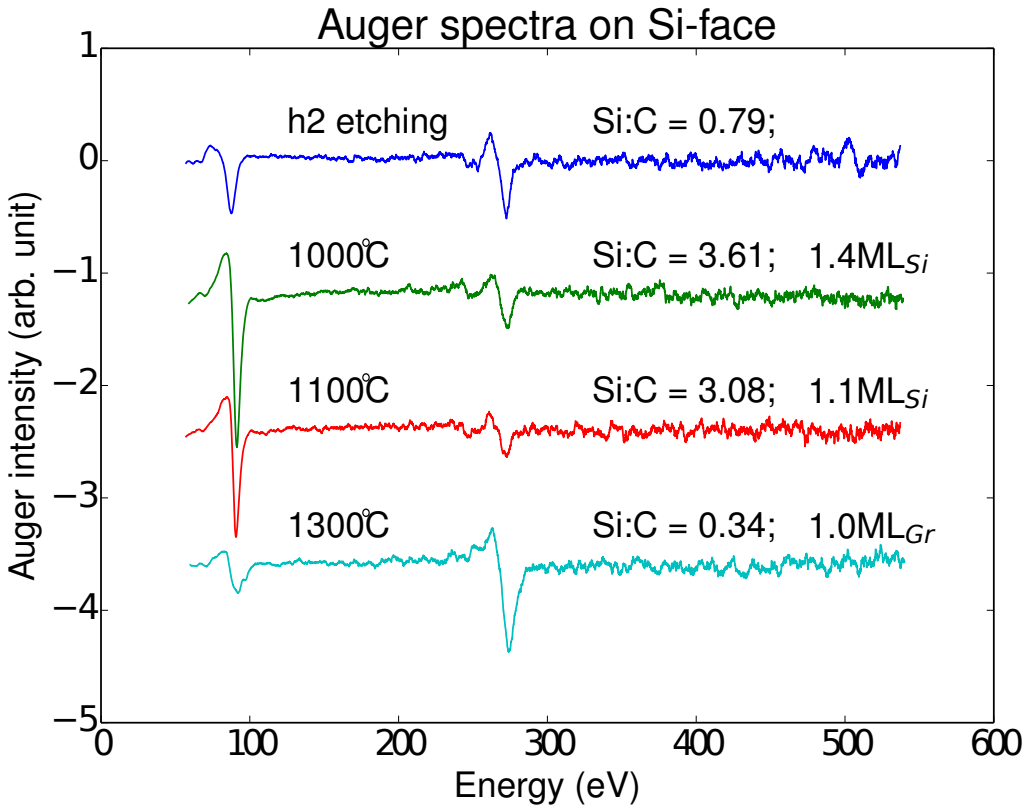

Figure 3.9: Auger spectra of the Si-face after ex-situ hydrogen etching and annealing at different temperatures in the silane/argon gas mixtures. The starting surface has small oxygen peak which is vanished after annealing. The Si:C ratios decrease as the annealed temperatures increase.

nanoribbons (GNRs) along the natural steps.

Figure 3.9 shows the Auger spectra of the $Si(0001)$ surface at each annealing step. The starting surface was treated using ex-situ hydrogen etching. Even transferring the sample inside the UHV system within several hours, oxygen peak clearly exists alongside with silicon and carbon peaks as seen from the top line. The presence of the oxygen caused the formation of the silicate layer on top of the bare SiC substrate. The confirmation of the silicate layer was the $(\sqrt{3} \times \sqrt{3})R30°$ reconstruction from LEED [144]. The Si:C ratio of only 0.79, smaller than that predicted by AAM for a clean surface, might result from the silicate layer. After annealing at 850 °C, the oxygen peak disappeared and the surface reconstruction became (1×1) because of

the oxygen evaporation. Then the sample was annealed at 1000 °C for 30 mins under Si pressure of 1.4×10^{-4} Torr. The oxygen peak was gone as expected, and the Si:C ratio increased to 3.61 due to silicon deposition. At higher temperature, 1100 °C, and the same silicon overpressure, the Si:C ratio was slightly smaller, 3.08. As the Si:C ratios almost remained constant in the temperature range of 1000 °C-1100 °C, the number of silicon deposited on the surface would be equal to the one evaporated from the surface. From the AES model, the ratios implied a silicon film thickness of $1.1 - 1.4$ ML. At the final temperature of 1300 °C, the Si:C ratio reduced to 0.34. The change of the C-peak shape of the last spectrum also confirms the formation of epitaxial graphene on the $Si(0001)$ surface [145]. Based on the AES model, the surface becomes carbon-rich with approximately one graphene layer (buffer layer).

The main result is new reconstructions on the Si-face discovered by LEED after annealing at 1000 °C for 30 mins under Si pressure of 1.4×10^{-4} Torr (Fig. 3.10). The sharp spots of the pattern, from the top left of the figure, implies the well-ordered surface. The new reconstruction has not reported elsewhere in the literature. Comparing the pattern with all possible reconstructions for the hexagonal surface (Table 23.3 in the Handbook of surface imaging and visualization [146]), the phase possibly belongs to the $(\sqrt{3} \times 7)R30^\circ$ reconstruction. To verify the prediction, the LEED pattern was matched with the $(\sqrt{3} \times 7)R30^\circ$ reciprocal lattice. It turned out that most of these spots were matched pretty well as shown in the bottom left of the figure. However, some spots did not belong to this reconstruction. Further investigating recommended that the remaining spots be from another reconstruction as shown later. The bottom right of the figure is a possible atomic model of the reconstruction. The $(\sqrt{3} \times 7)R30^\circ$ reconstruction layer is fitted well with the $Si(100)$ plane of the silicon bulk. The stress (mismatch) of the plane with the $SiC(0001)$ is less than 2 %.

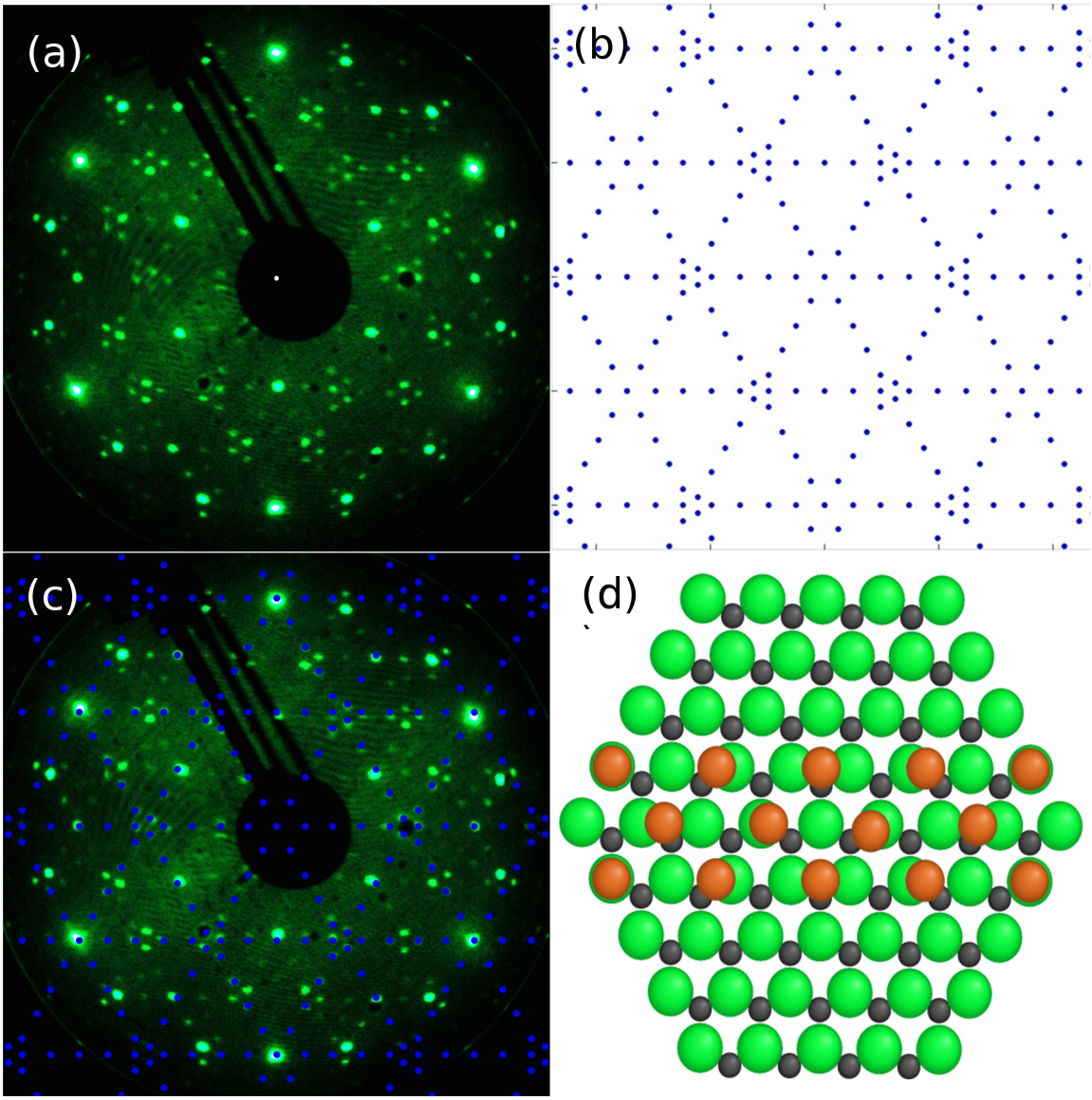

Figure 3.10: LEED pattern of the Si face after annealing at 1000 °C for 30 mins: (a) LEED pattern. (b) $(\sqrt{3} \times 7)R30°$ reciprocal lattice. (c) Matching the LEED pattern to the reciprocal lattice. (d) A unit cell of $Si(100)$ on top of $SiC(0001)$ plane in which green, black, and red circles represent Si, C atoms in SiC and Si in Si bulk respectively.

For completeness, the remaining spots which did not belong to $(\sqrt{3} \times 7)R30°$ phase were matched to the $(2\sqrt{3} \times \sqrt{13})R30°$ reconstruction as shown in the Fig. 3.11. Again, the top left of the figure shows the unit cell of the $Si(140)$ plane from silicon bulk on top of $SiC(0001)$ plane. Calculating from the atomic model, the stress of the $Si(140)$ unit cell with the $(2\sqrt{3} \times \sqrt{13})R30°$ reconstruction is also less than

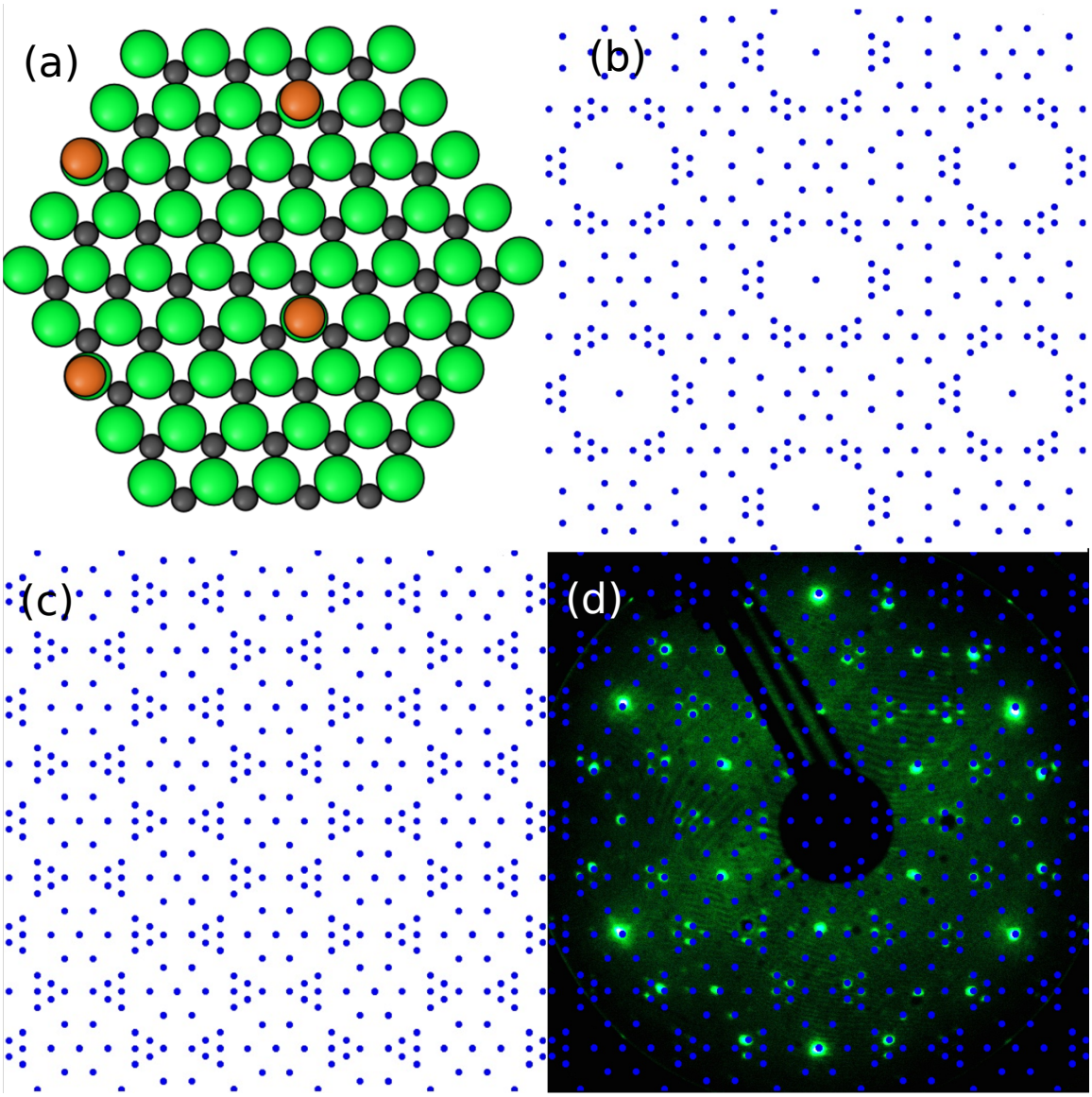

Figure 3.11: (a) A unit cell of $Si(140)$ on top of $SiC(0001)$ plane. (b) $(2\sqrt{3} \times \sqrt{13})R30°$ reciprocal lattice. (c) Superposition of $(\sqrt{3}\times 7)R30°$ and $(2\sqrt{3}\times\sqrt{13})R30°$ reconstructions. (d) Matching the LEED pattern to the reciprocal lattice.

2 %. The top right of the figure is the $(2\sqrt{3} \times \sqrt{13})R30°$ reciprocal lattice and the bottom left of it is the superposition of the $(\sqrt{3} \times 7)R30°$ and $(2\sqrt{3} \times \sqrt{13})R30°$ reconstructions. The bottom right of the figure confirms that the superposition of two phases covers all of the spots from the LEED pattern. Thus, the epitaxial silicon film is the mixture of two reconstruction layers. The results quite agree with the Si-layer thickness of 1.4ML based on the AAM model.

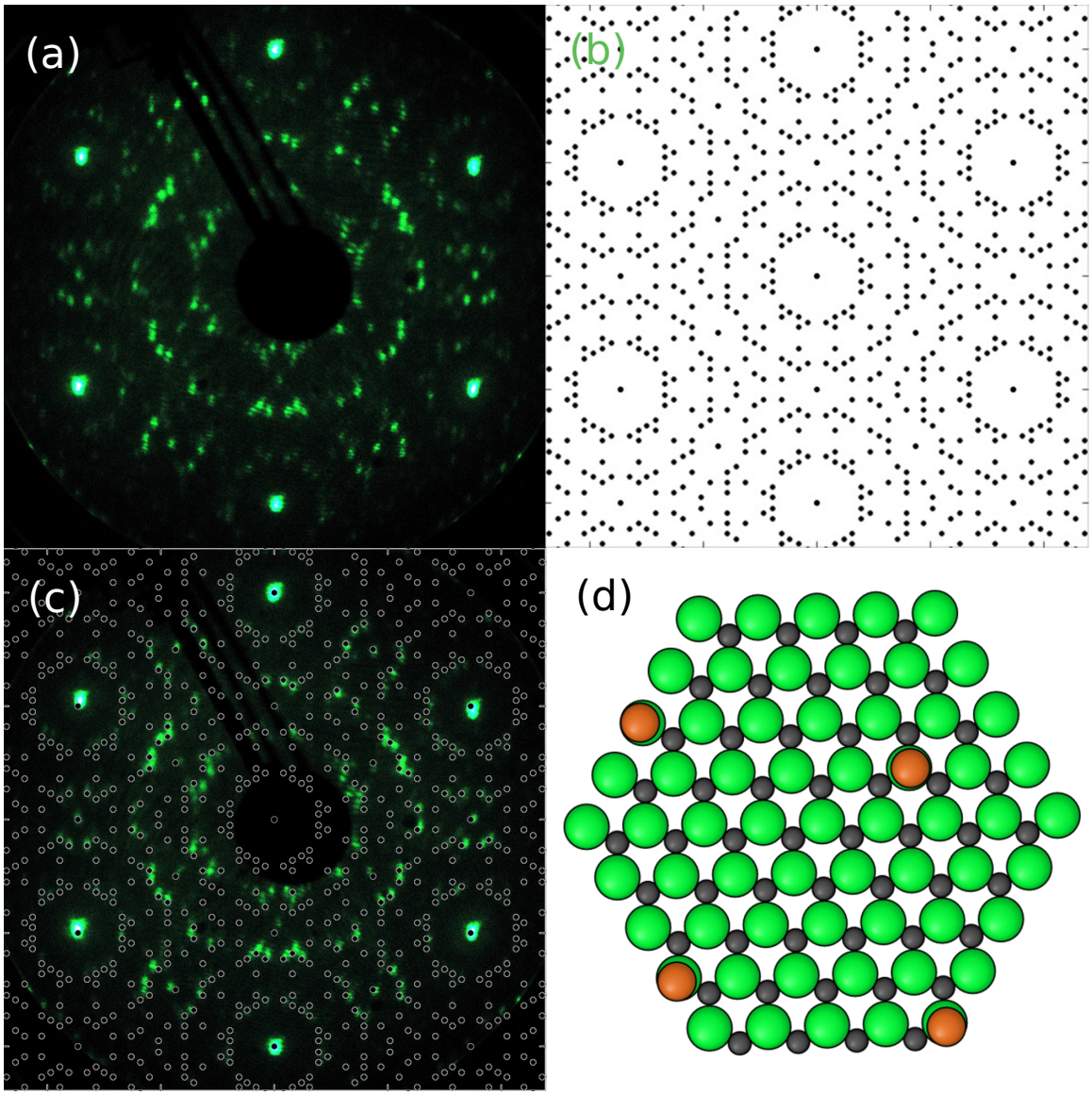

Figure 3.12: LEED pattern of the Si face after further annealing at 1100 °C: (a) complicated LEED pattern. (b) $(\sqrt{19} \times \sqrt{21})R36.6°$ reciprocal lattice. (c) Matching LEED pattern to the reciprocal lattice. (d) A unit cell of the reconstruction on top of $SiC(0001)$ plane.

Further annealing the $6H\text{-}SiC(0001)$ at 1100 °C in the silane/argon gas mixtures obtains a complex reconstruction as seen in the top left of the Fig. 3.12. Searching through the table 23.3 in the handbook [146], the pattern was possibly matched to the $(\sqrt{19} \times \sqrt{21})R36.6°$ reconstruction. The bottom right of the figure is the atomic model of the reconstruction. However, I have not found any low-index silicon plane

from silicon bulk matching to the structure.

When changing the growth temperatures and pressure of the silane/argon gas mixtures, there were some blurred and unknown reconstructions appeared which are not shown here. At the temperature range of 1000 °C-1100 °C, the silicon film thickness was almost unchanged under a given silicon overpressure based on AES signals, around $1.1 - 1.4$ML. Increasing temperature would result in more silicon evaporated than one deposited, thus making the surface more carbon rich. My experiment also confirmed a carbon-rich $(\sqrt{3} \times \sqrt{3})R30^\circ$ phase appeared at $\sim 1150\,^\circ$C and the $(6\sqrt{3} \times 6\sqrt{3})R30^\circ$ phase occurred at $\sim 1200\,^\circ$C.

3.2.2 Reconstructions on $SiC(000\bar{1})$ under silicon deposition

In this Section, I will show surface reconstructions on the C-face of the same sample while annealing under the silane/argon gas mixtures. It is worth to mention that the C-face was grown the same conditions with the Si-face because of our sample holder design. Based on the AES spectra, the thickness of the silicon films was close the same on both faces; however, the reconstructions were different. Apart from the beginning $(\sqrt{3} \times \sqrt{3})R30^\circ$ phase, there were (1×1), (3×3), and (2×2) phases shown up at different temperatures.

Figure 3.13 reveals the morphology of the C-face before and after graphitization. The starting surface, also treated using ex-situ hydrogen etching at 1400 °C, was atomically flat with regular straight steps (top figure). Between two big terraces were one smaller terrace. The existence of the small terraces was not the double-tip effect because of their width variations. The profile of the image on the right-hand side confirmed that between two big terraces were a unit-cell height step of 1.5 nm. The unit-cell height step included two half unit-cell height steps which were very close each other. The bottom figure is the morphology of the graphene on carbon face after graphitization at 1300 °C for 30 mins under silane/argon gas mixtures. Contrast

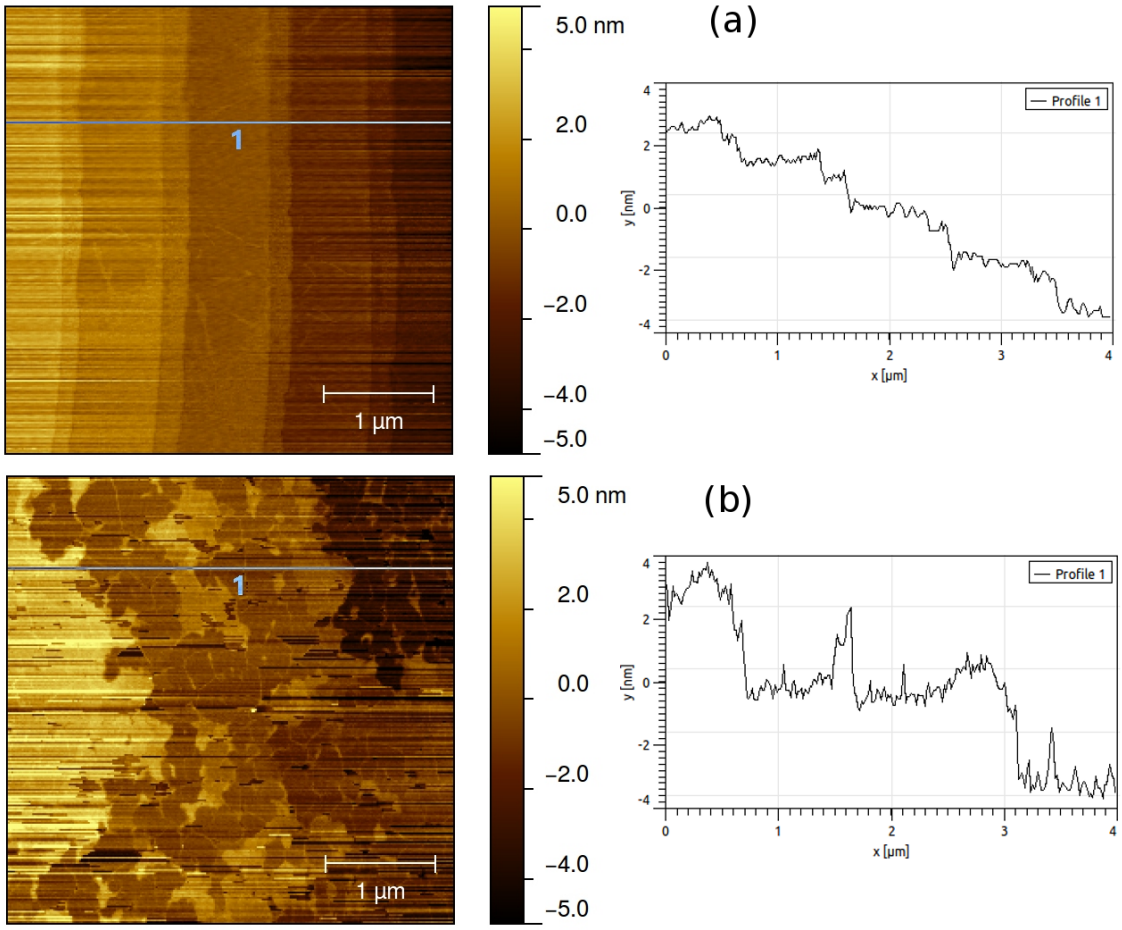

Figure 3.13: AFM images of the C-face: (a) The starting surface is atomically flat with regular straight steps. A unit-cell height step, $\sim 1.5\,\text{nm}$, includes two half-unit-cell height steps close to each other. (b) Morphology of the surface after graphitization. The step heights are two unit cells.

to the Si-face, the straight steps were disappeared on the C-face. On the terraces, the height of different regions varied because their heights were depended on the number of graphene on top. The line profile on the right reveals that the height of steps is approximately two unit cell heights, $\sim 3\,\text{nm}$.

The different reconstructions on the C-face at various conditions are summarized in the Fig. 3.14. After ex-situ hydrogen etching, the surface reconstruction was $(\sqrt{3} \times \sqrt{3})R30^\circ$ (not shown) which resulted from the silicate layer [144]. Contrast to the Si-face, the surface reconstruction remained unchanged while being annealed at 850 °C for 30 mins. It only transformed to (1×1) at higher temperature ($\sim 950\,^\circ\text{C}$).

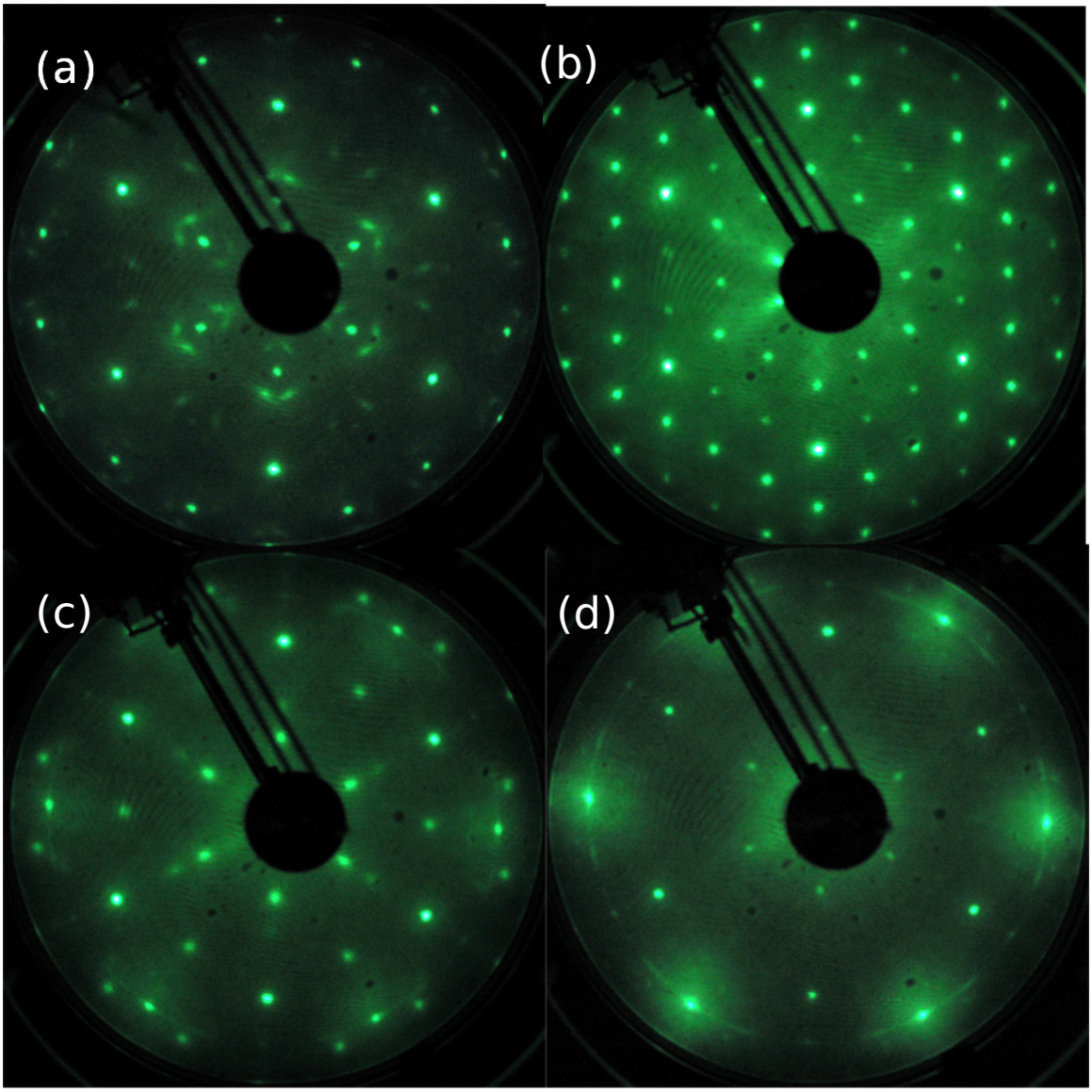

Figure 3.14: LEED patterns on the C-face at various temperatures. (a) (2×2) spots at 1000 °C and 1.4×10^{-4} Torr of silicon (75 eV). (b) (3×3) spots at 1100 °C and vacuum (72 eV). (c) (2×2) spots plus graphene ring at 1250 °C and 1.4×10^{-6} Torr of silicon (60 eV). (d) dimmer (2×2) spots and clear graphene ring when annealing in 1.4×10^{-5} Torr of silicon for additional 30 mins (60 eV).

Increasing the temperature to 1000 °C in silicon pressure of 1.4×10^{-4} Torr, the phase switched to (2×2) with additional unknown spots as shown in the top left of the figure. By keeping the silicon pressure unchanged and increasing the temperature to 1100 °C, the reconstruction remained (2×2). It only changed to (3×3) after being annealed at 1100 °C in vacuum for an hour (the top right of the figure). Then,

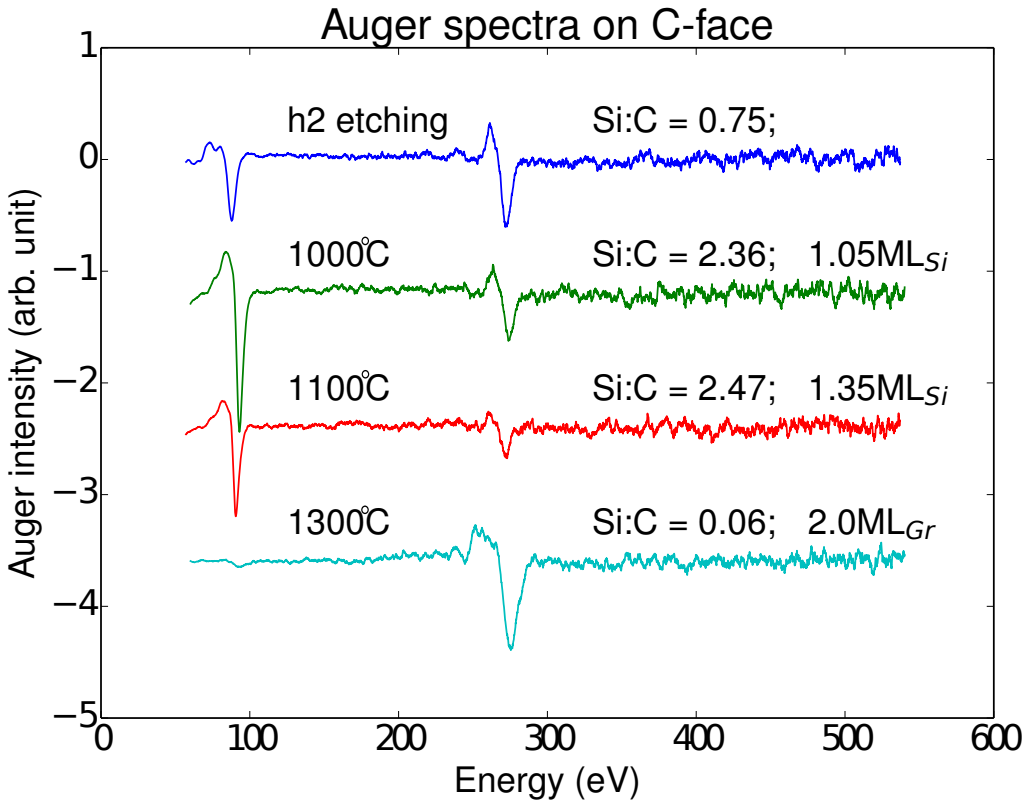

Figure 3.15: Auger spectra of the C-face after ex-situ hydrogen etching and annealing at different temperatures in the silane/argon gas mixtures. The Si:C ratios decrease as the annealed temperatures increase.

increasing temperature to 1250 °C in silicon pressure of 1.4×10^{-6} Torr, the reconstruction switched back to (2×2). However, there was a graphene ring appeared in the LEED patterns instead of unknown spots as shown previously at 1000 °C. When keeping the temperature the same, 1250 °C, and increasing the silicon pressure to 1.4×10^{-5} Torr, the (2×2) spots were dimmer, and the graphene ring was brighter as expected of more graphene grown as shown in the bottom left of the figure. In conclusion, there was only one stable reconstruction, (2×2), at the temperature range of 1000 °C-1200 °C under silicon overpressure.

Figure 3.15 shows the AES spectra of the C-face at various growth steps as in the Si-face (see Fig. 3.9). The starting surface had Si:C ratio of 0.75 which was similar to the ratio on the Si-face. The oxygen peak in this case was not as visible as that in the

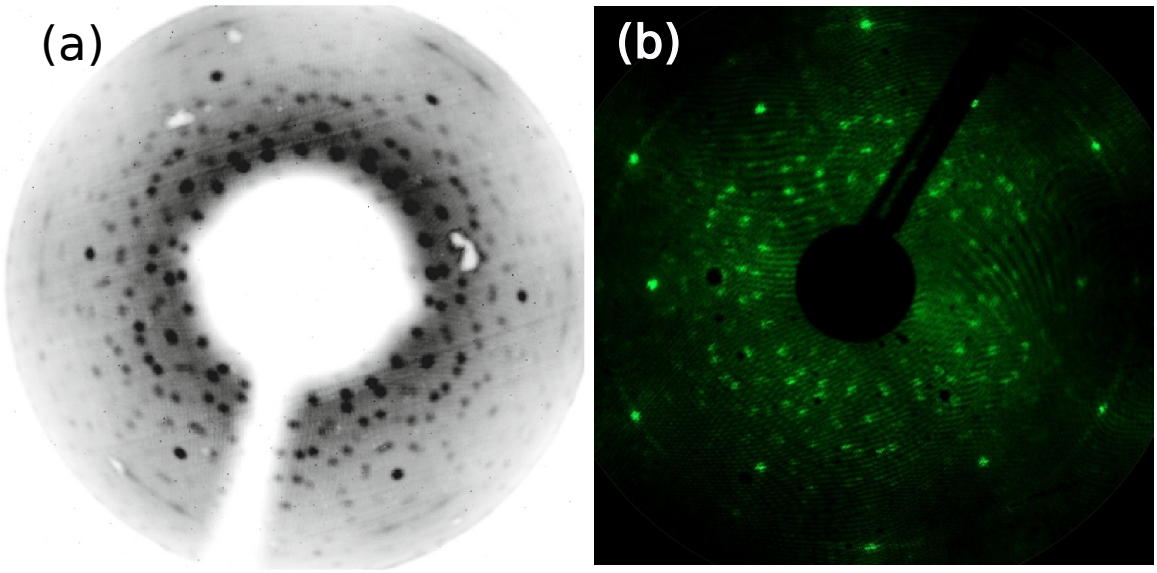

Figure 3.16: LEED patterns of the $(\sqrt{43}\times\sqrt{43})R7.6^\circ$ reconstruction: (a) The pattern on the C-face at 100 eV was reported recently [119]. The sample was prepared by heating in disilane (5×10^{-5} Torr) at 1220 °C for 10 min. (b) The pattern of the C-face surface is acquired at 60 eV. The sample was annealed inside our graphite under 2×10^{-4} Torr silane/argon gas mixtures at 1350 °C for 20 min.

Si-face because of the large background noises at high energies. The Si:C ratios are 2.36 and 2.47 at 1000 °C and 1100 °C respectively. Similar to the Si-face, the ratios almost insensitive in this temperature range. Based on the AES model, the thickness of the silicon films is slightly less than that in the Si-face case in that range, roughly 1.05-1.15ML compared to 1.1-1.4ML. Even though the background noises were large around 500 eV in these case, it was reasonable to conclude that there were no traces of the oxygen peaks. At 1300 °C, the Si:C ratio was relatively small, 0.06, which is corresponding to 2ML of graphene based on the AAM model.

To complete the chapter, I would like to discuss the $(\sqrt{43}\times\sqrt{43})R7.6^\circ$ reconstruction on the C-face. As discussed in Ref. [119], the symmetric structure was found to form between graphene and the underlying the C-face of the SiC substrate. Thus, this interface layer is analogous to the $(6\sqrt{3}\times 6\sqrt{3})R30^\circ$ buffer layer that forms on the Si-face. In Ref. [119], the reconstruction was established under either disilane or purified neon (without oxygen contamination). The specific conditions were disilane

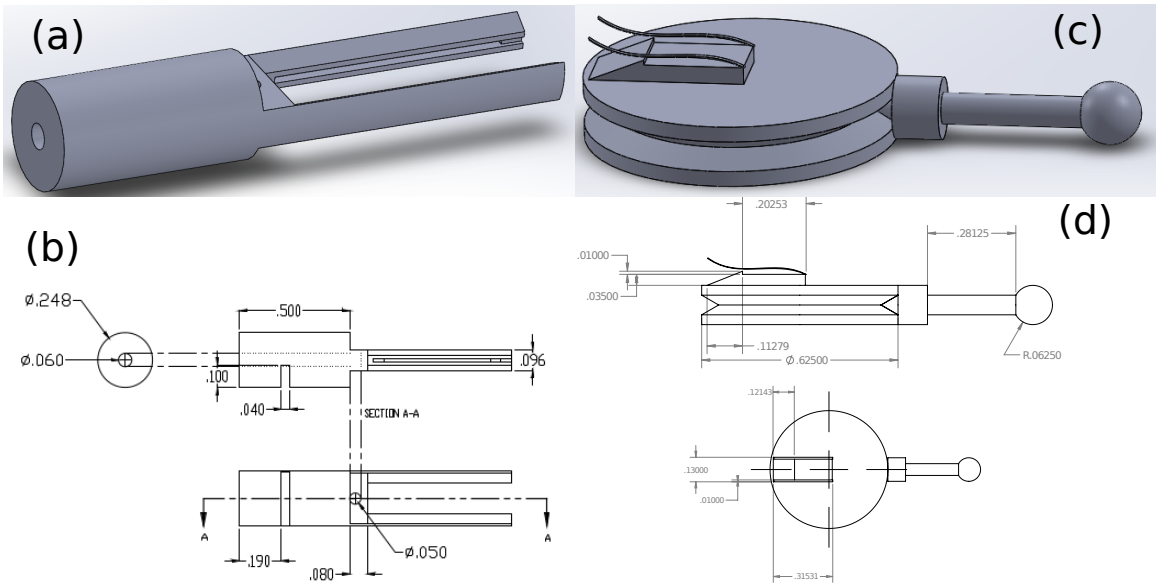

Figure 3.17: Design of the holders: (a) Vented graphite sample holder of the growth system. (b) Dimensions of the graphite holder in inches. (c) Modified sample holder of the RT STM system. (d) Dimensions of the STM holder.

pressure of 5×10^{-5} Torr, heating temperature of 1220 °C, and growth time of 10 min. In our graphite furnace, the $(\sqrt{43} \times \sqrt{43})R7.6°$ reconstruction on the C-face was achieved at slightly different conditions. The sample was annealed in 2×10^{-4} Torr silane/argon gas mixtures (corresponding to 1.4×10^{-6} Torr of silicon) at 1350 °C for 20 min.

For further investigating the properties of the $(\sqrt{43} \times \sqrt{43})R7.6°$ interface layer, it is necessary to use other surface science techniques. As available in our lab, the STM is suitable for studying the atomic structures of the reconstruction. However, if the sample is taken out to transfer to the STM system, the oxidation will destroy the interface layer. To overcome these obstacles, I created a vacuum suitcase which allowed transferring this sample to our STM system in the vacuum environment. Figure 3.17 is the design of the vented graphite sample holder used in the growth system and the modified sample holder used in the RT STM system. The vented holder had a small hole (0.06 inch of diameter) which assisted the silane gas to infiltrate inside the enclosed graphite furnace. On top of the STM holder, I introduced a holder stage

with two bending wires on the sides and a little stopper (the height of 0.01 inch) at the end to trap the sample inside. While transferring, the two sample holders were in alignment. Then the graphite sample holder (with a sample inserted inside it) was pushed forward slowly until the sample was entirely trapped inside the holder stage. The stopper would prevent the sample moving out when the graphite sample was withdrawn. After trapped the sample into the holder stage, the whole things were enclosed inside a small chamber and transferred to the STM system without exposing to air.

3.3 Chapter Conclusion

In this chapter, I successfully developed the Auger Attenuation Model (AAM) for the CMA data to determine the film thickness. The Auger intensity was derived from the material density, backscattering factor, effective attenuation length. These parameters could be reliably obtained using NIST software. This model was specifically applied for determining the silicon/graphene film thickness which epitaxially grown on top of a SiC substrate. The calculation was taken into account the different between the Si-terminated face and the C-terminated face of the substrate. Finally, I established a routine to convert the RFA data (which were collected from the in-situ LEED/Auger system) to the CMA data before exercising the AAM.

When studying the silicon deposition on top of the SiC wafer in silane/argon gas mixtures, I found interesting reconstructions on both faces. On the Si-face, LEED patterns revealed new reconstructions which have not reported elsewhere such as: $(\sqrt{3}\times 7)R30°$, $(2\sqrt{3}\times\sqrt{13})R30°$, $(\sqrt{19}\times\sqrt{21})R36.6°$. These patterns were formed at the temperature ranges of 1000 °C-1100 °C. On the other hand, LEED patterns on the C-face only showed the familiar phases of $(1\times)$, (2×2), (3×3). Moreover, I also achieved the $(\sqrt{43}\times\sqrt{43})R7.6°$ reconstruction on the C-face in silane gas. The results confirmed the reliability of our growth system to obtain high-quality film without any

contaminations (no oxygen present). For further study, I designed the vacuum box to transfer the samples after grown to the STM system in vacuum condition.

CHAPTER IV

EPITAXIAL GRAPHENE GROWTH ON VICINAL SILICON CARBIDE

In this chapter, I focus on studying the epitaxial graphene growth on the Si-face of a SiC dimple sample. A dimple geography provided various vicinal angles from an on-axis SiC wafer. While the dimple was anneal under silane/argon gas, larger vicinal angles caused to form natural step bunches and nano-facets which were important to study the formation of the sidewall graphene nanoribbons. The Si-face was chosen because of the ability to control a desirable number of graphene layers with appropriate growth conditions. The dimple sample was annealed inside the graphite furnace while flowing silane/argon gas mixtures through the growth chamber (silane percentage of 0.7%). The silane/argon gas would maintain higher silicon overpressure to suppress the silicon sublimation rate further. The growth setup was expected to yield high-quality graphene in the thermodynamic quasi-equilibrium process.

The first section, Sec. 4.1, is devoted to present the dimple experimental results. The starting surface of the dimple after hydrogen etching was uniform unit-cell or half unit-cell height steps. After the graphitization in silane/argon, the step bunching occurred and depended on the vicinal angles. The bigger the local angles were, the higher the bunching steps became. In the next section, a quasi-one-dimensional step bunching model was developed to explain the experimental results theoretically. The simulation outcomes of the model fitted well with the experiments. In the last section, the possibility of forming graphene in vicinal angles is discussed in comparison to existing models [147–150]. The results provide more understanding about the mechanism of epitaxial graphene growth on vicinal silicon carbide.

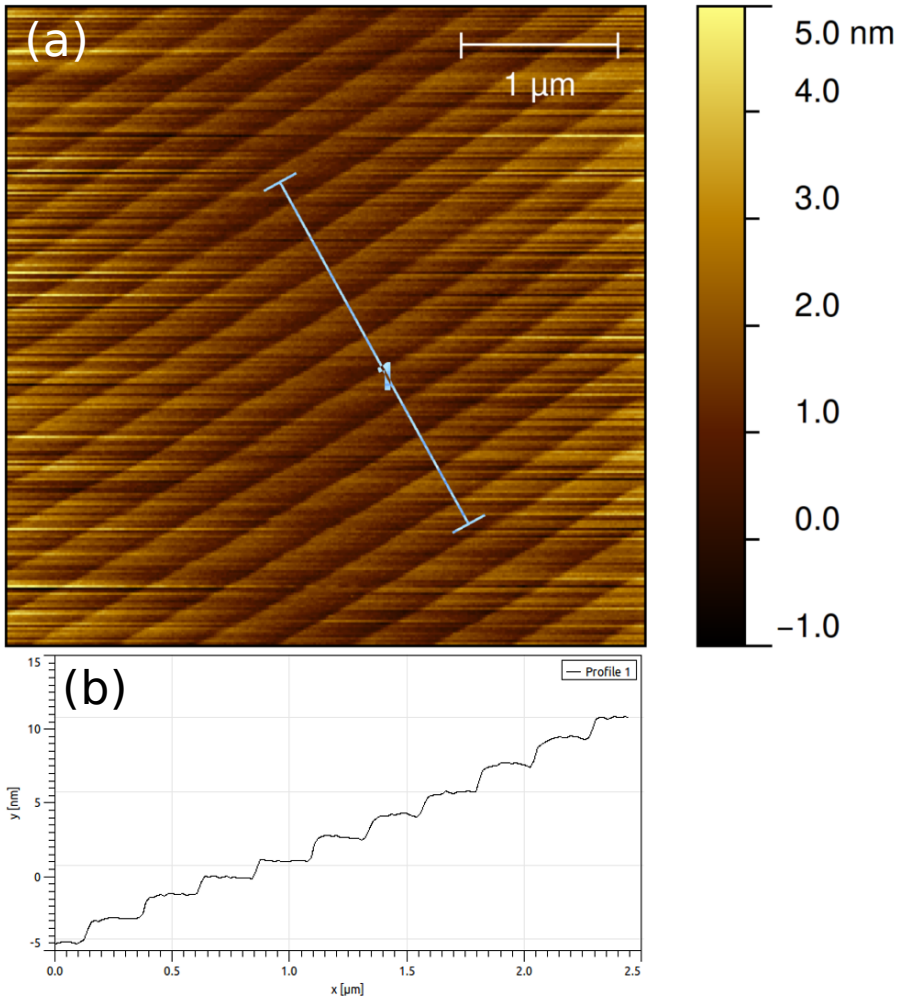

Figure 4.1: A $4 \times 4\,\mu\text{m}^2$ AFM image of the dimple sample after hydrogen etching which is taken near the center of the dimple: (a) graphic image (mean plane subtracted) reveals the equidistant, straight steps. (b) the line profile of the segment on the top figure after applying facet level. It confirms the average step height of a unit-cell of $6H$-SiC, 1.5 nm.

4.1 Experimental Results

4.1.1 Dimple sample preparation

A dimple sample was prepared on the Si-face of a $6H$-SiC wafer by using dimple grinder as described in the Sec. 2.1. After the grinding process, the dimple had a depth of $30\,\mu\text{m}$ as shown in the Fig. 2.3. The dimple sample was treated using hydrogen etching to remove all the deep scratches on the surface (see Sec. 2.1.2). Then, the AFM was used to confirm the atomically flat surface with regular steps on

Figure 4.2: A $10 \times 7.5\,\mu m^2$ SEM image of the dimple sample after hydrogen etching taken near the center of the dimple. The scan is captured at primary electron energy of 3 kV, working distance of 8 mm, and aperture size of 30 μm.

it. The density of these steps depended on the vicinal angles as shown in the Fig. 2.6. The AFM image of the typical region near the center of the dimple is presented in Fig. 4.1. In this image, the data is leveled by adding a plane to mark the terrace flat using Gwyddion software. The line profile (averaging of 15 pixels) at the bottom of the image reveals that these steps are a unit-cell height of 1.5 nm. The average terrace size is about 250 nm which is corresponding to the vicinal angle of 0.35°.

Figure 4.2 shows an SEM image of the dimple sample after hydrogen etching. The scan position is also near the center of the dimple. As also seen in this figure, the surface consists of regular, straight steps. The average terrace size of about 300 nm is close to the results from AFM images.

4.1.2 Dimple sample morphology after graphitization

The dimple sample was inserted into a graphite holder and transferred into the UHV system as discussed previously (Sec. 2.2.1). The growth process of the dimple sample

included three temperature steps of 850 °, 1100 °, and 1250 ° consecutively. The temperature of the furnace was monitored by the infrared pyrometer with the emissivity set to 88% (see Sec. 2.2.2 for temperature calibration). The soak time at each temperature step was equal to 20 min while the ramping time between two temperatures was only 30 sec. The whole process was controlled by the in-house python program named pyTherm.py (see Dr. Miller's thesis for more details [90]). During the annealing procedure, the 0.7% silane/argon gas mixtures continuously flowed through the growth chamber. The gas pressure was initially at 2×10^{-4} Torr, then it was stable at 2×10^{-3} Torr during the graphitization step of 1250 ° (corresponding to the silicon overpressure of 1.4×10^{-5} Torr). The pressure was measured by a convection gauge at that pressure range [91]. After the graphitization, the graphite furnace was cooled down to room temperature quickly by shutting off the RF heater. When the silane/argon gas was stopped flowing, the turbopump was turned on to pump the growth chamber. Until the pressure of the growth chamber reached to 1×10^{-8} Torr, the vacuum valve was opened to transfer the sample to the main chamber for in-situ LEED/Auger characterization.

As usual, the sample was firstly characterized by LEED because this technique is operated at lower primary electron energy ($50 - 200$ eV) than the Auger mode (2.5 keV). The LEED patterns inside the dimple and on the flat region were almost identical, perhaps because the size of the primary electron beam was comparable to the dimple diameter. The LEED pattern at 60 eV showed both the graphene and the $(6\sqrt{3} \times 6\sqrt{3})R30°$ reconstruction spots as shown in the Fig. 4.3. Based on the sharpness of these spots, the surface was well-ordered. After that, the equipment was switched to the Auger mode to measure the Auger spectra of the sample. Again, because of the large beam size, the Auger data only provided the average coverage of the graphene inside the dimple. The shape of the C-peak and the Si:C Auger intensity ratio affirmed the existence of epitaxial graphene on the surface [145]. Based on the

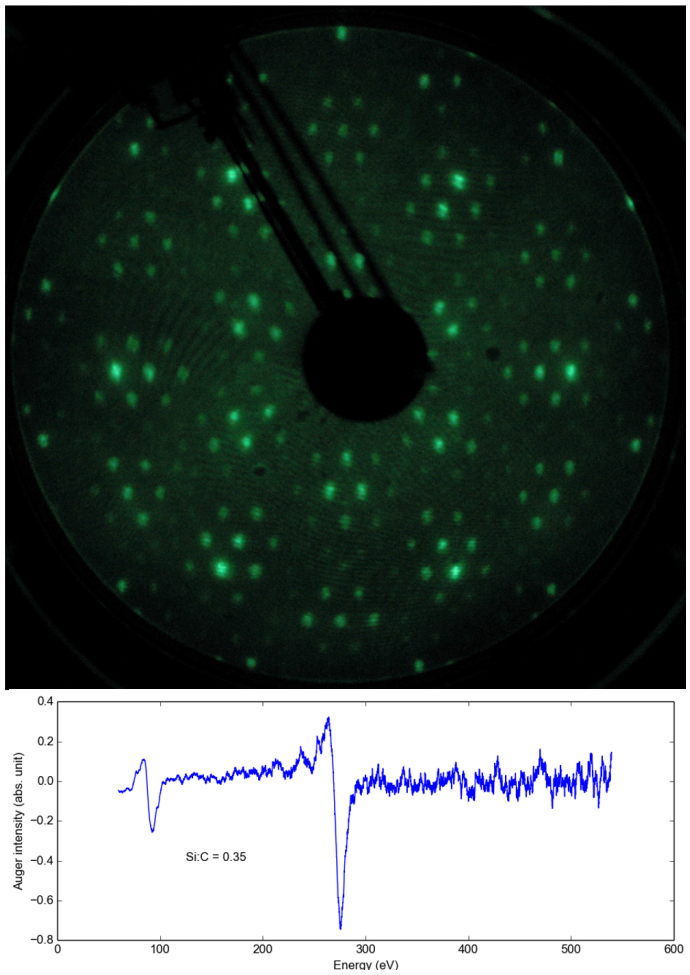

Figure 4.3: In-situ characterization of the dimple sample after graphitization: (top) LEED pattern shows the graphene and the $(6\sqrt{3}\times 6\sqrt{3})R30°$ reconstruction at 60 eV. (bottom) Auger spectrum has Si:C ratio of 0.36. Based on the AAM model, the graphene coverage is one graphene layer.

AAM model from Sec. 3.1.6, the Si:C ratio of 0.36 was corresponding to one graphene layer.

The dimple sample was then transferred out for further investigation using SEM, AFM, and STM. Figure 4.4 shows the morphology of the dimple obtained by SEM. The $5\times 5\,\mu\text{m}^2$ scans were taken at various locations inside the dimple. Due to different work functions of secondary electrons emitted from the surface, SEM distinguishes regions according to different contrasts [108, 151]. In this figure, the bright regions were covered by the $(6\sqrt{3}\times 6\sqrt{3})R30°$ buffer layer while the dark regions were covered

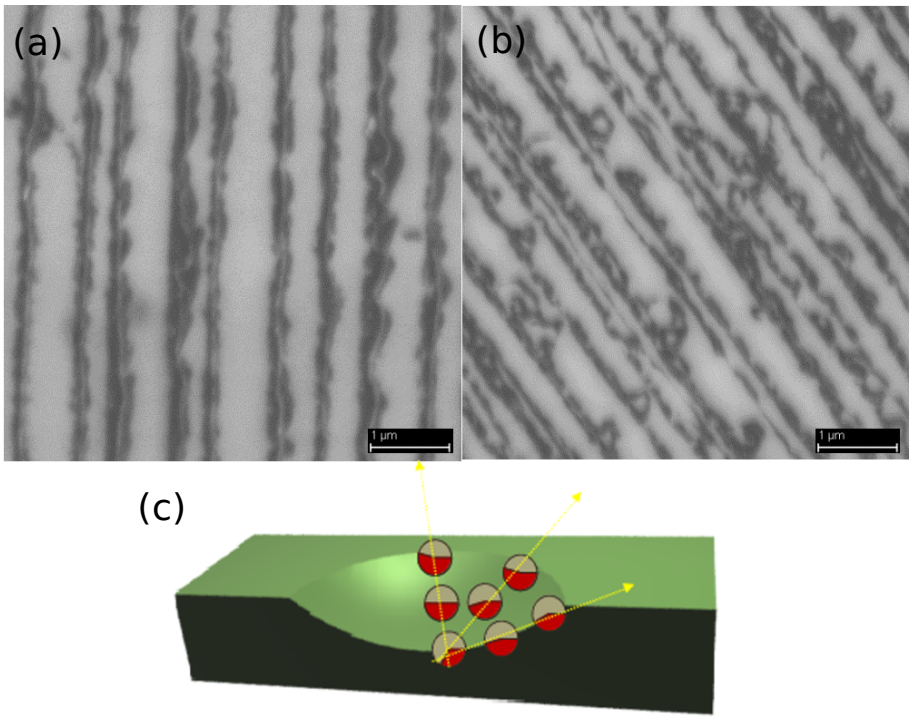

Figure 4.4: SEM images taken at various locations inside the dimple sample after graphitization, (a) and (b). The white regions are buffer layers while the dark regions are graphene layers. (c) The average graphene coverage at different locations. The larger the vicinal angle, the higher the graphene coverage. Scan parameters are 3 kV primary electron energy, 8 mm working distance, and 30 μm aperture size.

by graphene. Overall, the surface still included multiple parallel steps though the terrace widths were uneven. The dark regions appeared along the steps which also implied that the growth of graphene started at step edges. The step edges were not as straight as they appeared before graphitization. The average graphene coverage was calculated by the ratio of the dark area to the total area. The calculations from different locations revealed that graphene regions were broadened with increasing vicinal angles. The average graphene coverage inside the dimple was about 0.46ML which was close to the Auger estimation.

Figure 4.5 is a $10 \times 10\,\mu m^2$ AFM image of a typical region inside the dimple. The topography of the surface demonstrated an array of parallel steps. However, the widths of those terraces varied significantly which agreed with the SEM results. The line profile, which was taken perpendicular to the step edges, is shown in the bottom

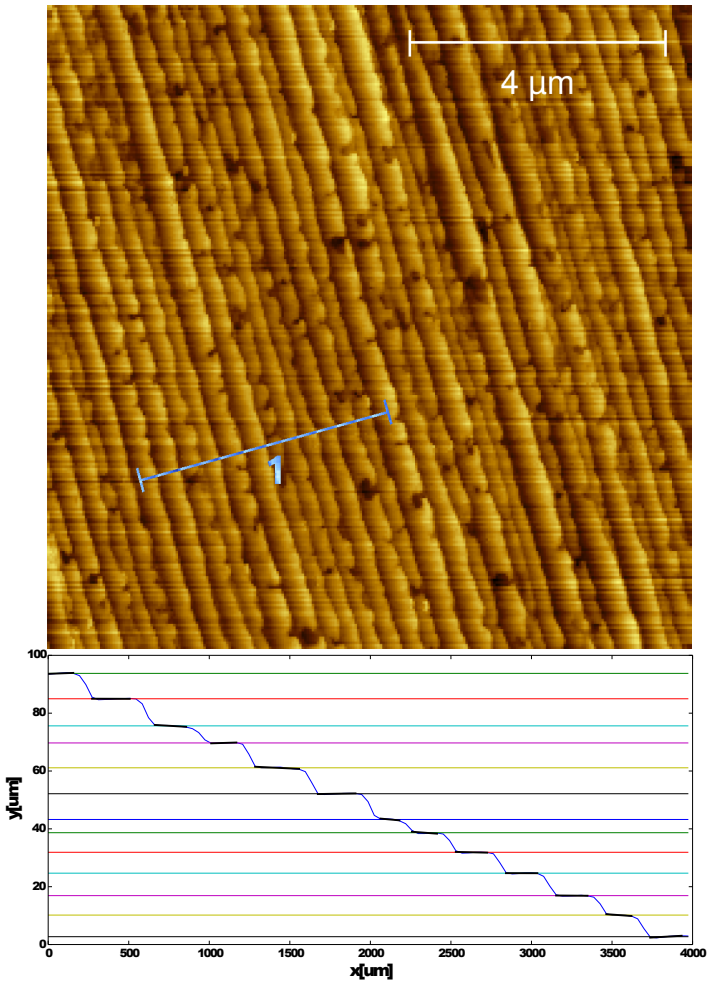

Figure 4.5: A $10 \times 10\,\mu\text{m}^2$ AFM image the dimple sample on silicon face after graphitization. (left) Topography of the surface after removing quadratic backgrounds. (right) The line profile of the in the top figure after applying the facet level data. The horizontal lines are the terraces, identified by their shape after background subtraction.

of the Fig. 4.5 after applying the facet level data. By using Gwyddion software, this tool levels data by subtracting a plane to make facets of the surface as horizontal as possible. The profile is reasonable to interpret the average bunch size as well as the vicinal angle at this typical position. Quantitatively, the step heights, which are interpreted from the image, are bigger than a unit-cell height of the regular steps of the starting surface. To increase the accuracy, the procedures were repeated for different profiles (10 profiles at each location in the dimple), then the average value and standard deviation were taken from the acquired data. The summary of the

Table 3: Calculation the average bunch size N_{av} (nm) versus local angle α (degree) from AFM images at different locations inside the dimple. See text for explanation of estimation methods.

Region	Scan ID	N_{av} (nm)	α $(^\circ)$
1	0309013c	2.60 ± 0.36	0.25
2	03090140	5.45 ± 0.42	0.75
3	03090144	7.16 ± 0.20	1.35
4	0309014a	10.52 ± 0.13	2.88
5	03090154	2.90 ± 0.11	0.31
6	03090152	3.87 ± 0.33	0.44
7	03090156	8.98 ± 0.24	1.84

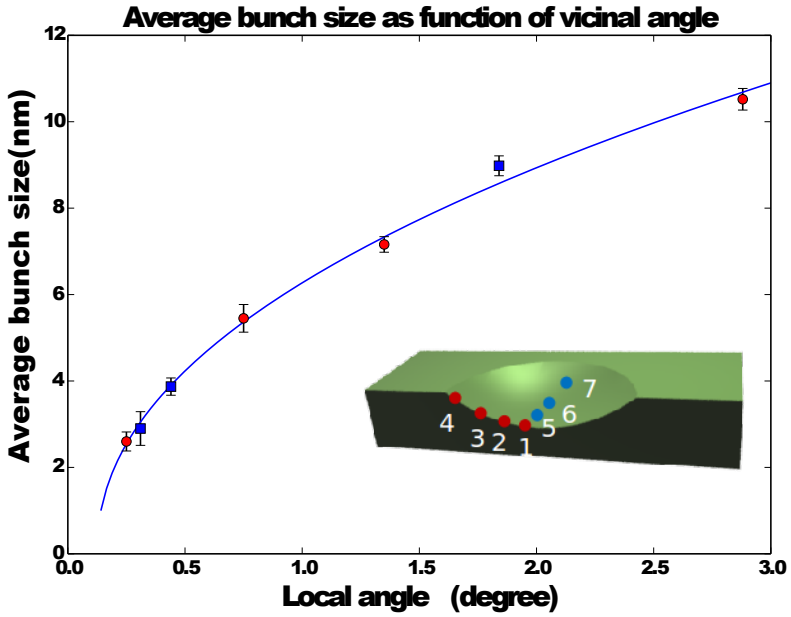

Figure 4.6: Average step heights at various local angles as suggested in the Table 3. The data are fitted to the power law relation, $a(x - x_0)^b$. The curve fit function provides the value of the parameters: $a = 6.08 \pm 0.14$, $b = 0.47 \pm 0.05$, and $x_0 = 0.12 \pm 0.05$. Inset: The approximate locations of the AFM images inside the dimple.

results at different locations is presented on the table 3.

The average bunch sizes at various local angles are visualized in the Fig. 4.6. The approximate locations of the AFM images are presented in the inset. As shown in the figure, the larger the vicinal angle, the bigger the bunch height. Moreover, the average bunch height is relatively insensitive to the direction of the steps. The

relationship between average bunch size and vicinal angles is held at various locations inside the dimple. The data are fitted to a power law relation $a(x - x_0)^b$ using the curve fit function (the Scipy package in Python). The results are: $a = 6.08 \pm 0.14$, $b = 0.47 \pm 0.05$, and $x_0 = 0.12 \pm 0.05$. The power law relation ($b \approx 1/2$) of the average bunch sizes as a function of vicinal angles will be explained by running the simulation of a step bunching model in the next Section.

The STM study of a different dimple sample (sample ID: HDS009), which was expected to be similar nanoribbon structures, indicated the analogous step bunching formations. The details of STM results on sidewall graphene nanoribbons were presented in Chapter 3 of Dr. Yuntao Li's thesis [103]. Figure 4.7 shows the topology of a typical sidewall facet on the dimple. A large scan ($5 \times 5\,\mu\text{m}^2$) displays the overall step structure of a large step bunch (Fig. 4.7). A zooming-in scans ((b) and (c)) confirm the presence of graphene lattices on both the terrace and near the step edge. Compared to the undistorted graphene lattices on the flat terraces, the graphene lattices near the step edge are stretched, sheared, and rotated about $10\,^\circ$. The line profile of the step bunch (Fig. 4.7c) demonstrates the step height of 11 nm which is corresponding to the facet angle of $22.3\,^\circ$. The results from Dr. Li's thesis show that the sidewall is the $(11\bar{2}\ 16)$ facet with approximately the zigzag-edge orientation.

The results of the experiment raise two issues needed to be resolved: (i) the evolution of step bunching, (ii) the formation of graphene at the step edges. In the next section, a quasi-one-dimensional step model is developed to solve the former issue. The simulation results confirmed the power law relation of the average bunch size and the vicinal angle. The latter issue has not been well understood yet and will be discussed in Sec. 4.3.

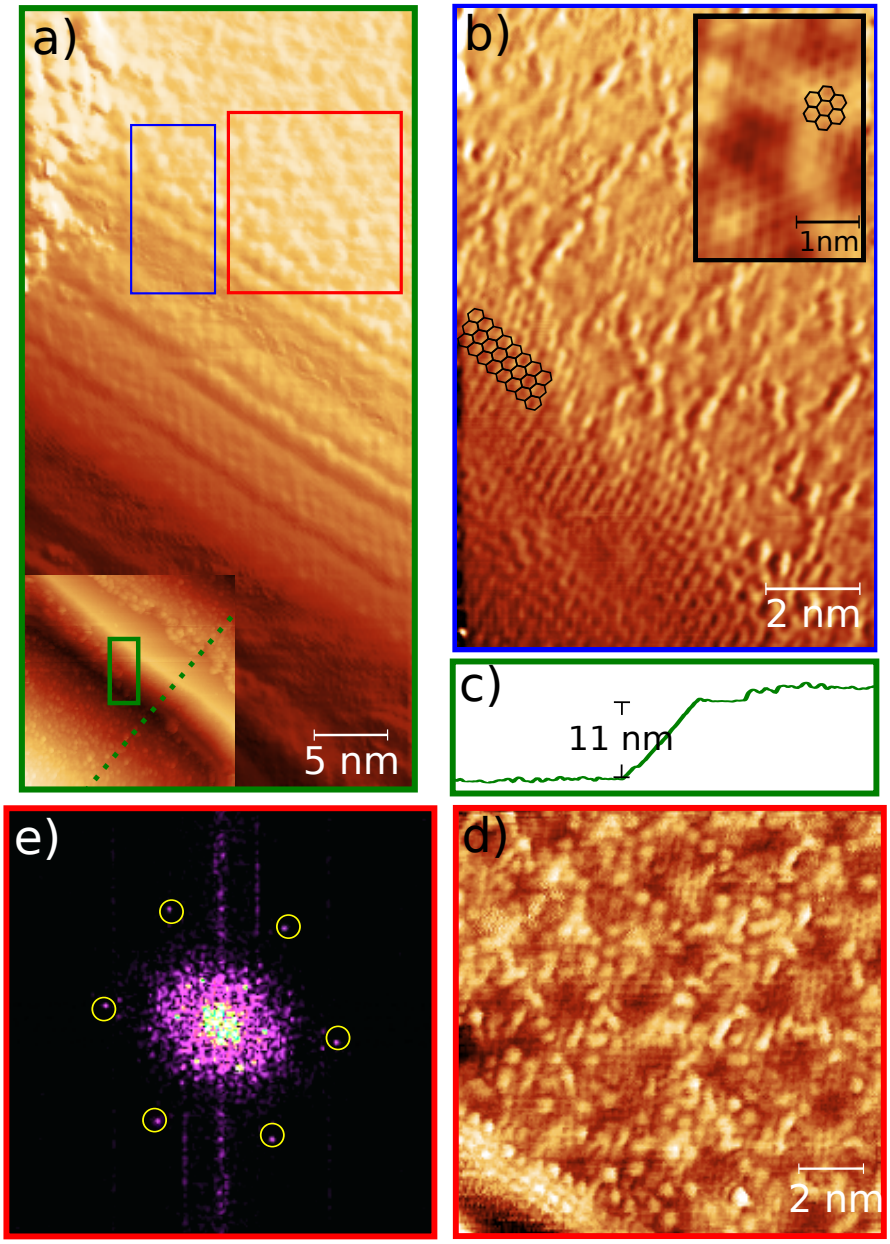

Figure 4.7: STM image of a typical sidewall facet on the dimple. (a) The overall step structure of a large step bunch shown in the inset. (b) Atomic resolutions of a region near the step edge with distorted graphene lattices. The inset shows the undistorted graphene lattices on the flat terrace farther way from the step edge. (c) Line profile of the dashed green line in the inset of (a) reveals the step height of 11 nm and facet angle of 22.3°. (d) Undistorted graphene lattices of the top terrace in (a). (e) FFT of (d) showing the $(1 \times 1)_{Gr}$ periods ($\sim$ 2.34 Å). Images are acquired at sample biases of -0.6 V (a), -1.0 V (b), and -0.6 V (e) while tunneling current sets at 30 pA. Copyright ©2016 by Yuntao Li. Reprinted with permission [103].

4.2 SiC step bunching: a quasi one dimensional step model

The formation of step bunches at a vicinal surface has been an interesting topic in surface science for a long time. Step bunching is an essential case of surface self-organization when the system is out of equilibrium states. The mechanism of the stepping behavior is also crucial for comprehensive understanding the step-flow growth mode. This mode is widely used for epitaxial growth of thin film in technology nowadays. Recently, SiC step bunching is a problem of interest because of the outstanding properties of the SiC material. Step bunching of the SiC surface has different heights and edges formed in various conditions. The possible source of surface instabilities includes geometrical, energetic and kinetic origins. For the geometrical origin, the step morphology and bunching depend on the crystallographic structures and step directions. For example, after hydrogen etching the steps of the $6H$-SiC are straight or zigzag shapes, unit-cell or half unit-cell heights corresponding to the surface tilted toward $[1\bar{1}00]$ or $[11\bar{2}0]$ respectively [152]. For the energetic and kinetic origins, the step bunching mechanisms include strain effects [153], surface electromigration [154, 155], and an asymmetric attachment/detachment known as Ehrlich-Schwoebel (ES) effect [156–158]. In our dimple graphitization experiments, the primary source of step bunching is the ES effect because of no external electromagnetic field. In this effect, the probabilities of incorporating of adatoms from the upper and lower terraces to the step are uneven because of the asymmetrical energy barriers between two sides of the steps.

4.2.1 Theory of Step Bunching

In this section, I will derive the analytic expressions of the step velocity. For the SiC system, I will choose a simplified model which ignores graphene growth and presumes that SiC step bunching is a consequence of etching via the desorption of Si atoms from the crystal. A conventional model of thin-film growth can be applied, with zero

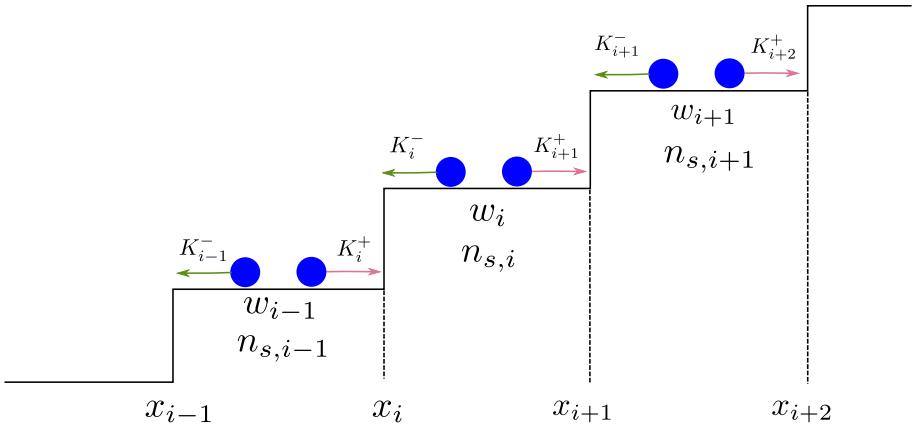

Figure 4.8: Schematic step configuration of a vicinal suface in one dimension. The position of the ith step is x_i. $n_{s,i}$ is the concentration of adatoms on the ith terrace, its width $w_i = x_{i+1} - x_i$. The kinetic coefficients for the ascending and descending step i are K_i^+ and K_i^- respectively.

incident atom flux. The model is generalized from the original Burton-Cabrera-Frank (BCF) model in the presence of ES barriers. It is considered in the regime of: (i) the attachment/detachment limitation, and (ii) local mass transport [159]. In that regime, the step motion is limited by the attachment/detachment rate of adatoms to step edges (in contrast to being limited by the diffusion rate on terraces). The local mass transport means that only atoms from two bounding terraces can hop to the steps (no significant hopping of adatoms over the steps). In this situation, an adatom detaching from the step can diffuse on the terrace and then attach to nearby steps without moving out of the surface.

We consider a vicinal surface with an array of discrete steps in quasi-one dimension as labeling in Fig. 4.8. The processes of atom migration on the surface are generally described by the stationary diffusion equation [160]:

$$D_s \frac{d^2 n_s}{dx^2} - \frac{n_s}{\tau_s} + R = 0, \tag{4.1}$$

where D_s is the coefficient of surface diffusion, n_s is the concentration of adatoms (adatom density) on the surface, R is the deposition rate of adatoms to the surface, τ_s is the lifetime of an atom in a state of mobile adsorption, and x is the horizontal

coordinate perpendicular to the step edges.

In the attachment/detachment limited regime, the rate of an adatom attaching to or detaching from a step is much smaller than the rate of diffusion on terraces. Thus, the step motion on the surface reduces to the diffusion problem at a single terrace. Considering the terrace i between two steps i and $i+1$, the boundary conditions are determined by the surface fluxes of adatoms at the descending step and the ascending step [161]:

$$\begin{aligned} -D_s \frac{dn_{s,i}}{dx}\Big|_{x=x_i} &= -K_i^-[n_{s,i}(x_i) - n_s^e(x_i)], \\ -D_s \frac{dn_{s,i}}{dx}\Big|_{x=x_{i+1}} &= K_{i+1}^+[n_{s,i}(x_{i+1}) - n_s^e(x_{i+1})], \end{aligned} \tag{4.2}$$

where K_i^- and K_{i+1}^+ are the kinetic coefficients for the ascending and the descending steps i and $i+1$ respectively, $n_{s,i}(x)$ is the adatom concentration on the terrace between the ith and $i+1th$ steps, and $n_s^e(x_i)$ is the equilibrium value of the adatom concentration in the vicinity of the step i. The value of n_s^e at the ith step depends on the chemical potential at that step in an exponential law as $n_s^e(x_i) = n_s^e \exp[\mu_i/k_BT]$. In which, μ_i is the atom chemical potential at the step i, defined as the increase/decrease in free energy of the system when an adatom attaches/detaches to the step. For a $1D$ step configuration with elastic and entropic step repulsions, the step chemical potential can be written as [162]

$$\mu_i = 2\Omega g h^3 \left(\frac{1}{w_{i-1}^3} - \frac{1}{w_i^3}\right), \tag{4.3}$$

where $\Omega = a_\perp a_\parallel$ is the atomic area, $a_\perp$ and $a_\parallel$ are the interatomic distances perpendicular and parallel to the steps respectively, h is the step height, and $w_i = x_{i+1} - x_i$ is the width of terrace i. The parameter g is the step-interaction coefficient which is the coefficient of the s^3 term in the Gruber-Mullins form [163] for the free energy of vicinal surfaces with slope s.

The steady-state velocity of the step can be determined by the mass conservation

[164]:

$$v_i = \frac{dx_i}{dt} = \Omega \left(\frac{dn_{s,i-1}}{dx} \Big|_{x=x_i} + \frac{dn_{s,i}}{dx} \Big|_{x=x_i} \right) = v_- + v_+, \tag{4.4}$$

From the Eq. 4.4, there are two terms of the step-flow velocity corresponding to two contributions from both bounding terraces, the terrace in front of the step and the terrace behind the step. The Ehrlich-Schwoebel effect introduces the asymmetric barrier energies of the upward step edge (K^+) and downward step edge (K^-). It leads to the inequality of two velocity terms which allows the step bunching induced. Assuming that the step kinetic coefficients can be expressed in the exponential form $K_i^{\pm} = K_0 \exp(-E_i^{\pm}/k_B T)$, where $\Delta E_i = E_i^- - E_i^+$ characterizes the asymmetric barrier energies as discussed above. The ratio $\beta_i = K_i^-/K_i^+ = \exp(-\Delta E_i/k_B T)$ is an important parameter to control the step bunching process. It is called the normal ES effect if $\beta_i > 1$ or inverse ES effect if otherwise. The diffusion equation Eq. (4.1) is a second-order differential equation which has a general solution in the form:

$$n_{s,i}(x) = R\tau_s - A_i \cosh(x/\lambda_s) - B_i \sinh(x/\lambda_s), \tag{4.5}$$

where $\lambda_s = \sqrt{\tau_s D_s}$ is the surface diffusion length of adatoms. Substituting this solution to the boundary condition Eq. (4.2), the integration constants, A and B, can be determined after lengthy calculations:

$$\begin{aligned} A_i =& (R\tau_e - n_s^e(x_i)) \frac{K_i^- K_{i+1}^+ [\sinh(\frac{x_{i+1}}{\lambda_s}) - \sinh(\frac{x_i}{\lambda_s})] + \frac{D_s}{\lambda_s}[K_i^- \cosh(\frac{x_{i+1}}{\lambda_s}) + K_{i+1}^+ \cosh(\frac{x_i}{\lambda_s})]}{[K_i^- K_{i+1}^+ + (\frac{D_s}{\lambda_s})^2] \sinh(\frac{x_i}{\lambda_s}) + \frac{D_s}{\lambda_s}(K_i^- + K_{i+1}^+) \cosh(\frac{x_i}{\lambda_s})} \\ B_i =& (R\tau_e - n_s^e(x_i)) \frac{K_i^- K_{i+1}^+ [\cosh(\frac{x_i}{\lambda_s}) - \cosh(\frac{x_{i+1}}{\lambda_s})] - \frac{D_s}{\lambda_s}[K_i^- \sinh(\frac{x_{i+1}}{\lambda_s}) + K_{i+1}^+ \sinh(\frac{x_i}{\lambda_s})]}{[K_i^- K_{i+1}^+ + (\frac{D_s}{\lambda_s})^2] \sinh(\frac{x_i}{\lambda_s}) + \frac{D_s}{\lambda_s}(K_i^- + K_{i+1}^+) \cosh(\frac{x_i}{\lambda_s})} \end{aligned} \tag{4.6}$$

By substituting this expressions to the general solution in the Eq. 4.5, the concentrations of adatoms on each terraces are fully calculated. Then it is trivial to get the step velocity based on the Eq. 4.4. However, it is worth to make some assumption to simplify the analytic expressions. In our case at graphitization temperature, the carbon rich surface suggests that the absence of net silicon deposition, $R = 0$. Moreover,

the silicon desorption rate is suppressed by silane/argon gas mixtures, thus leading to the long diffusion length, $\lambda_s = \sqrt{D_s \tau_s} \gg w_i$. In that sense, we can approximate the hyperbolic functions: $\sinh(\frac{x}{\lambda}) \approx \frac{x}{\lambda}$ and $\cosh(\frac{x}{\lambda}) \approx 1 + \frac{x^2}{2\lambda^2}$. The last assumption is that the asymmetric effects are the same for each steps, i.e. $K_i^+ = K^+, K_i^- = K^-$ for all i. In this case we introduce the kinetic lengths $d_+ = D_s/K^+$ and $d_- = D_s/K^- = d_+/\beta$. Thus, the velocity of the *ith* step can be written in sum of two terms (Eq. 4.4) which are the functions of the widths of the terrace in front of the step and behind the step, v_- and v_+ respectively.

$$\begin{aligned} v_- &= \left(\frac{D_s \Omega n_s^e}{\lambda_s}\right) \frac{\frac{\beta}{k_B T}[\mu_i - \mu_{i+1}] + \frac{\beta d_+}{\lambda_s}(\frac{w_i}{\lambda_s}) + \beta(\frac{w_i}{\lambda_s})^2}{\frac{d_+}{\lambda_s}(1+\beta) + [\beta + (\frac{d_+}{\lambda_s})^2](\frac{w_i}{\lambda_s})} \\ v_+ &= \left(\frac{D_s \Omega n_s^e}{\lambda_s}\right) \frac{\frac{\beta}{k_B T}[\mu_i - \mu_{i-1}] + \frac{d_+}{\lambda_s}(\frac{w_{i-1}}{\lambda_s}) + \beta(\frac{w_{i-1}}{\lambda_s})^2}{\frac{d_+}{\lambda_s}(1+\beta) + [\beta + (\frac{d_+}{\lambda_s})^2](\frac{w_{i-1}}{\lambda_s})} \end{aligned} \tag{4.7}$$

Looking further to simplify the denominators of the velocities formula in Eq. (4.7), we consider two limiting cases:

$$\begin{aligned} (a) \quad & \frac{d_+}{\lambda_s}(1+\beta) \ll [\beta + (\frac{d_+}{\lambda_s})^2] \left(\frac{w_i}{\lambda_s}\right) \\ (b) \quad & \frac{d_+}{\lambda_s}(1+\beta) \gg [\beta + (\frac{d_+}{\lambda_s})^2] \left(\frac{w_i}{\lambda_s}\right) \end{aligned} \tag{4.8}$$

In the limit (a), the asymmetry parameter β is eliminated, and the steps tend to debunch instead of bunching. We did not address this situation in this thesis, further studies of the limit are presented by Krug et al. [160]. The limit (b) is related to our problem of forming step bunches in the dimple sample. It takes place when $w_i \ll d_+$ and $d_+/\lambda_s < 1$. In that case, the quadratic terms of terrace lengths in the numerators of Eqs. 4.8 are neglected relative to the linear ones. Thus, the step velocities in Eqs. (4.7) reduce to

$$\begin{aligned} v_- &= \frac{D_s \Omega n_s^e}{d_+(1+\beta)} \left\{ \frac{\beta}{k_B T}[\mu_i - \mu_{i+1}] + \frac{\beta d_+}{\lambda_s^2} w_i \right\} \\ v_+ &= \frac{D_s \Omega n_s^e}{d_+(1+\beta)} \left\{ \frac{\beta}{k_B T}[\mu_i - \mu_{i-1}] + \frac{d_+}{\lambda_s^2} w_{i-1} \right\} \end{aligned} \tag{4.9}$$

The two terms in the curly brackets in the Eqs. 4.9 have different contributions to the step-flow velocity. The first term is the difference between the chemical potentials

of two neighboring steps. It is inversely proportional to the cube of the distance between these neighbor steps. Therefore, this term is the repulsive force to keep the steps apart from each other. The second terms provide grounds for a step bunching instability because of the asymmetric barriers. If we set $k_- = \frac{D_s \Omega n_s^e}{(1+\beta)\lambda_s^2}$ and $k_+ = \beta k_-$, the step velocity has the analytic form:

$$v_i = v_+ + v_- = \left(\frac{\beta}{1+\beta}\right) \frac{D_s \Omega n_s^e}{k_B T d_+}(2\mu_i - \mu_{i+1} - \mu_{i-1}) + k_+ w_i + k_- w_{i-1} \tag{4.10}$$

in which

$$\frac{D_s \Omega n_s^e}{\lambda_s^2} = \frac{\Omega n_s^e}{\tau_s} = \Omega \hat{R}_e = R_e \tag{4.11}$$

is the desorption rate per surface atom. It is easy to verify that $k_+ + k_- = R_e$ and $k_+ - k_- = \frac{1-\beta}{1+\beta} * R_e < 0$. Those results are similar to the current-induced step bunching [162]. For the normal ES barrier $\beta > 1$, it leads to $k_+ - k_- < 0$ which is comparable step down direction force in the case of current-induced step bunching. It is a necessary and sufficient condition for forming step bunches. Assuming that there are N steps which have initial average terrace width w_0, the sum of all velocities of the steps give:

$$\sum_i^N v_i = k_+ \sum_i^N w_i + k_- \sum_i^N w_{i-1} = N R_e w_0 \tag{4.12}$$

in which $\sum_i^N w_i = \sum_i^N w_{i-1} = N w_0$ by using the periodic boundary condition. If we define v_0 as the characteristic velocity of the system (average step velocity), thus $v_0 = R_e w_0$.

4.2.2 Simulation of Step Bunching

4.2.2.1 Differential Equation Solver

In general, the step evolution can be obtained by solving the N first-order, linear, coupled equations:

$$\frac{dx}{dt} = f(x, x_0, t...) \tag{4.13}$$

where $x = [x_1, x_2, ...x_N]$ is the step positions at time t, y_0 is the initial step configurations, and f is the step velocities in Eq. 4.10. All of these functions are the N-dimensional array where N is the number of simulation steps. It is appropriate to use a periodic boundary condition because of a large number of steps N. Thus, the terrace width and chemical potential of the indexes N and $(N+1)$ are equal to those of the indexes 0 and 1 respectively.

4.2.2.2 Parameter Settings

From literatures [165] we obtained the values of SiC parameters for running simulation as followed:

- Three-bilayer step height: $h = 7.5\,\text{Å}$
- C-C (or Si-Si) distance: $a = 3.08\,\text{Å}$
- Carbon (or silicon) atom density in a SiC bilayer: $\rho = 0.366\,\text{Å}^2$
- Coefficient of surface diffusion: $D_s = 0.33 \times 10^{-2}\,\text{cm}^2\text{s}^{-1}$
- Diffusion length: $\lambda_s = 0.3 \times 10^{-4}\,\text{cm}$
- Equilibrium concentration of adatom at the step: $n_s^e = 0.314 \times 10^8\,\text{cm}^{-2}$
- Boltzmann energy: $k_B = 8.617 \times 10^{-5}\,\text{eV} \cdot \text{K}^{-1}$

  At room temperature: $k_B T = 0.0257\,\text{eV}$

  At $1250°C$: $k_B T = 0.1312\,\text{eV}$

The Ehrlich-Schwoebel barrier (ES) of a SiC step depends on the step directions and step thickness [165, 166]. For a three-bilayer-height step, the value of the asymmetric barrier is about $\Delta E \approx -0.4\,\text{eV}$ which is corresponding to the asymmetry parameter $\beta = \exp(-\Delta E/k_B T) \approx 21$. The exact value is not extremely important because the general simulation results are unchanged.

4.2.2.3 Numerical Difficulties

At first, the ordinary differential equations (ODEs) (Eq. 4.13) are stiff so that only the stiff solvers in Python and Matlab are considered. In Matlab program, the list of stiff solvers includes ode15s, ode23s, ode23t, ode23tb, in which ode23s solver is the fastest and most stable to run our simulation. In Python, we used the scipy package, specifically the function scipy.integrate.ode(func, x0, t, args=(), Dfun=None ...). The different methods delivered the same numerical results which made them reliable.

One of the difficulties of solving the stiff ODEs was the divergence of the integrations. It happened when a below step passed through the step above it, thus making the step velocities approach infinity. The simple solution to this problem was to increase the relative and absolute precisions (rtol and atol respectively). In our problem, the solvers worked well at $rtol = 1 \times 10^{-12}$ and $atol = 1 \times 10^{-12}$. The simulation time could be reduced significantly if the precisions were only increased while the solvers enter the stiff long time regions.

To increase the speed, efficiency, and reliability of the solvers, we supplied the Jacobian matrix into these solvers. The Jacobian matrix $\frac{\delta v_i}{\delta x_i}$ was obtained from the Eg. 4.10. After introducing the Jacobian matrix, the solvers ran faster and avoided the integral divergence with appropriate precisions. The detail python code of the simulation is attached at the Appendix C.

4.2.2.4 Numerical Results

In this section, some of the simulations results are shown. It is worth to mention that the evolution of the step bunches is starting from a uniform step array added small random Gaussian deviations. The size of the deviations does not change the characteristics of the problem, but it determines how fast the bunches start forming. The simulation size (or a number of the steps) N is necessary to control the upper limit of the step bunch. A typical simulation uses the standard deviation of the

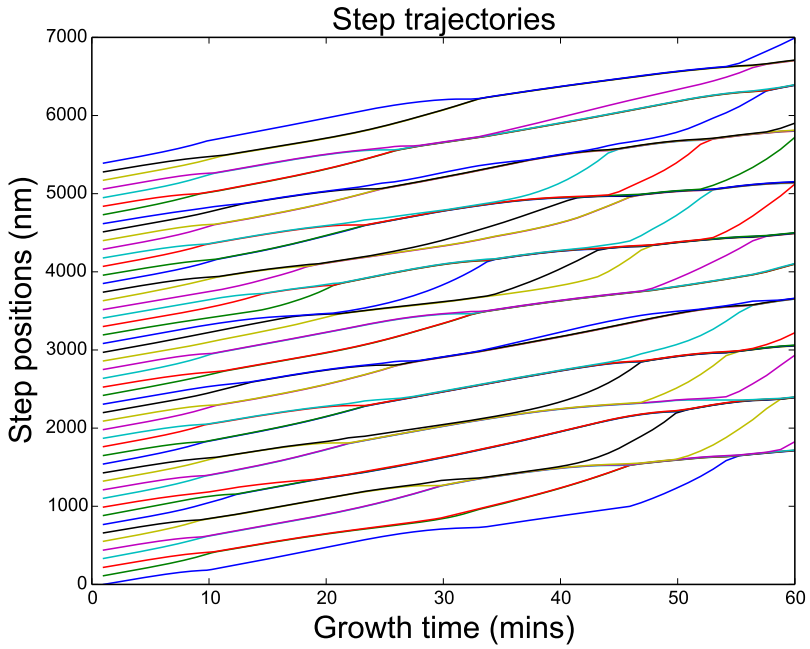

Figure 4.9: Step trajectories showing the formation of step bunches. The simulation parameters are $N = 50$, $w_0 = 1100\,\text{Å}$.

Gaussian distribution of 1-5 unit-cells and the number of steps of 500-2000.

Figure 4.9 shows the evolution of step trajectories as a function of growth time. The simulation size is 50 steps with average terrace width of 1100 Å (apart from the small random deviations). There are three interesting features in this figure: (i) forming step bunches from single steps, (ii) joining two bunches to a bigger bunch, and (iii) exchanging of mono steps between bunches starts after some time. As growth time passes by, the number of bunches reduce as well as the average bunch size increases.

A bunch is defined by the number of adjacent steps where the terraces between them are smaller than half of initial average terrace width, w_0 [162]. To count the number of steps in a bunch using the computer code, we define the "left" and "right" as the starting or ending of a bunch respectively. The bunch starts (or ends) where the larger-than-$w_0/2$ terrace is on the left (or right) of it. Then, the average bunch size is just the mean of the total bunches. Figure 4.10 reveals the average bunch size

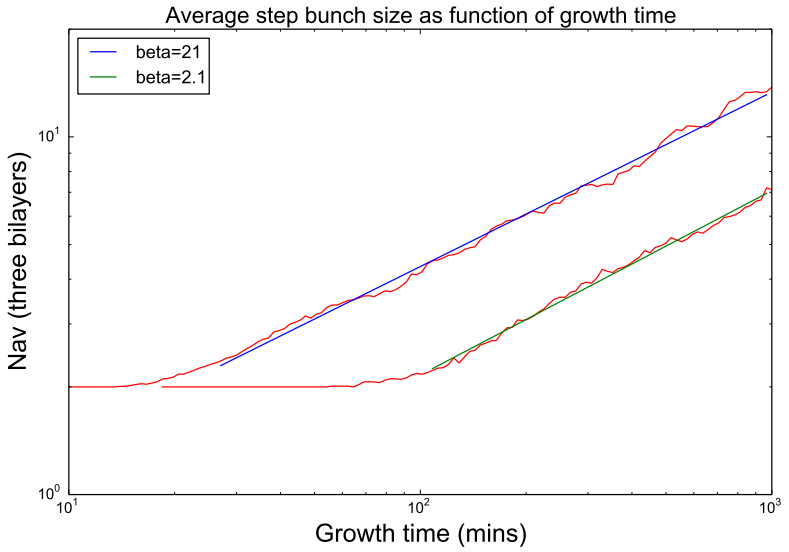

Figure 4.10: Evolution of the average bunch size as a function of growth time. The asymptotic values of these lines depend on the Ehrlich-Schwoebel (ES) barriers. However, the slope of the lines are approximately equal to $\frac{1}{2}$. Fitted lines have slope of 0.49 ± 0.01 (the top line) and 0.52 ± 0.01 (the bottom line). The simulation parameters are $N = 500$, $w_0 = 300\,\text{Å}$.

N_{av} (in term of three SiC bilayers) as a function of growth time in a log-log scale. The system includes 500 steps with the initial average terrace width of 300 Å. The initial induction time (the growth time when the steps start to bunch) depends on the ES barriers as seen from the different asymptotic values of the lines. However, the slopes of the lines remain constant ($\sim \frac{1}{2}$) while changing the asymptotic parameter, β. The slopes of the fitted lines are 0.49 ± 0.01 (the top line) and 0.52 ± 0.01 (the bottom line). The power law relation of the average bunch size and the growth time was reported previously for the current-induced step bunching [162, 167].

Finally, our target is to study the relation of average bunch size N_{av} at a different local angle α, to see if the experimental scaling $N_{av} \propto \alpha^{1/2}$ (Fig. 4.6) can be explained. The local angle is determined by the length of the average terrace width, w_0, and the single step height, h. In the simulation, I assume that three SiC bilayers travel together as a single layer so that the height of the step is a constant $h = 0.75\,\text{nm}$. Because the $N_{av} \propto t^{1/2}$ is already observed in simulations, we hypothesize that the

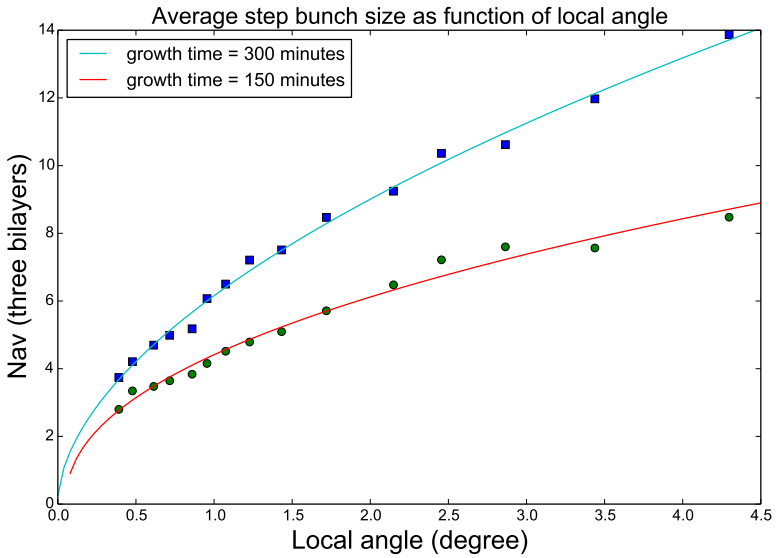

Figure 4.11: Average bunch size at the different local angles. The data are snapshotted after 150 min and 300 min time of growth of a 500 step system. The solid lines are the fits to power law relation $a(x - x_0)^b$ with $b = .55 \pm 0.04$ (the top line) and $b = .46 \pm 0.05$ (the bottom line).

angle scaling is related through a renormalization of the growth time, i.e., $N_{av} \propto (t/t_A)^{1/2}$, where t_A is a characteristic time that must be inversely proportional to the local angle; i.e., proportional to w_0. Dimensional considerations require a constant velocity, which we choose to be the characteristic velocity $v_0 = R_e w_0$. So, the observed identical exponent for angle and time scaling laws would follow naturally from an angle-independent value for v_0, which in turn implies that R_e is proportional to the step density (or angle), $1/w_0$. It is agreement with the relation of the growth rate and the off-angle reported previously [168]. Figure 4.11 shows the average bunch size at different local angles. The green circle and blue square data are calculated at the growth time of 150 min and 300 min respectively. The data is fitted to the power law relation $a(x-x_0)^b$. The results yield: $a = 4.5 \pm 0.3$, $b = 0.46 \pm 0.05$, $x_0 = 0.05 \pm 0.13$ for the growth time of 150 min and $a = 6.15 \pm 0.34$, $b = 0.55 \pm 0.04$, $x_0 = -0.003 \pm 0.090$ for the growth time of 300 min. As seen in the Fig. 4.9, the average bunch sizes (in term of three SiC bilayers) increase over growth time. Moreover, they follow the

power law relation with the vicinal angle, ax^b with $b \approx 1/2$. The fitted curves also closely pass through the origin $(0, 0)$ as the x_c parameters are small in both cases. The simulation results are similar to the experimental results in the Fig. 4.6.

4.3 Discussions

Despite potential complications not included in the model (e.g., graphene growth and possibly complex gas-surface reactions), the agreement of the numerical calculations and the experimental results (Fig. 4.6 and Fig. 4.11) validates our hypothesis that the desorption rate is proportional to the step density at a given local angle. Due to the higher instability of the atom at the step edge (because of more dangling bonds), the process of silicon evaporation from the silicon carbide surface would start along the step edge [169–171]. It means the rate of evaporation is proportional to the number of steps or step density. Moreover, the characteristic velocity of the system, $v_0 = R_e w_0$ in which R_e is the desorption rate and w_0 is the average terrace width, would remain constant at different local angles inside the dimple.

Another consideration to justify the model is to estimate the material lost from the SiC surface during the epitaxial growth of graphene. Because the silicon vapor pressure is much higher than carbon vapor pressure, the SiC etching rate is proportional to the silicon sublimation rate. In reality, there are two processes happened simultaneously while annealing: evaporation and condensation. However, at graphitization temperature, the silicon deposition rate is neglected because of the C-rich surface at this point. On the other hand, the silicon sublimation rate is estimated from Hertz-Knudsen equation [172]:

$$J_s = \frac{\alpha_e P_e}{\sqrt{2\pi m k_B T}} \tag{4.14}$$

in which α_e is the sticking coefficient of the Si atoms onto the surface ($0 \leq \alpha_e \leq 1$), P_e is the silicon vapor pressure, m is the mass of the molecule, k_B is the Boltzmann constant, and T is the temperature. Our purpose is to estimate the amount of SiC

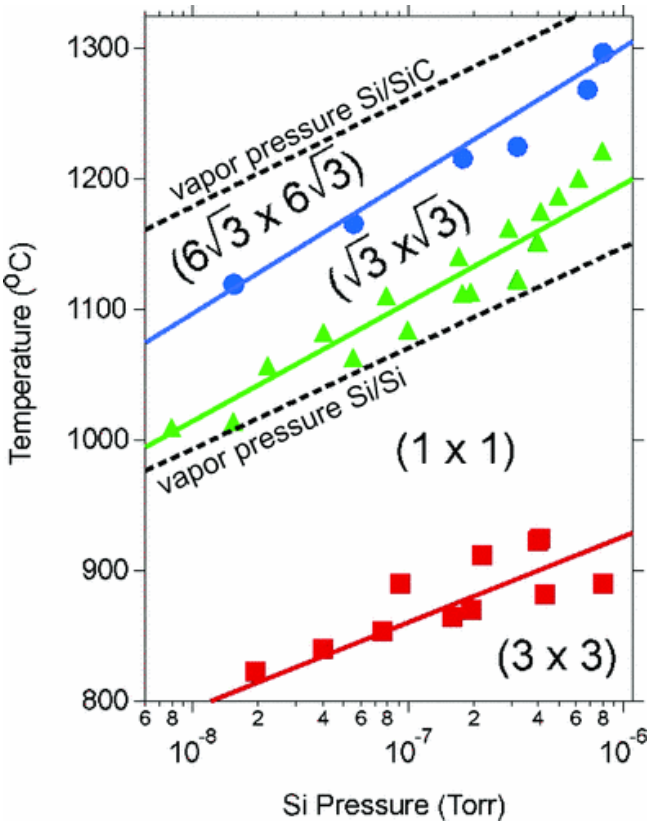

Figure 4.12: Pressure-temperature phase diagram for SiC surface. The top dashed line is the silicon vapor pressure over silicon carbide surface in equilibrium [173].

lost during the growth, so just take $\alpha_e = 1$ for the maximum case. The silicon vapor pressure over silicon carbide was extracted from the Si/SiC curve in the Fig. 4.12. At our graphitization temperature of $1250°C$, the approximation yields $P_e \approx 9 \times 10^{-8}$ Torr $= 1.2 \times 10^{-5}$ Pa. By substituting these parameters into the Eq. 4.14, the maximum silicon sublimation rate is $J_{max} \approx 1.5 \times 10^{17}\,\mathrm{m^{-2}s^{-1}}$. It is corresponding to the desorption rate of $R_e \approx 4 \times 10^{-3}$ three-bilayer sheet/s. Thus, the evaporation time for a three-bilayer SiC sheet is $\tau_e = 1/R_e = 250$ s. In our experiment, a SiC sample was annealed in 30 min which would result in the evaporation of ~ 7.2 layers of three-bilayer height. The amount of silicon carbide lost suggests an average step bunch height of 5-6 nm. This is of the same magnitude as the step bunch height measured by AFM inside the dimple (as calculated from the Fig. 4.6).

Our study on the step bunching of SiC gains the additional understanding of

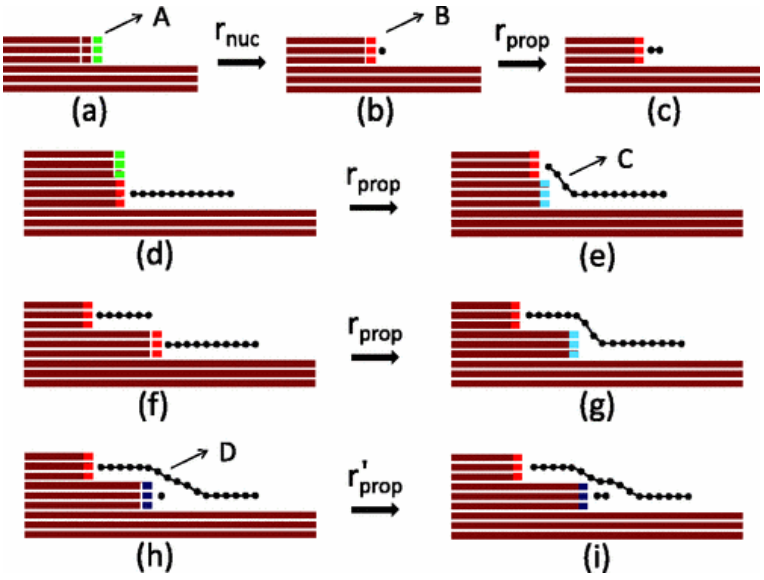

Figure 4.13: Kinetic Monte Carlo (KMC) model for the growth of graphene on a vicinal angle: (a) the initial triple-bilayer step structure, (b) the nucleation sites at the step edges, (c) a graphene layer propagating to the left, (d)(e) the graphene layer may "climb over" the upper terrace, (f)(g) two graphene sheets may coalesce upon further propagation, (h)(i) the second layer underneath the first one may then start [148].

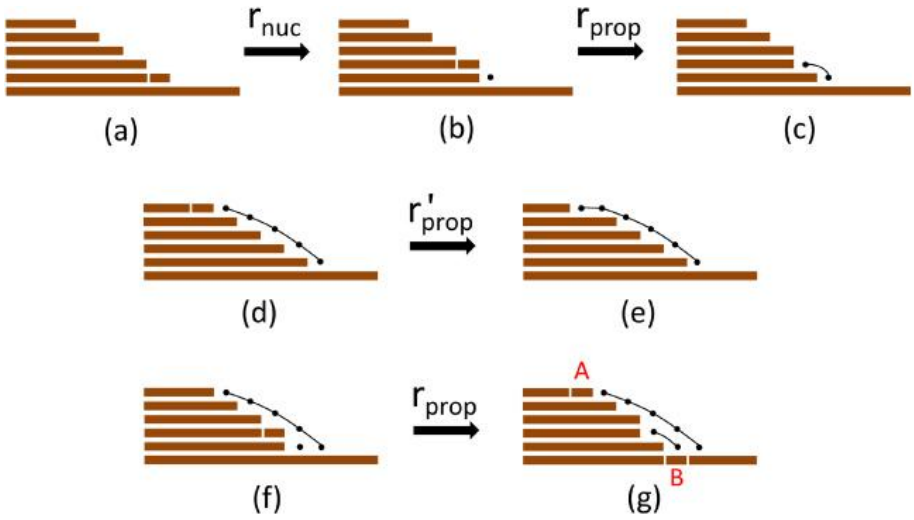

Figure 4.14: Kinetic Monte Carlo (KMC) model for the growth of graphene on a nano-facet. (a) initial structure of the nano-facet, (b) the nucleation sites at the bottom terrace, (c) a graphene layer propagating up the step, (d)(e) continuing over growth on the upper terrace, (f)(g) the start of the second layer underneath the first one [150].

the growth epitaxial graphene at vicinal angles. Ming and Zangwill [148, 150] have proposed a theoretical Kinetic Monte Carlo (KMC) model for the growth of graphene on a vicinal angle (Fig. 4.13) and on a nano-facet (Fig. 4.14). The former model supposes that the nucleation sites for graphene growth are at the step edges. Then, the sublimation of Si atoms from a triple-bilayer (half unit cell) step forms a single layer of graphene because of the mass conservation. The second layer of graphene grows underneath the first layer at the slower rate because of the difficulty to sublimate Si atoms from the SiC with the first graphene layer already present above. The latter model assumes that the bottom layer nucleates first, then the growth propagates up the steps of the facet. When reaching to the upper terrace, the growth continues on the flat terrace with the much slower propagation rate while the second layer may start at the bottom of the facet, underneath the first layer. Based on our experiments of annealing the SiC dimple in silane/argon gas, the mechanism of graphene growth on a vicinal angle is explained in a different way. The SEM image (Fig. 4.4) shows that most of the flat terraces covered by buffer layers (bright regions) while graphene formed at the step edges (dark regions). The results imply that the buffer layer is formed firstly on the whole surface at graphitization temperature. Further heating may not result in the formation of the another buffer layer underneath the first one. Otherwise, the carbon atoms can travel across the surface and form graphene at the edges. As studied by Zhang et al. [174], carbon atoms on underneath graphene layers may form carbon clusters, consisting of 6 atoms or more. The small carbon clusters are interacted weakly with the graphene via the van der Waals forces. The diffusion barrier of the clusters is negligibly small (6 meV). As the results, graphene prefers to growth at the step edges, thus following only the buffer layers on the terraces as implied by the SEM image. However, if all of the remaining carbon atoms (due to the losses of SiC to create the step bunches) form graphene, the average number of graphene layers inside the dimple is about 5 as interpreted from the experimental

data (Fig. 4.6). There are possibilities that the carbon can interact with the ionized hydrogen atoms and leave the surface or multi graphene layers are grown on the facet. STM study in the Fig. 4.7 reveals that the buffer layer on the terraces is undoubted rough. The rough surface may result from the carbon clusters left on the buffer layer.

4.4 Chapter Conclusion

In this chapter, I focused on studying of epitaxial graphene growth on vicinal silicon carbide. The vicinal angles of 0-5 ° were created by introducing a dimple on the top of an on-axis SiC wafer. After the hydrogen etching treatment, the surface of the sample was atomically flat with regular unit-cell steps as confirmed by SEM and AFM. The dimple was then graphitized at 1250 °C for 30 mins in silane/argon by using the graphite furnace. The AFM results indicated the step bunching of SiC after graphitization. The average bunch sizes increased with respect to the vicinal angle as a power law relation, ax^b with $b = 1/2$. The SEM and Auger results were quantitatively in agreement that the surface was covered by 1.5 graphene layers (a buffer layer and a half of graphene layer). As indicated in the SEM images, the growth of graphene started at step edges. The LEED patterns also proved the mixture of $(6\sqrt{3} \times 6\sqrt{3})R30°$ spots (from the buffer layer) and graphene spots.

A quasi-one-dimensional step bunching model was developed and simulated to verify the step bunching phenomenon. The step bunching mechanism came from the asymmetric energy barriers, so-called Ehrlich-Schwoebel effect. The simulation, being consistent with the previous reports of current-induced step bunching, confirmed the power law relation of the average step size and local angle. The results also implied that the material lost is proportional to the step density at a given position. Thus, the greater vicinal angles are, the bigger the step bunches and the more graphene coverage are on the surface. The experimental results indicated that graphene prefers to form on the step edges instead of growing underneath the buffer layer.

CHAPTER V

CONCLUSION

In this thesis, I have presented my research on the growth of epitaxial graphene on SiC under silane/argon gas mixtures. Prior to graphitization temperature, about 1200 °C, the deposition of silicon on SiC wafers creates reconstructions on both faces. On the Si-face of an on-axis SiC wafer, I have found new reconstructions of $(\sqrt{3} \times 7)R30°$ $(2\sqrt{3} \times \sqrt{13})R30°$, $(\sqrt{19} \times \sqrt{21})R36.6°$. On the C-face of the sample, the Si-rich surface only shows the well-known (3×3) and (2×2) phases. Under certain growth conditions close to the graphitization temperature, I have obtained the $(\sqrt{43} \times \sqrt{43})R7.6°$ reconstruction which is consistent with an earlier report [119]. I have revised and improved the Auger attenuation model for Auger spectra acquired using a cylindrical mirror analyzer (CMA). This model allows us to determine the thickness of a thin film based on the Auger peak intensities. In particular, I have applied it to estimate the graphene or silicon film thickness epitaxial grown on SiC substrates after converting retarding field analyzer data to CMA data. At graphitization temperature, I focused on the vicinal silicon carbide as a substrate for epitaxial graphene growth, using a spherical dimple ground into an on-axis SiC wafer to introduce a range of vicinal angles from 0° to 5°. After graphitized at 1250 °C for 30 mins in silane/argon by using the graphite furnace, the step bunches have formed from the unit-cell height, uniform step surface. The LEED patterns and Auger spectra reveal the presence of both buffer layer carbon and graphene on the surface. Further studies via SEM confirm that graphene starts to grow at the step edges. The AFM data have suggested the power law relation of the average bunch size and local angle. I have established a quasi-one-dimensional step bunching model to explain the step bunching of the SiC.

The simulation from the model confirms the power law relation from the experiments.

The epitaxial deposition of silicon suggests the possibility of the synthesis of epitaxial silicene sheets on SiC substrates. Silicene, the graphene equivalent for silicon, leads to new prospects for applications, especially due to its compatibility with Si-based electronics [175–180]. The worldwide search for silicene has not been fully successful, but I strongly believe that it could be achieved in our growth system. The existence of the $(\sqrt{43} \times \sqrt{43})R7.6^\circ$ and other new reconstructions affirms that our growth system is oxygen free, clean, and reliable to obtain the high-quality silicon thin film. In the future, we may alter growth conditions such as temperature, annealed time, and silane pressure to control the silicon deposition rate on the surface, thus being able to achieve a single layer of silicon on top of SiC.

Another work considered in the future is to take advantage of using vacuum box to transfer the sample to different UHV systems. Our growth system only has LEED and Auger to characterize the sample after growth. Unlike graphene, quite inactive to the air, a thin film of silicon is modified under the presence of oxygen. Thus, it is necessary to make a vacuum box to transfer the grown samples to other UHV systems for further characterization. We already made a vacuum transferred box to the room temperature STM system which would be used extensively to STM characterize the samples after heated.

One main purpose of this thesis is to discover a method to grow sidewall graphene nanoribbons on SiC facets. As investigated, the step bunching is formed on the vicinal silicon carbide. The average bunch size is dependent on the local angles and growth time. The findings allow us to create natural facets on a SiC substrate. If the starting surface is atomically flat with regular steps, the facet orientation and size would also depend on the local angles and growth time. Then, it is able to grow sidewall graphene nanoribbons (GNRs) in the natural facets. In this thesis, the quality of the GNRs was not fully studied. The continuity of the ribbons also needs further investigations.

With the ability to transferring samples to different UHV systems using the vacuum box, more research can be done to understand the growth mechanism of these GNRs.

APPENDIX A

AUGER ATTENUATION MODEL

```
#!/usr/bin/python
'''Auger model uses for estimation of Silicon or Graphene on Silicon
Carbide based on ratio of silicon and carbon intensity'''

import math
import numpy as np
# Multiplier gain (normalization)
T_90 = 14.14
T_272 = 20.68
gain = T_90/T_272
# Analyzer is at 42.2 degrees, or 0.736528944 rad
ang = 0.736528944
cos = math.cos(ang)
# Relative sensitivity factors
si_si = 0.35
si_c = 0.2
# Interplaner spacing (Angstrom)
a_sic = 2.51          # SiC bilayer spacing
d_sic = 0.63          # distance between Si-C in one bilayer
a_g = 3.35            # graphite layer spacing
a_si = 1.3578         # distance between Si bulk layers in (001) direction
# 2D atomic density (10**14 atoms/cm2)
n_sic = 12.25       # n_c = n_si = n_sic
n_g = 38.16
n_si = 6.775
# 3D atomic density (10**22 atoms/cm3)
rho_sib = 5.0
rho_g = 11.4
rho_sic = 4.83
# EAL at 90eV, 272eV, 2.5 keV
eal_sic = [3.165, 6.776, 36.51]
eal_si = [3.433, 7.532, 40.08]
eal_g = [3.883, 8.730, 45.28]

# Backscattering factors
bcf_si_sic = 1.100
bcf_si_si = 1.078
bcf_c_sic = 1.315
bcf_c_g = 1.139
class model:
    def __init__(self):
        # Effective attenuation length
        self.sic_90 = 1./(1./(eal_sic[0]*cos)+1./eal_sic[2])
        self.sic_272 = 1./(1./(eal_sic[1]*cos)+1./eal_sic[2])
        self.si_90 = 1./(1./(eal_si[0]*cos)+1./eal_si[2])
```

```
46          self.si_272 = 1./(1./(eal_si[1]*cos)+1./eal_si[2])
47          self.g_90 = 1./(1./(eal_g[0]*cos)+1./eal_g[2])
48          self.g_272 = 1./(1./(eal_g[1]*cos)+1./eal_g[2])
49          # \sigma*\gamma calculated from relative sensitivity factors
50          self.sig_si = si_si/(eal_si[0]*bcf_si_si)
51          self.sig_c = si_c/(eal_g[1]*bcf_c_g)
52          # Formula to calculate the sum exp(-i*x) from 0 to n-1
53          self.sum = lambda n,x: (np.exp(x)-np.exp(x-n*x))/(np.exp(x)-1.0)
54          #Silicon and Carbon signal from n layers of Bare SiC substrate
55          self.Si_sic = lambda n: bcf_si_sic*self.sig_si*n_sic*self.sum(n,
56          a_sic/self.sic_90)
57          self.C_sic = lambda n: bcf_c_sic*self.sig_c*n_sic*self.sum(n,
58          a_sic/self.sic_272)
59      def Graphene(self,n,m=50,face=0):
60          """ Si/C ratios as a function of Graphene layers on SiC
61          Arguments:  n: Graphene monolayer
62                      m: SiC bilayer
63                      face: C (Carbon) or Si (Silicon)
64          Returns:    Si/C ratio as a function of n"""
65          I_g = bcf_c_g*self.sig_c*n_g*self.sum(n,a_g/self.g_272)
66          if face == 'C':
67              I_si = self.Si_sic(m)*np.exp(-n*a_g/self.g_90-d_sic/self.sic_90)
68              I_c = self.C_sic(m)*np.exp(-n*a_g/self.g_272)
69              return gain*I_si/(I_g+I_c)
70          if face == 'Si':
71              I_si = self.Si_sic(m)*np.exp(-n*a_g/self.g_90)
72              I_c = self.C_sic(m)*np.exp(-n*a_g/self.g_272-d_sic/self.sic_272)
73              return gain*I_si/(I_g+I_c)
74      def Silicon(self,ML,m=50,face=0):
75          """ Si/C ratios as a function of Silicon layers on SiC substrate
76          Arguments:  ML: Amount of Silicon on bilayer SiC
77                      m: SiC bilayer
78                      face: C (Carbon) or Si (Silicon)
79          Returns:    Si/C ratio as the function of ML"""
80          # Exchange to Silicon layers on Silicon bulk (001)
81          asi = 0.543         #Angstrom
82          asic = 0.307        #Angstrom
83          n = ML*asi**2/(math.sqrt(3)*asic**2)
84          I_sib = bcf_si_si*self.sig_si*n_si*self.sum(n,a_si/self.si_90)
85          if face == 'C':
86              I_si = self.Si_sic(m)*np.exp(-n*a_si/self.si_90-d_sic/self.sic_90)
87              I_c = self.C_sic(m)*np.exp(-n*a_si/self.si_272)
88              return gain*(I_sib+I_si)/I_c
89          if face == 'Si':
90              I_si = self.Si_sic(m)*np.exp(-n*a_si/self.si_90)
91              I_c = self.C_sic(m)*np.exp(-n*a_si/self.si_272-d_sic/self.sic_272)
92              return gain*(I_sib+I_si)/I_c
```

APPENDIX B

CONVERT RFA AUGER DATA TO CMA-SCALING AND RESOLUTION

Make certain to adjust T start and step.)

```
#!/usr/bin/python
import numpy as np
import cPickle
from Scientific.IO import NetCDF as ncdf
def readRFA(filename):
    '''
    Read cPickle file generated by RFA.
    '''

    # Get the raw data
    with open(filename) as fh:
        xdata, ydata = cPickle.load(fh)
    # Convert lists to numpy arrays
    x_array = np.array(xdata)
    y_array = np.array(ydata)
    return(x_array,y_array)
def readCMA(filename):
    '''
    Read netCDF file generated by CMA.
    '''

    # open the netcdf data file
    data=ncdf.NetCDFFile(filename,'r')

    # copy to local variables
    energy = data.variables['ENERGY'][:]
    intensity = data.variables['INTENSITY'][:]
    return((energy,intensity))
def Icma(E,Irfa,T=1.,A=1.,B=None,C=0.,D=0.,bkgrange=[140.,240.]):
    '''
    Calculate CMA signal from RFA signal.
    '''
    if B == None:
        B = Irfa[((E >= bkgrange[0])
        & (E <= bkgrange[1])).nonzero()].mean()
    dE = (E[-1]-E[0])/(len(E)-1)
    NE = (Irfa-B).cumsum()*dE + C
    result = A*np.diff(E*T*NE)/dE + D
    return(np.append(result,result[-1]))
```

APPENDIX C

QUASI-1D STEP BUNCHING MODEL

```
#!/usr/bin/python
"""
1D step model to study quantitatively growth of step bunches.
Reproduced prof. John Weeks numerical results.
"""

import ipdb
import numpy as np
from scipy.integrate import ode
import matplotlib.pyplot as plt

# Experimental parameters
a = 3.08                # C-C (Si-Si) distance
beta = 444                # Asymmetry coefficient: K^{-}/K^{+}
Re = 1./250                # Depostion rate: layer/s

lamb = 0.3E-4          # Surface diffusion length: cm
Ds = 0.33E-2          # Coefficient of surface diffusion: cm^2/s
kT = 0.1312                # Bolzmann constant at 1200C: eV
R = 1E13                # Vibration frequency or hopping rate: 1/s
E = 2.                        # ES barrier: eV
kapa = R*exp(-E/kT)                # kinetice coefficient: (1/s)

# Calculated coefficients:
v0 = 1E8*lamb^2*kapa/(kT*Ds)         # Velocity factor: A/(eV*s)
k1 = Re/(1.+beta)
k2 = beta*Re/(1.+beta)

#--------------------------------------------------------------------------
class Model:
    """The evolution of the steps by solving the differential
            equation: dx/dt = vstep(t,x)
    Input:
        N:      Number of steps in simulation
        w0:     Average terrace width, measured in angstroms
        T:      Tuple giving growth time in seconds
        log:    True: logarithmic time steps,
                False: linear time steps (default)
        sd:     Standard deviation for step positions (units of a)
        ODEkws: Dictionary of keywords for scipy.integrate.ode()
    Output:
        vector of step positions (angstroms):
        y = [x_0, x_1, ... x_(N-1)]

    """
```

```
46
47
48      def __init__(self, N=300, w0=1100, T=(0.,1.*60,10.), log=False,
49                   sd=10.,quiet=False,**ODEkws):
50          self.N = N
51          self.w0 = w0
52          self.quiet = quiet
53          if log:
54              self.t = np.logspace(*T)
55          else:
56              self.t = np.linspace(*T)
57          self.ODEkws = ODEkws
58          # set some default keyword values:
59          if not 'method' in ODEkws: self.ODEkws['method'] = 'bdf'
60          if not 'with_jacobian' in ODEkws: self.ODEkws['with_jacobian'] = 1
61          if not 'nsteps' in ODEkws: self.ODEkws['nsteps'] = 10000
62          if not 'rtol' in ODEkws: self.ODEkws['rtol'] = 1.E-12
63          if not 'atol' in ODEkws: self.ODEkws['atol'] = 1.E-12
64          # k1, k2 inversely proportional to terrace widths:
65          self.k1 = k1*1100./self.w0
66          self.k2 = k2*1100./self.w0
67          # Define N dimensional arrays
68          self.y = np.zeros([self.t.size,self.N],dtype='float128')
69          sig = np.random.normal(scale=sd*3.08, size=N+1)
70          sig[0] = 0.
71          pos = np.array([(np.power(i,1)).astype(int)*w0+sig[i]
72                          for i in np.arange(N+1)])
73          self.SimWidth = pos.max()  # Total width of simulation (angstroms)
74          self.y[0,:] = np.sort(pos)[0:-1]  # Monotonic conditions
75          self.minterrace = 0.  # minimum terrace width, for checking.
76
77
78      def mu(self,x):
79          '''The chemical potential, calculated from step positions.
80          '''
81          xaug = np.append(x,np.array(x[0:4]+self.SimWidth))
82          xaug = np.insert(xaug,0,np.array(x[self.N-2:self.N]-self.SimWidth))
83          terr = np.ediff1d(xaug) # N+5 terraces; zero index at +2
84          ti3 = terr**-3
85          return -mc*ediff1d(ti3)[1:-3]
86
87
88      def vstep(self,t,x):
89          """Velocities of N steps.
90
91             It's easiest to implement periodic BC in the terrace widths,
92             since they're relative measures.
93          """
94          # Set up augmented terrace array for implementing periodic BC
95          xaug = x
96          xaug = np.append(x,np.array(x[0:4]+self.SimWidth))
97          xaug = np.insert(xaug,0,np.array(x[self.N-2:self.N]-self.SimWidth))
98          # N+6 steps, with zero index at +2
99          terr = np.ediff1d(xaug) # N+5 terraces; zero index at +2
100         inds, = np.where(terr<self.minterrace)
101         if inds.any():
```

```
            errstr = "Terrace width less minimum!"
            raise Exception(errstr)
        ti3 = terr**-3
        diff3 = np.diff(ti3,3)  #zero index at +2
        vel = v0*diff3[0:-2] + self.k1*terr[2:-3] + self.k2*terr[1:-4]
        vel[vel<0]=0
        return vel


    def jac(self,t,x):
        """Jacobian of vstep (step velocities);
        partial derivatives of vstep w/ respect to step positions x.
        """
        jacmat = np.zeros([self.N+5,self.N+5],dtype='float128')
        xaug = x
        xaug = np.append(x,np.array(x[0:4]+self.SimWidth))
        xaug = np.insert(xaug,0,np.array(x[self.N-2:self.N]-self.SimWidth))
        # N+6 steps, with zero index at +2
        terr = np.ediff1d(xaug) # N+5 terraces; zero index at +2
        ti4 = terr**-4
        AA = 3.*v0
        kappa = np.array([0., -self.k2, -self.k1+self.k2, self.k1, 0.])
        for i in range(2,self.N+3):
            jacmat[i,i-2:i+3] = AA*np.array([-(ti4[i-2]), (3.*ti4[i-1] +
             ti4[i-2]),-3.*(ti4[i] + ti4[i-1]), (ti4[i+1] + 3.*ti4[i]),
                                -(ti4[i+1])]) + kappa
        jacmat[-5:-3,2:4] = jacmat[-5:-3,-3:-1]
        return jacmat[2:-3,2:-3]


    def checkTerraces(self,t,x):
        """ Check for negative terrace widths and exit ode solver.
        """
        xaug = np.append(x,np.array(x[0:4]+self.SimWidth))
        xaug = np.insert(xaug,0,np.array(x[self.N-2:self.N]-self.SimWidth))
        terr = np.ediff1d(xaug)
        if np.where(terr<0.)[0].any():
            errstr = "leaving solver..."
            raise Exception(errstr)
            return -1
        else:
            self.lastx = x
            return 0

    def evol(self,last=0):
        """Evolution of steps with time, using scipy.integrate.ode class
        """
        solve = ode(self.vstep,self.jac).set_integrator('lsoda',
               **self.ODEkws)
        solve.set_initial_value(self.y[last,:],self.t[last])
        for i in np.arange(last+1,self.t.size):
            if not self.quiet: print("Step: {0:d}, Time: {1:f}
                                     \n".format(i,self.t[i]))
            self.y[i,:] = solve.integrate(self.t[i])
```

```
158     def bunch(self):
159         """
160         Return the average bunch sizes for all times.
161         """
162         Nav = np.zeros(self.t.size)
163         for t in np.arange(self.t.size):
164             terr = np.ediff1d(np.append(self.y[t,:],self.y[t,0:2]
165                               +self.SimWidth))
166             temp = np.ediff1d((terr < self.w0/2.).astype(np.int))
167             left = np.where(temp==1)[0] + 1
168             right = np.where(temp==-1)[0] + 1
169             if (right.size == 0 or left.size == 0):
170                 Nav[t] = 0.
171             else:
172                 if right[0] < left[0]:
173                     right=np.roll(right,-1)
174                     right[-1] += self.N
175                 bunches = right - left + 1
176                 Nav[t] = bunches.mean()
177         return Nav
```

Bibliography

[1] P. R. Wallace. "The band theory of graphite." *Physical Review* **71** (9), 622–634 (1947).

[2] N. D. Mermin. "Crystalline order in two dimensions." *Physical Review* **176** (1), 250–254 (1968).

[3] J. Shelton, H. Patil, and J. Blakely. "Equilibrium segregation of carbon to a nickel (111) surface: A surface phase transition." *Surface Science* **43** (2), 493?520 (1974).

[4] A. Van Bommel, J. Crombeen, and A. Van Tooren. "LEED and Auger electron observations of the SiC(0001) surface." *Surface Science* **48** (2), 463?472 (1975).

[5] C. Berger, Z. Song, T. Li, X. Li, A. Y. Ogbazghi, R. Feng, Z. Dai, A. N. Marchenkov, E. H. Conrad, P. N. First, and et al.. "Ultrathin epitaxial graphite: 2D electron gas properties and a route toward graphene-based nanoelectronics." *The Journal of Physical Chemistry B* **108** (52), 19 912?19 916 (2004).

[6] K. S. Novoselov. "Electric field effect in atomically thin carbon films." *Science* **306** (5696), 666–669 (2004).

[7] S. Stankovich, D. A. Dikin, R. D. Piner, K. A. Kohlhaas, A. Kleinhammes, Y. Jia, Y. Wu, S. T. Nguyen, and R. S. Ruoff. "Synthesis of graphene-based nanosheets via chemical reduction of exfoliated graphite oxide." *Carbon* **45** (7), 1558–1565 (2007).

[8] K. S. Kim, Y. Zhao, H. Jang, S. Y. Lee, J. M. Kim, K. S. Kim, J.-H. Ahn, P. Kim, J.-Y. Choi, and B. H. Hong. "Large-scale pattern growth of graphene films for stretchable transparent electrodes." *Nature* **457** (7230), 706–710 (2009).

[9] X. Li, W. Cai, J. An, S. Kim, J. Nah, D. Yang, R. Piner, A. Velamakanni, I. Jung, E. Tutuc, and et al.. "Large-area synthesis of high-quality and uniform graphene films on copper foils." *Science* **324** (5932), 1312–1314 (2009).

[10] A. H. Castro Neto, F. Guinea, N. M. R. Peres, K. S. Novoselov, and A. K. Geim. "The electronic properties of graphene." *Reviews of Modern Physics* **81** (1), 109–162 (2009).

[11] C. Riedl, C. Coletti, T. Iwasaki, A. A. Zakharov, and U. Starke. "Quasi-free-standing epitaxial graphene on SiC obtained by hydrogen intercalation." *Physical Review Letters* **103** (24) (2009).

[12] E. Pop, V. Varshney, and A. K. Roy. "Thermal properties of graphene: Fundamentals and applications." *MRS Bulletin* **37** (12), 1273–1281 (2012).

[13] E. P. Randviir, D. A. Brownson, and C. E. Banks. "A decade of graphene research: production, applications and outlook." *Materials Today* **17** (9), 426–432 (2014).

[14] A. K. Sood, I. Lund, Y. R. Puri, H. Efstathiadis, P. Haldar, N. K. Dhar, J. Lewis, M. Dubey, E. Zakar, P. Wijewarnasuriya, and et al.. "Review of graphene technology and its applications for electronic devices." *Graphene - New Trends and Developments* (2015).

[15] A. K. Geim. "Graphene: Status and prospects." *Science* **324** (5934), 1530–1534 (2009).

[16] K. S. Novoselov, V. I. Fal'ko, L. Colombo, P. R. Gellert, M. G. Schwab, and K. Kim. "A roadmap for graphene." *Nature* **490** (7419), 192–200 (2012).

[17] S. V. Morozov, K. S. Novoselov, M. I. Katsnelson, F. Schedin, D. C. Elias, J. A. Jaszczak, and A. K. Geim. "Giant intrinsic carrier mobilities in graphene and its bilayer." *Physical Review Letters* **100** (1) (2008).

[18] K. Bolotin, K. Sikes, Z. Jiang, M. Klima, G. Fudenberg, J. Hone, P. Kim, and H. Stormer. "Ultrahigh electron mobility in suspended graphene." *Solid State Communications* **146** (9-10), 351–355 (2008).

[19] N. Sun, K. Tahy, H. Xing, D. Jena, G. Arnold, and S. T. Ruggiero. "Electrical noise and transport properties of graphene." *Journal of Low Temperature Physics* **172** (3-4), 202–211 (2013).

[20] F. Schwierz. "Graphene transistors." *Nature Nanotechnology* **5** (7), 487–496 (2010).

[21] H. Tetlow, J. Posthuma de Boer, I. Ford, D. Vvedensky, J. Coraux, and L. Kantorovich. "Growth of epitaxial graphene: Theory and experiment." *Physics Reports* **542** (3), 195–295 (2014).

[22] K. S. Novoselov, D. Jiang, F. Schedin, T. J. Booth, V. V. Khotkevich, S. V. Morozov, and A. K. Geim. "Two-dimensional atomic crystals." *Proceedings of the National Academy of Sciences* **102** (30), 10 451–10 453 (2005).

[23] A. Reina, X. Jia, J. Ho, D. Nezich, H. Son, V. Bulovic, M. S. Dresselhaus, and J. Kong. "Large area, few-layer graphene films on arbitrary substrates by chemical vapor deposition." *Nano Letters* **9** (1), 30–35 (2009).

[24] J. Hass, R. Feng, T. Li, X. Li, Z. Zong, W. A. de Heer, P. N. First, E. H. Conrad, C. A. Jeffrey, and C. Berger. "Highly ordered graphene for two dimensional electronics." *Applied Physics Letters* **89** (14), 143 106 (2006).

[25] J. Baringhaus, M. Ruan, F. Edler, A. Tejeda, M. Sicot, A. Taleb-Ibrahimi, A.-P. Li, Z. Jiang, E. H. Conrad, C. Berger, and et al.. "Exceptional ballistic transport in epitaxial graphene nanoribbons." *Nature* **506** (7488), 349–354 (2014).

[26] A. K. Geim and K. S. Novoselov. "The rise of graphene." *Nature Materials* **6** (3), 183–191 (2007).

[27] R. Heyrovska. "Atomic structures of graphene, benzene and methane with bond lengths as sums of the single, double and resonance bond radii of carbon." *arxiv.org* (2008).

[28] C. Lee, X. Wei, J. W. Kysar, and J. Hone. "Measurement of the elastic properties and intrinsic strength of monolayer graphene." *Science* **321** (5887), 385–388 (2008).

[29] J.-W. Jiang, J.-S. Wang, and B. Li. "Young's modulus of graphene: A molecular dynamics study." *Physical Review B* **80** (11) (2009).

[30] H. W. Kroto, J. R. Heath, S. C. OBrien, R. F. Curl, and R. E. Smalley. "C60: Buckminsterfullerene." *Nature* **318** (6042), 162–163 (1985).

[31] S. Iijima. "Helical microtubules of graphitic carbon." *Nature* **354** (6348), 56–58 (1991).

[32] N. M. R. Peres. "Colloquium: The transport properties of graphene: An introduction." *Reviews of Modern Physics* **82** (3), 2673–2700 (2010).

[33] T. Ando. "The electronic properties of graphene and carbon nanotubes." *NPG Asia Materials* **1** (1), 17–21 (2009).

[34] T. Ohta. "Controlling the electronic structure of bilayer graphene." *Science* **313** (5789), 951–954 (2006).

[35] X. Fan, Z. Shen, A. Q. Liu, and J.-L. Kuo. "Band gap opening of graphene by doping small boron nitride domains." *Nanoscale* **4** (6), 2157 (2012).

[36] G. Gui, J. Li, and J. Zhong. "Band structure engineering of graphene by strain: First-principles calculations." *Physical Review B* **78** (7) (2008).

[37] M. Y. Han, B. Ozyilmaz, Y. Zhang, and P. Kim. "Energy band-gap engineering of graphene nanoribbons." *Physical Review Letters* **98** (20) (2007).

[38] J. Casady and R. Johnson. "Status of silicon carbide (SiC) as a wide-bandgap semiconductor for high-temperature applications: A review." *Solid-State Electronics* **39** (10), 1409–1422 (1996).

[39] P. Neudeck, A. Trunek, D. Spry, J. Powell, H. Du, M. Skowronski, X. Huang, and M. Dudley. "CVD growth of 3C-SiC on 4H/6H mesas." *Chemical Vapor Deposition* **12** (8-9), 531–540 (2006).

[40] G. C. Capitani, S. Di Pierro, and G. Tempesta. "The $6H-SiC$ structure model: Further refinement from SCXRD data from a terrestrial moissanite." *American Mineralogist* **92** (2-3), 403–407 (2007).

[41] L. S. Ramsdell. "Studies on silicon carbide." *American Mineralogist* **32** (1-2), 64–82 (1947).

[42] D. Pashley. "Epitaxy growth mechanisms." *Materials Science and Technology* **15** (1), 2–8 (1999).

[43] F. C. Frank and J. H. van der Merwe. "One-dimensional dislocations. ii. misfitting monolayers and oriented overgrowth." *Proceedings of the Royal Society A: Mathematical, Physical and Engineering Sciences* **198** (1053), 216–225 (1949).

[44] "Molecular beam epitaxy (MBE)." The University of Kaiserslautern: https://www.physik.uni-kl.de/en/hillebrands/research/methods/molecular-beam-epitaxy/.

[45] C. Riedl, C. Coletti, and U. Starke. "Structural and electronic properties of epitaxial graphene on $SiC(0001)$: a review of growth, characterization, transfer doping and hydrogen intercalation." *Journal of Physics D: Applied Physics* **43** (37), 374 009 (2010).

[46] A. Ouerghi, M. G. Silly, M. Marangolo, C. Mathieu, M. Eddrief, M. Picher, F. Sirotti, S. El Moussaoui, and R. Belkhou. "Large-area and high-quality epitaxial graphene on off-axis SiC wafers." *ACS Nano* **6** (7), 6075–6082 (2012).

[47] F. La Via, M. Camarda, and A. La Magna. "Mechanisms of growth and defect properties of epitaxial SiC." *Appl. Phys. Rev.* **1** (3), 031 301 (2014).

[48] N. Mishra, J. Boeckl, N. Motta, and F. Iacopi. "Graphene growth on silicon carbide: A review." *physica status solidi (a)* **213** (9), 2277–2289 (2016).

[49] T. Li. *Characteristics of graphite films on silicon- and carbon-Terminated faces of silicon carbide.* Dissertation, Georgia Institute of Technology (2006).

[50] G. Yazdi, T. Iakimov, and R. Yakimova. "Epitaxial graphene on SiC: A review of growth and characterization." *Crystals* **6** (5), 53 (2016).

[51] W. A. de Heer, C. Berger, M. Ruan, M. Sprinkle, X. Li, Y. Hu, B. Zhang, J. Hankinson, and E. Conrad. "Large area and structured epitaxial graphene produced by confinement controlled sublimation of silicon carbide." *Proceedings of the National Academy of Sciences* **108** (41), 16 900–16 905 (2011).

[52] J. R. Hass. *Structural characterization of epitaxial graphene on silicon carbide*. Dissertation, Georgia Institute of Technology (2008).

[53] G. M. Rutter. *Atomic scale properties of epitaxial graphene grown on $SiC(0001)$*. Dissertation, Georgia Institute of Technology (2008).

[54] N. Sharma. *Microscopic and spectroscopic studies of growth and electronic structure of epitaxial graphene*. Dissertation, Georgia Institute of Technology (2009).

[55] K. D. Kubista. *Local measurements of cyclotron states in graphene*. Dissertation, Georgia Institute of Technology (2011).

[56] Y. Hu. *Production and properties of epitaxial graphene on the carbon terminated face of hexagonal silicon carbide*. Ph.D. thesis, Georgia Institute of Technology (2013).

[57] F. Wang. *Surface/interface modification and characterization of C-face epitaxial graphene*. Ph.D. thesis, Georgia Institute of Technology (2015).

[58] M. S. Nevius. *Improved growth, ordering, and characterization of sidewall epitaxial graphene nanoribbons*. Ph.D. thesis, Georgia Institute of Technology (2016).

[59] Luxmi, N. Srivastava, G. He, R. M. Feenstra, and P. J. Fisher. "Comparison of graphene formation on C-face and Si-face $SiC(0001)$ surfaces." *Physical Review B* **82** (23) (2010).

[60] R. Yakimova, G. R. Yazdi, T. Iakimov, J. Eriksson, and V. Darakchieva. "(invited) challenges of graphene growth on silicon carbide." *ECS Transactions* **53** (1), 9–16 (2013).

[61] Z. R. Robinson, G. G. Jernigan, M. Currie, J. K. Hite, K. M. Bussmann, L. O. Nyakiti, N. Y. Garces, A. Nath, M. V. Rao, V. D. Wheeler, and et al.. "Challenges to graphene growth on SiC: Substrate effects, hydrogen etching and growth ambient." *Carbon* **81**, 73–82 (2015).

[62] R. Y. Syvajarvi, M and E. Janzan. "Interfacial properties in liquid phase growth of SiC." *Journal of The Electrochemical Society* **146** (4), 1565 (1999).

[63] P. N. First, W. A. de Heer, T. Seyller, C. Berger, J. A. Stroscio, and J.-S. Moon. "Epitaxial graphenes on silicon carbide." *MRS Bulletin* **35** (04), 296?305 (2010).

[64] J. Hicks, K. Shepperd, F. Wang, and E. H. Conrad. "The structure of graphene grown on the $SiC(000\bar{1})$ surface." *Journal of Physics D: Applied Physics* **45** (15), 154 002 (2012).

[65] J. B. Hannon, M. Copel, and R. M. Tromp. "Direct measurement of the growth mode of graphene on $SiC(0001)$ and $SiC(000\bar{1})$." *Physical Review Letters* **107** (16) (2011).

[66] F. Wang, K. Shepperd, J. Hicks, M. S. Nevius, H. Tinkey, A. Tejeda, A. Taleb-Ibrahimi, F. Bertran, P. Le Fevre, D. B. Torrance, and et al.. "Silicon intercalation into the graphene-SiC interface." *Physical Review B* **85** (16) (2012).

[67] G. R. Yazdi, R. Vasiliauskas, T. Iakimov, A. Zakharov, M. Syvajarvi, and R. Yakimova. "Growth of large area monolayer graphene on $3C - SiC$ and a comparison with other SiC polytypes." *Carbon* **57**, 477–484 (2013).

[68] I. Forbeaux, J.-M. Themlin, and J.-M. Debever. "Heteroepitaxial graphite on $6H - SiC(0001)$: Interface formation through conduction-band electronic structure." *Physical Review B* **58** (24), 16 396–16 406 (1998).

[69] J. Hass, W. A. de Heer, and E. H. Conrad. "The growth and morphology of epitaxial multilayer graphene." *Journal of Physics: Condensed Matter* **20** (32), 323 202 (2008).

[70] L. I. Johansson, S. Watcharinyanon, A. A. Zakharov, T. Iakimov, R. Yakimova, and C. Virojanadara. "Stacking of adjacent graphene layers grown on C-face SiC." *Physical Review B* **84** (12) (2011).

[71] J. Borysiuk, R. Bozek, K. Grodecki, A. Wysmolek, W. Strupinski, R. Stepniewski, and J. M. Baranowski. "Transmission electron microscopy investigations of epitaxial graphene on C-terminated 4H-SiC." *Journal of Applied Physics* **108** (1), 013 518 (2010).

[72] N. Camara, B. Jouault, A. Caboni, B. Jabakhanji, W. Desrat, E. Pausas, C. Consejo, N. Mestres, P. Godignon, and J. Camassel. "Growth of monolayer graphene on 8° off-axis $4H - SiC(000\bar{1})$ substrates with application to quantum transport devices." *Applied Physics Letters* **97** (9), 093 107 (2010).

[73] L. B. Biedermann, M. L. Bolen, M. A. Capano, D. Zemlyanov, and R. G. Reifenberger. "Insights into few-layer epitaxial graphene growth on $4H - SiC(000\bar{1})$ substrates from STM studies." *Physical Review B* **79** (12) (2009).

[74] K. Wakabayashi, Y. Takane, M. Yamamoto, and M. Sigrist. "Electronic transport properties of graphene nanoribbons." *New Journal of Physics* **11** (9), 095 016 (2009).

[75] K. Wakabayashi, K.-i. Sasaki, T. Nakanishi, and T. Enoki. "Electronic states of graphene nanoribbons and analytical solutions." *Science and Technology of Advanced Materials* **11** (5), 054 504 (2010).

[76] X. Li. *Epitaxial graphene films on SiC: growth, characterization, and devices*. Dissertation, Georgia Institute of Technology (2008).

[77] K. Nakada, M. Fujita, G. Dresselhaus, and M. S. Dresselhaus. "Edge state in graphene ribbons: Nanometer size effect and edge shape dependence." *Physical Review B* **54** (24), 17 954–17 961 (1996).

[78] L. Brey and H. A. Fertig. "Electronic states of graphene nanoribbons studied with the Dirac equation." *Physical Review B* **73** (23) (2006).

[79] Y.-W. Son, M. L. Cohen, and S. G. Louie. "Energy gaps in graphene nanoribbons." *Physical Review Letters* **97** (21) (2006).

[80] M. Sprinkle, M. Ruan, Y. Hu, J. Hankinson, M. Rubio-Roy, B. Zhang, X. Wu, C. Berger, and W. A. de Heer. "Scalable templated growth of graphene nanoribbons on SiC." *Nature Nanotechnology* **5** (10), 727–731 (2010).

[81] J. Baringhaus, J. Aprojanz, J. Wiegand, D. Laube, M. Halbauer, J. H?bner, M. Oestreich, and C. Tegenkamp. "Growth and characterization of sidewall graphene nanoribbons." *Applied Physics Letters* **106** (4), 043 109 (2015).

[82] I. Palacio, A. Celis, M. N. Nair, A. Gloter, A. Zobelli, M. Sicot, D. Malterre, M. S. Nevius, W. A. de Heer, C. Berger, and et al.. "Atomic structure of epitaxial graphene sidewall nanoribbons: Flat graphene, miniribbons, and the confinement gap." *Nano Lett.* **15** (1), 182–189 (2015).

[83] W. Norimatsu and M. Kusunoki. "Formation process of graphene on $SiC(0001)$." *Physica E: Low-dimensional Systems and Nanostructures* **42** (4), 691–694 (2010).

[84] V. Ramachandran, M. F. Brady, A. R. Smith, R. M. Feenstra, and D. W. Greve. "Preparation of atomically flat surfaces on silicon carbide using hydrogen etching." *Journal of Electronic Materials* **27** (4), 308–312 (1998).

[85] S. Nie, C. Lee, R. Feenstra, Y. Ke, R. Devaty, W. Choyke, C. Inoki, T. Kuan, and G. Gu. "Step formation on hydrogen-etched $6H - SiC(0001)$ surfaces." *Surface Science* **602** (17), 2936–2942 (2008).

[86] D. B. Torrance. *Growth and electronic properties of nanostructured epitaxial graphene on silicon carbide*. Ph.D. thesis, Georgia Institute of Technology (2013).

[87] F. Dulot, L. Mansour, A. Leycuras, W. Wulfhekel, D. Sander, F. Arnaud d'Avitaya, and M. Hanbucken. "Structure and morphology of concave-shaped surfaces on $6H-SiC(0001)$ after H2 etching." *Applied Surface Science* **187** (3-4), 319–325 (2002).

[88] W. Wulfhekel, D. Sander, S. Nitsche, F. Dulot, A. Leycuras, and M. Hanbucken. "Regular step formation on concave-shaped surfaces on $6H-SiC(0001)$." *Surface Science* **550** (1-3), 8–14 (2004).

[89] W. Wulfhekel, D. Sander, S. Nitsche, F. Dulot, A. Leycuras, and M. Hanbucken. "Structural reorganisation of vicinal surfaces on $6H-SiC(0001)$ induced by hot hydrogen etching." *Applied Surface Science* **234** (1-4), 251–255 (2004).

[90] D. L. Miller. *Atomic-scale spectroscopy and mapping of magnetic states in epitaxial graphene*. Ph.D. thesis, Georgia Institute of Technology (2010).

[91] The Standford Research System. *IGC100 - Ion Gauge Controller*, reverion 2.4 edition (2002).

[92] M. Sprinkle. *Epitaxial graphene on silicon carbide: low-vacuum growth, characterization, and device fabrication*. Dissertation, Georgia Institute of Technology (2010).

[93] L. Biasetto, M. Manzolaro, and A. Andrighetto. "Emissivity measurements of opaque gray bodies up to 2000° C by a dual-frequency pyrometer." *The European Physical Journal A* **38** (2), 167–171 (2008).

[94] C. Davisson and L. H. Germer. "Diffraction of electrons by a crystal of nickel." *Physical Review* **30** (6), 705–740 (1927).

[95] B. E. Murphy. *The physico-chemical properties of fullerenes and porphyrin derivatives deposited on conducting surfaces*. Ph.D. thesis, Trinity College Dublin (2014).

[96] M.-G. Barthes-Labrousse. "The Auger effect." *Microscopy Microanalysis Microstructures* **6** (3), 253–262 (1995).

[97] "Auger Effect." http://hyperphysics.phy-astr.gsu.edu/hbase/Atomic/auger.html.

[98] D. H. NARUMAND and K. D. CHILDS. "Auger spectrometers: A tutorial review." *Applied Spectroscopy Reviews* **34** (3), 139–158 (2004).

[99] "Scanning tunneling microscopy of nanomaterials." http://archive.cnx.org/contents/9891be71-2d10-46ca-ac19-c38385c54c8d@2/scanning-tunneling-microscopy-of-nanomaterials#id1165533962032.

[100] G. Binnig, H. Rohrer, C. Gerber, and E. Weibel. "Surface studies by scanning tunneling microscopy." *Physical Review Letters* **49** (1), 57–61 (1982).

[101] J. Bardeen. "Tunnelling from a many-particle point of view." *Physical Review Letters* **6** (2), 57–59 (1961).

[102] J. Tersoff and D. R. Hamann. "Theory of the scanning tunneling microscope." *Physical Review B* **31** (2), 805–813 (1985).

[103] Y. Li. *Nanostructured graphene on Si-terminated SiC and its electronic properties*. Ph.D. thesis, Georgia Institute of Technology (2016).

[104] Y. Martin, C. C. Williams, and H. K. Wickramasinghe. "Atomic force microscope-force mapping and profiling on a sub 100å scale." *Journal of Applied Physics* **61** (10), 4723 (1987).

[105] "Basic contact AFM & dynamic force microscope (DFM)." http://www.parkafm.com/index.php/park-spm-modes/91-standard-imaging-mode/223-basic-contact-afm-dynamic-force-microscope-dfm.

[106] J. M. Palmer. *Pre-growth structures for high quality epitaxial graphene nanoelectronics grown on silicon carbide*. Ph.D. thesis, Georgia Institute of Technology (2014).

[107] V. Kochat, A. Nath Pal, E. S. Sneha, A. Sampathkumar, A. Gairola, S. A. Shivashankar, S. Raghavan, and A. Ghosh. "High contrast imaging and thickness determination of graphene with in-column secondary electron microscopy." *Journal of Applied Physics* **110** (1), 014 315 (2011).

[108] M.-H. Park, T.-H. Kim, and C.-W. Yang. "Thickness contrast of few-layered graphene in SEM." *Surface and Interface Analysis* **44** (11-12), 1538–1541 (2012).

[109] G. P. W.J. Choyke, H. Matsunami. *Silicon Carbide: Recent Major Advances* (Springer, 2004).

[110] K. Heinz, J. Bernhardt, J. Schardt, and U. Starke. "Functional surface reconstructions of hexagonal SiC." *Journal of Physics: Condensed Matter* **16** (17), S1705–S1720 (2004).

[111] U. Starke, J. Schardt, and M. Franke. "Morphology, bond saturation and reconstruction of hexagonal SiC surfaces." *Applied Physics A: Materials Science & Processing* **65** (6), 587–596 (1997).

[112] U. Starke. "Atomic structure of hexagonal SiC surfaces." *physica status solidi (b)* **202** (1), 475–499 (1997).

[113] U. Starke, J. Schardt, J. Bernhardt, M. Franke, and K. Heinz. "Stacking transformation from hexagonal to cubic SiC induced by surface reconstruction: A seed for heterostructure growth." *Physical Review Letters* **82** (10), 2107–2110 (1999).

[114] C. Riedl, U. Starke, J. Bernhardt, M. Franke, and K. Heinz. "Structural properties of the graphene-$SiC(0001)$ interface as a key for the preparation of homogeneous large-terrace graphene surfaces." *Physical Review B* **76** (24) (2007).

[115] X. Xie, H. Wang, A. Wee, and K. P. Loh. "The evolution of $r30°$ and $6\sqrt{3}\times 6\sqrt{3})r30°$ superstructures on $6H-SiC(0001)$ surfaces studied by reflection high energy electron diffraction." *Surface Science* **478** (1-2), 57–71 (2001).

[116] M. Naitoh, J. Takami, S. Nishigaki, and N. Toyama. "A $(2\sqrt{3}\times 2\sqrt{13})$ surface phase in the $6H-SiC(0001)$ surface studied by scanning tunneling microscopy." *Applied Physics Letters* **75** (5), 650 (1999).

[117] L. Li, Y. Hasegawa, T. Sakurai, and I. S. T. Tsong. "Field-ion scanning tunneling microscopy study of the atomic structure of $6H-SiC(0001)$ surfaces cleaned by in situ si molecular beam etching." *Journal of Applied Physics* **80** (4), 2524 (1996).

[118] J. Bernhardt, M. Nerding, U. Starke, and K. Heinz. "Stable surface reconstructions on $6H-SiC(000\bar{1})$." *Materials Science and Engineering: B* **61-62**, 207–211 (1999).

[119] G. He, N. Srivastava, and R. M. Feenstra. "Formation of a buffer layer for graphene on C-face $SiC(000\bar{1})$." *Journal of Electronic Materials* **43** (4), 819–827 (2013).

[120] S. Shivaraman, M. V. S. Chandrashekhar, J. J. Boeckl, and M. G. Spencer. "Thickness estimation of epitaxial graphene on SiC using attenuation of substrate raman intensity." *Journal of Electronic Materials* **38** (6), 725–730 (2009).

[121] H. Hiura, H. Miyazaki, and K. Tsukagoshi. "Determination of the number of graphene layers: Discrete distribution of the secondary electron intensity stemming from individual graphene layers." *Applied Physics Express* **3** (9), 095 101 (2010).

[122] Y. K. Koh, M.-H. Bae, D. G. Cahill, and E. Pop. "Reliably counting atomic planes of few-layer graphene ($n > 4$)." *ACS Nano* **5** (1), 269–274 (2011).

[123] I. G. Ivanov, J. U. Hassan, T. Iakimov, A. A. Zakharov, R. Yakimova, and E. Janzen. "Layer-number determination in graphene on SiC by reflectance mapping." *Carbon* **77**, 492–500 (2014).

[124] L. Frank, E. Mikmekova, I. Mullerova, and M. Lejeune. "Counting graphene layers with very slow electrons." *Applied Physics Letters* **106** (1), 013 117 (2015).

[125] A. Nakayama, S. Hoshino, Y. Yamada, A. Ohmura, and F. Ishikawa. "Counting graphene layers based on the light-shielding effect of raman scattering from a substrate." *Applied Physics Letters* **107** (23), 231 604 (2015).

[126] J. Biberian and G. Somorjai. "On the determination of monolayer coverage by Auger electron spectroscopy. application to carbon on platinum." *Applications of Surface Science* **2** (3), 352–358 (1979).

[127] M. Xu, D. Fujita, J. Gao, and N. Hanagata. "Auger electron spectroscopy: A rational method for determining thickness of graphene films." *ACS Nano* **4** (5), 2937–2945 (2010).

[128] L. Kotis, S. Gurban, B. Pecz, M. Menyhard, and R. Yakimova. "Determination of the thickness distribution of a graphene layer grown on a 2" SiC wafer by means of auger electron spectroscopy depth profiling." *Applied Surface Science* **316**, 301–307 (2014).

[129] G. Ertl and J. Kuppers. *Low Energy Electrons and Surface Chemistry* (VCH, 1985).

[130] J. Liday, S. Hofmann, and R. Harman. "Estimation of the electron backscattering factor in AES." *Czechoslovak Journal of Physics* **39** (7), 782–789 (1989).

[131] C. J. Powell and A. Jablonski. "NIST electron effective-attenuation-length database - version 1.3." *National Institute of Standards and Technology, Gaithersburg, MD* (2011).

[132] C. J. Powell and A. Jablonski. "NIST backscattering-correction-factor database for auger electron spectroscopy, version 1.1 of SRD 154." *National Institute of Standards and Technology, Gaithersburg, MD* (2015).

[133] C. J. Powell, A. Jablonski, F. Salvat, and A. Y. Lee. "NIST electron elastic-scattering cross-section database, version 4.0." *National Institute of Standards and Technology, Gaithersburg, MD* (2016).

[134] L. E. Davis. *Handbook of Auger electron spectroscopy : A reference book of standard data for identification and interpretation of Auger electron spectroscopy data* (Physical Electronics Industries, 2d edition, 1972).

[135] R. Payling. "Modified elemental sensitivity factors for auger electron spectroscopy." *Journal of Electron Spectroscopy and Related Phenomena* **36** (1), 99–104 (1985).

[136] P. W. Palmberg. "Quantitative Auger electron spectroscopy using elemental sensitivity factors." *Journal of Vacuum Science and Technology* **13** (1), 214 (1976).

[137] P. Hall and J. Morabito. "Matrix effects in quantitative auger analysis of dilute alloys." *Surface Science* **83** (2), 391–405 (1979).

[138] G. Leveque and J. Bonnet. "Quantitative correction of backscattering in Auger electron spectroscopy of thin films." *Applied Surface Science* **89** (2), 211–219 (1995).

[139] S. Tanuma, C. J. Powell, and D. R. Penn. "Calculations of electron inelastic mean free paths. ix. data for 41 elemental solids over the 50 eV to 30 keV range." *Surface and Interface Analysis* **43** (3), 689–713 (2011).

[140] S. Goler, C. Coletti, V. Piazza, P. Pingue, F. Colangelo, V. Pellegrini, K. V. Emtsev, S. Forti, U. Starke, F. Beltram, and et al.. "Revealing the atomic structure of the buffer layer between $SiC(0001)$ and epitaxial graphene." *Carbon* **51**, 249–254 (2013).

[141] M. Seah. "Quantitative auger electron spectroscopy and electron ranges." *Surface Science* **32** (3), 703–728 (1972).

[142] D. G. Watson, P. E. Larson, D. F. Paul, and R. E. Negri. "High energy resolution auger spectroscopy on a CMA instrument." *Surface and Interface Analysis* **44** (1), 121–125 (2011).

[143] U. Starke, J. Schardt, J. Bernhardt, and K. Heinz. "Reconstructed oxide structures stable in air: Silicate monolayers on hexagonal SiC surfaces." *Journal of Vacuum Science & Technology A: Vacuum, Surfaces, and Films* **17** (4), 1688 (1999).

[144] N. Sieber, B. F. Mantel, T. Seyller, J. Ristein, L. Ley, T. Heller, D. R. Batchelor, and D. Schmei?er. "Electronic and chemical passivation of hexagonal $6H - SiC$ surfaces by hydrogen termination." *Applied Physics Letters* **78** (9), 1216?1218 (2001).

[145] N. Sharma, D. Oh, H. Abernathy, M. Liu, P. N. First, and T. M. Orlando. "Signatures of epitaxial graphene grown on Si-terminated 6H-SiC (0001)." *Surface Science* **604** (2), 84?88 (2010).

[146] A. Hubbard. *The Handbook of Surface Imaging and Visualization* (CRC Press, 1995).

[147] F. Ming and A. Zangwill. "Phase field modeling of submonolayer epitaxial growth." *Physical Review B* **81** (23) (2010).

[148] F. Ming and A. Zangwill. "Model for the epitaxial growth of graphene on $6H - SiC(0001)$." *Physical Review B* **84** (11) (2011).

[149] F. Ming. *Theoretical studies of the epitaxial growth of graphene.* Ph.D. thesis, Georgia Institute of Technology (2011).

[150] F. Ming and A. Zangwill. "Model and simulations of the epitaxial growth of graphene on non-planar $6H - SiC$ surfaces." *Journal of Physics D: Applied Physics* **45** (15), 154 007 (2012).

[151] J. Xie and J. P. Spallas. "Different contrast mechanisms in SEM imaging of graphene." *Agilent Technologies* (2012).

[152] A. Nakajima, H. Yokoya, Y. Furukawa, and H. Yonezu. "Step control of vicinal $6H - SiC(0001)$ surface by h_2 etching." *Journal of Applied Physics* **97** (10), 104 919 (2005).

[153] W. Hong, H. N. Lee, M. Yoon, H. M. Christen, D. H. Lowndes, Z. Suo, and Z. Zhang. "Persistent step-flow growth of strained films on vicinal substrates." *Physical Review Letters* **95** (9) (2005).

[154] E. S. Fu, D.-J. Liu, M. Johnson, J. Weeks, and E. D. Williams. "The effective charge in surface electromigration." *Surface Science* **385** (2-3), 259–269 (1997).

[155] S. Stoyanov. "New type of step bunching instability at vicinal surfaces in crystal evaporation affected by electromigration." *Surface Science* **416** (1-2), 200–213 (1998).

[156] G. Ehrlich. "Atomic view of surface self-diffusion: Tungsten on tungsten." *J. Chem. Phys.* **44** (3), 1039 (1966).

[157] R. L. Schwoebel. "Step motion on crystal surfaces." *Journal of Applied Physics* **37** (10), 3682 (1966).

[158] M. Xie, S. Leung, and S. Tong. "What causes step bunching: negative Ehrlich-Schwoebel barrier versus positive incorporation barrier." *Surface Science* **515** (1), L459–L463 (2002).

[159] C. Misbah, O. Pierre-Louis, and Y. Saito. "Crystal surfaces in and out of equilibrium: A modern view." *Rev. Mod. Phys.* **82** (1), 981–1040 (2010).

[160] J. Krug, V. Tonchev, S. Stoyanov, and A. Pimpinelli. "Scaling properties of step bunches induced by sublimation and related mechanisms." *Physical Review B* **71** (4) (2005).

[161] E. Williams. "Steps on surfaces: Experiment and theory." *Surface Science Reports* **34** (6-8), 175–294 (1999).

[162] D.-J. Liu and J. D. Weeks. "Quantitative theory of current-induced step bunching on Si(111)." *Physical Review B* **57** (23), 14 891–14 900 (1998).

[163] E. Gruber and W. Mullins. "On the theory of anisotropy of crystalline surface tension." *Journal of Physics and Chemistry of Solids* **28** (5), 875?887 (1967).

[164] G. S. Bales and A. Zangwill. "Morphological instability of a terrace edge during step-flow growth." *Physical Review B* **41** (9), 5500?5508 (1990).

[165] Y. Li, X. Chen, and J. Su. "Study on formation of step bunching on $6H - SiC(0001)$ surface by kinetic Monte Carlo method." *Applied Surface Science* **371**, 242–247 (2016).

[166] H. J. Guo, W. Huang, J. Peng, R. W. Zhou, X. C. Liu, Y. Q. Zheng, and E. W. Shi. "Study of ehrlich-schwoebel barrier in 4H-SiC epitaxial growths by molecular statics method." *Materials Science Forum* **858**, 217–220 (2016).

[167] Y.-N. Yang, E. S. Fu, and E. D. Williams. "An STM study of current-induced step bunching on $si(111)$." *Surface Science* **356** (1-3), 101–111 (1996).

[168] K. Mochizuki. "Theoretical consideration of step-flow and two-dimensional nucleation modes in homoepitaxial growth of $4H - SiC(0001)$ vicinal surfaces under silicon-rich condition." *Applied Physics Letters* **93** (22), 222 108 (2008).

[169] V. Borovikov and A. Zangwill. "Step bunching of vicinal $6H - SiC0001$ surfaces." *Physical Review B* **79** (24) (2009).

[170] V. Borovikov and A. Zangwill. "Step-edge instability during epitaxial growth of graphene from $SiC(0001)$." *Physical Review B* **80** (12) (2009).

[171] T. Ohta, N. C. Bartelt, S. Nie, K. Th?rmer, and G. L. Kellogg. "Role of carbon surface diffusion on the growth of epitaxial graphene on SiC." *Physical Review B* **81** (12) (2010).

[172] H. Hertz. "Ueber die verdunstung der fl?ssigkeiten, insbesondere des quecksilbers, im luftleeren raume." *Annalen der Physik* **253** (10), 177?193 (1882).

[173] R. M. Tromp and J. B. Hannon. "Thermodynamics and kinetics of graphene growth on $SiC(0001)$." *Physical Review Letters* **102** (10) (2009).

[174] W. Zhang, X. Yu, E. Cahyadi, Y.-H. Xie, and C. Ratsch. "On the kinetic barriers of graphene homo-epitaxy." *Applied Physics Letters* **105** (22), 221 607 (2014).

[175] P. Vogt, P. De Padova, C. Quaresima, J. Avila, E. Frantzeskakis, M. C. Asensio, A. Resta, B. Ealet, and G. Le Lay. "Silicene: Compelling experimental evidence for graphenelike two-dimensional silicon." *Physical Review Letters* **108** (15) (2012).

[176] E. Cinquanta, E. Scalise, D. Chiappe, C. Grazianetti, B. van den Broek, M. Houssa, M. Fanciulli, and A. Molle. "Getting through the nature of silicene: An $sp^2 - sp^3$ Two-dimensional silicon nanosheet." *The Journal of Physical Chemistry C* **117** (32), 16 719–16 724 (2013).

[177] Y. Cai, C.-P. Chuu, C. M. Wei, and M. Y. Chou. "Stability and electronic properties of two-dimensional silicene and germanene on graphene." *Physical Review B* **88** (24) (2013).

[178] Y. Yamada-Takamura and R. Friedlein. "Progress in the materials science of silicene." *Science and Technology of Advanced Materials* **15** (6), 064 404 (2014).

[179] M. Houssa, A. Dimoulas, and A. Molle. "Silicene: A review of recent experimental and theoretical investigations." *J. Phys.: Condens. Matter* **27** (25), 253 002 (2015).

[180] C. Grazianetti, E. Cinquanta, and A. Molle. "Two-dimensional silicon: the advent of silicene." *2D Materials* **3** (1), 012 001 (2016).

[181] C. J. Powell and A. Jablonski. "NIST electron inelastic-mean-free-path database - version 1.2." *National Institute of Standards and Technology, Gaithersburg, MD* (2010).

VITA

Tien Hoang was born in Hung Yen, Vietnam in 1986. As a child, he was interested in natural science and the world that surrounded him. Tiens childhood dream was to acquire a National Olympiad medal for K-12 students. Thanks to his commitment and passion for physics, Tien won two silver medals in the National Physics Olympiad for 12th-grade students in 2003 and 2004. After that, Tien was selected to the Honors Program at the Vietnam National University. In Fall 2009, Tien got admitted to the Ph.D. program at the Georgie Institute of Technology. One year later, he joined Dr. Firsts group to study surfaces, interfaces, and nanostructures of materials. Tien chose graphene as a subject of study because of its potential applications in nanoelectronics devices. After receiving a Ph.D. diploma, Tien plans to use his research accomplishments as a quantitative analyst and, in the future, to become a data scientist.